THE INFLUENCE OF SCALE, GEOMETRY, AND MICROSTRUCTURE ON THE

ELECTRICAL PROPERTIES OF CHEMICALLY DEPOSITED

THIN SILVER FILMS

by

SARAH M. PETERSON

A DISSERTATION

Presented to the Department of Chemistry
and the Graduate School of the University of Oregon
in partial fulfillment of the requirements
for the degree of
Doctor of Philosophy

December 2007

"The Influence of Scale, Geometry, and Microstructure on the Electrical Properties of Chemically Deposited Thin Silver Films," a dissertation prepared by Sarah M. Peterson in partial fulfillment of the requirements for the Doctor of Philosophy degree in the Department of Chemistry. This dissertation has been approved and accepted by:

_____   _____

Marina Guenza, Chair of the Examining Committee

_11/20/2007_____

Date

Committee in Charge: Marina Guenza, Chair
                               Mark Lonergan
                               Jim Hutchison
                               Rahgu Parthasarathy

Accepted by:

_____

Dean of the Graduate School

An Abstract of the Dissertation of

Sarah M. Peterson   for the degree of   Doctor of Philosophy

in the Department of Chemistry   to be taken   December 2007

Title: THE INFLUENCE OF SCALE, GEOMETRY, AND MICROSTRUCTURE ON

THE ELECTRICAL PROPERTIES OF CHEMICALLY DEPOSITED THIN

SILVER FILMS

Approved: _____

Miriam Deutsch, Ph.D.

Silver films with nanoscale to mesoscale thicknesses were produced by chemical

reduction onto silica substrates and their physical and electrical properties were

investigated and characterized. The method of silver deposition was developed in the

context of this research and uses a single step reaction to produce consistent silver films

on both flat silica coverslips and silica nanospheres of 250-1000 nm. Both the structure

and the electrical properties of the silver films are found to differ significantly from those

produced by vacuum deposition. Chemically deposited (CD) silver is not uniformly

smooth, but rather is granular and porous with a network-like structure. By quantitatively

accounting for the differences in scale, geometry, and microstructure of the CD films, it

is found that the same models used to describe the resistivity of vacuum deposited films

may be applied to CD films. A critical point in the analysis that allows this relation involves the definition of a geometric parameter, g, which replaces the thickness, t, as the critical length that influences the electrical properties of the film. The temperature dependent properties of electrical transport were also investigated and related to the microstructure of the CD films. A detailed characterization of CD silver as shells on silica spheres is also presented including physical and optical properties. In spite of the rough and porous morphology of the shells, the plasmon resonance of the core-shell structure is determined by the overall spherical shell structure and is tunable through variations in the shell thickness. Preliminary investigations into the electrical transport properties of aggregates of silver coated spheres suggest similarities in the influence scale, geometry, and microstructure to silver films on flat substrates. The aggregates of shells also exhibit pressure related resistance behavior due to the composite structure.

CURRICULUM VITAE

NAME OF AUTHOR: Sarah M. Peterson

PLACE OF BIRTH: Beeville, TX

DATE OF BIRTH: November 10, 1975

GRADUATE AND UNDERGRADUATE SCHOOLS ATTENDED:

     University of Oregon
     University of Dallas

DEGREES AWARDED:

     Doctor of Philosophy, Inorganic Chemistry, December 2007,
          University of Oregon
     Master of Science, Chemistry, December 2003, University of Oregon
     Bachelor of Science, Chemistry, December 1997, University of Dallas

PROFESSIONAL EXPERIENCE:

     Teaching Assistant, University of Oregon, 2002-2003, 2006-2007
          Taught and graded general chemistry laboratory with up to 40 students
          per term

     Petroleum Analyst, Netherland Sewell & Associated, 1999-2002
          Collaborated with engineers and analysts in a team environment to provide
          clients with consulting services and estimates of petroleum reserves and
          future revenue, including publication of official SEC reports

     Chemist/Technician, Xenco Laboratories, 1997-1998
          Provided contract analysis of soil and water samples in a small private
          laboratory using EPA instrumentation methods including BTEX, MTBE,
          and TPH method W4181

GRANTS, AWARDS AND HONORS:

Magna cum Laude, University of Dallas, 1997

Phi Beta Kappa, 1997

NSF GK-12 Fellowship, University of Oregon, 2003-2006

PUBLICATIONS:

Peterson, M.S.M.; Deutsch, M.; Bouwman, J.; Chen, A. *J. Colloid Interface Sci.* **2007**, *306*, 41-49.

ACKNOWLEDGMENTS

This dissertation is dedicated to Mike Peterson and to our future children. I present this work to them in the hope that all scientific research will strive not to conquer, but rather to serve the human soul and intellect as it pursues a deeper understanding of the depths of God's gift of creation.

TABLE OF CONTENTS

LIST OF FIGURES

LIST OF TABLES

CHAPTER I

INTRODUCTION

Background

The field of nanotechnology is a broad one, ripe with discoveries fueling applications that range from flexible electronic materials[1-3] to biomedical detection and control of neural signals in vivo.[4] The true promise of the nanoscale lies not only in the small size of the material, but in physical and chemical properties which cannot be found in the same materials at larger dimensions. Hence, the focus of research in the realm of the very small is not governed purely by whether a material is nano- or meso- or microscale, but by the altered properties that it displays which cannot be found in other size regimes. For example, the electrical resistance of metals increases dramatically for size regimes much smaller than their electron mean free path $(\lambda.)$[5] Nanoparticles of metals also have optical resonances which strongly depend on particle size, composition, and chemical environment.[6,7]

A primary motivation for studying thin vacuum deposited (VD) metallic films has been to find useful conducting materials in the ever shrinking world of electronics.[8,9] Therefore resistivity and the impact of temperature on resistivity are key properties of interest in thin metal films. A large body of theoretical work and experimental data now exists studying the impact of the scale of film thickness on the electrical properties of VD films.[5,9-14] Some of this work is outlined in greater detail in Chapter 2. Interestingly, little effort has been made to compare the electrical properties of films produced by other methods, such as chemical reduction methods, to VD films.[15] The foundation of our understanding of thin metal films is therefore based on VD films often grown with smooth surfaces and epitaxial microstructures[16] that are very different from the morphologies found in chemically deposited films.

This dissertation explores the electrical transport properties of chemically deposited (CD) thin silver films and compares them to those of VD films. These properties are altered due to nanometer length scales, deposition geometry, and microstructure.

When nanoscale silver crystallites form the building blocks of a microscale structure, their geometric arrangement on the substrate, as well as the electrical contact between the crystallite grains, have a significant impact on the electrical transport properties of the overall material. These microscale composites are deposited on substrates through a chemical reduction process. Because of the resulting scale, geometry, and microstructure of the crystallites, the well studied metal, silver, becomes a material which no longer behaves electronically like the bulk metal. It also differs electronically from thin VD films of silver to which it would seem most comparable.

Understanding how scale, geometry, and microstructure alter the electronic behavior of a well understood bulk material is the first step toward the ability to design new devices with electrical properties engineered on a micro or even nanoscopic level. This microstructural control of properties is at the forefront of materials research today. Electronics applications, catalysis, sensing, and even solar energy capture can use the electronic and optical characteristics of metallic and semiconducting materials altered by the material dimensions in a constructive way.[3,17-19]

Within the field of nanoscale metals, the study of noble metal shells patterned onto nanoscale dielectric spheres, known as metal nanoshells, is another important segment of these studies. Based on their optical properties, noble metal nanoshells offer numerous useful applications in a variety of fields, including biomedical studies, photonic band gap materials, and chemical catalysis.[20-23] The intriguing geometry of core-shell materials has primarily been studied for its optical characteristics.[24,25] The rapid growth in the field of plasmonics has resulted in increased investigation of the optical properties of metal films on flat substrates as well.[26-28] Studies to date have not, however, compared the electrical properties of flat films to those of shells. The disparate motives and objectives of research on thin films and metal nanoshells have not required such a comparison.

This body of research focuses on the investigation of the electrical transport properties of CD silver films on flat substrates, but also seeks to compare them to silver deposited by the same method on spherical substrates. The data suggest that the electrical properties of disordered metal films, whether flat or spherical are governed by similar factors of scale, geometry and microstructure. However, the comparison is limited. For example, we have not measured the resistance across a single sphere, and modeling of sphere resistance data is not possible with the current body of data. Resistance across aggregates of spheres are used to elucidate the basic comparison of shells to films. Further study in this area is necessary and could lead to a unified

model of conductivity in nanocrystalline silver materials. Such a system would be extremely useful for the microstructural design of desired electronic properties.

Core-Shell Materials

Unlike metal thin films which can be produced by a variety of high vacuum, electrolysis, or chemical reduction methods, complete spherical metal nanoshells can only be produced through deposition in solution. Typically, a chemical reduction of metal salt precursor is used to produce a nanoscale metal shell. These methods rarely produce a shell that is as smooth or uniform as a vacuum deposited film.

The research presented for core-shell materials includes a new single step method for the electroless deposition of silver onto silica. Metal nanoshell materials are synthesized using solution-based electroless deposition methods in which a metal precursor is reduced onto colloidal dielectric spheres to produce a nanoscale shell.[24,29–35] These coatings may consist either of smooth and complete layers of metal, or rough aggregates of metal nanoparticles on the sphere surfaces. Both such morphologies effectively surround the core and are referred to as contiguous in this work.

Current methods for producing contiguous metal shells require multiple steps. Typically, the first step produces a layer of metal nanoparticle seeds of 2-20 nm average size. Either an organic ligand or direct reduction is used to attach the metal nanoparticles to the dielectric sphere. This process is known as decorating the sphere.[29,32,34–39] The seeds may be of the same metal as the final shell or a different one. Some methods use these seeds to induce further metal reduction onto the sphere surface by providing nucleation centers.[24,32,34,40] Others repeat the seeding process to obtain thicker coatings layer by layer.[31,37]

The impact of organic ligands and seeds of a different metal on the electronic transport and optical properties of core-shell materials has not been thoroughly studied yet. As with other nanometer scale metals, these properties are expected to be highly sensitive to their chemical environment. It is therefore advantageous to develop fabrication protocols which yield pure, two-component inorganic metallodielectric particles such as the method presented here.

Recently it was shown that the well known Tollen's reaction, commonly used for silvering mirrors may be employed to decorate sub-micron dielectric spheres with a seed layer of silver nanoparticles approximately 20 nm in size.[36] The method reported in this work has been independently developed to fabricate core-shell materials of

silver on silica and is based on the Tollen's process and it's general reduction reaction.[41] What distinguishes this method from previously published results is that the silver shell forms in a single step process without employing seeding or other chemical functionalization of the spheres. Silver shells have been previously produced using several established methods but all of them require multiple steps.[24,29-32]

A study of the optical properties of the silver shells produced here allows a comparison with core-shell structures produced by other methods. The alteration of the surface plasmon resonance (SPR) of nanoscale metals in response to their dimensions, geometry, and chemical environment is an example of optical properties being impacted by nanoscale sizing. Unlike bulk metals, the SPR of metal nanoparticles and nanoscale core-shell structures is a unique, sensitive function of the system's size, shape, and environment. In extinction spectroscopy this is usually observed through characteristic peaks and overall shape and width of the absorption spectrum.[6,42-46] Consequently, metal nanoparticles have been used in sensing applications,[7,47,48] and the tunability of core-shell structures has been studied for use in photonic bang gap materials.[21]

To date, the electrical properties of noble metal core-shell structures have not been studied either individually or in aggregates. The film morphologies of silver deposited on spheres by the electroless method to be reported in Chapter 6 are very similar to those grown on flat substrates to be presented in Chapter 3. Therefore it is reasonable to expect that studies of the properties of these coatings on flat silica substrates will offer a reliable comparison for studies of the core-shell materials. A detailed analysis of the electrical properties of the silver films is thus pursued and used for comparison to the core-shell materials deposited by the same process.

Thin Metal Films

Thin metal films, nanowires, and nanostructured metals are each structures that include one or more critical length scales on the order of bulk metal λ. Consequently, they exhibit electrical properties which are influenced by the length scales of the system. The limiting dimension for epitaxial thin silver films is the film thickness.[9,14] For thickness values on the order of λ, elevated resistivity is detected due to the contribution of electron scattering at the film surfaces. Wires have additional scattering around the entire circumference of the wire. Nanostructured metals (n-metals) are a class of materials composed of individually formed nanoparticles that are shaped into

much larger structures.[49] While they typically have macroscopic dimensions overall, they exhibit elevated resistivity due to the small sizes of the individual crystallites.[50,51] In every case conduction is reduced due to a limitation of electron transport caused by a mismatch or interface of the metal crystal lattice.

The CD silver films presented here will be shown to have various structural elements which can be related to thin films, nanowires, or n-metal materials. The study of CD films aids in understanding the relationship between the scale of the material and its electrical properties. The understanding gained through the CD silver films regarding the relationship between geometry, microstructure, and resistivity is relevant to all conducting materials. The elevated resistivity and high surface areas studied in these films may allow for greater sensitivity in sensing or catalysis applications using noble metals. Application of this understanding to systems using alternative metals or semiconductors will enable further optimization of desired electronic characteristics.

A background in the current understanding of the electrical behavior of thin films, wires, and nanostructured silver (n-Ag) materials provides the context for the study of CD films. The body of research on thin silver films produced by vacuum deposition is extensive. The majority of mathematical modeling of the influence of the nanoscale on resistivity has been based on VD films. Nanowires can often be included in the models for thin films with minimal modifications due to the additional nanoscale dimension. Methods for the production of nanowires are becoming more prevalent and are providing new data to verify existing models.[52,53] N-metals, though most often studied for a large range of physical properties,[49] are also gaining attention for their electrical transport properties.[50,51,54] Data for films, nanowires, and n-metals will be referenced whenever the relationship between their structures and electrical properties may assist in the understanding of CD films.

Chapter 2 will outline currently accepted mathematical modeling which describes the influence of scale and microstructure on VD films. These models will be used as the basis of the analysis of the electrical properties of CD films and their comparison to VD films throughout this work.

CHAPTER II

MODELING AND RESISTIVITY IN NANOSCALE METALS

A review of the development of modeling for thin metal films is presented with references to nanowires and n-Ag materials wherever appropriate. An understanding of the studies presented in the literature provides a crucial launch point for elucidating the transport properties of CD films.

The Drude Model

The resistivity, ρ, of metals is governed by their electron mean free path, λ, which is the distance that an electron travels under bias before a scattering event takes place. The length of λ in a perfect infinite crystal is only limited by the phonon vibrations of the atoms that make up the lattice. The infinite crystalline resistivity of a given metal is described by the Drude model, written as,

$$\rho = \frac{m_e v_f}{n e^2 \lambda} \tag{2.1}$$

or

$$\rho = \frac{m_e}{n e^2 \tau} \tag{2.2}$$

where m_e is the mass of an electron, v_f is the Fermi velocity, n is the electron density characteristic of the element, e is the charge of an electron and τ is the relaxation time.[55] The relaxation time is the average time an electron travels between scattering events and is directly related to λ such that $\tau = \frac{\lambda}{v_f}$.

On the scale of bulk metals, impurities and lattice defects can also decrease λ. The empirically derived Matthiessen rule accounts for these additional scattering events by the summation of all contributions to the resistivity.[9] Thus the resistivity due to lattice imperfections and impurities, ρ_i, is added to the resistivity due to phonons, ρ_p.

This gives an effective mean free path such that

$$\lambda_{eff} = \left(\frac{1}{\lambda_p} + \frac{1}{\lambda_i} \right)^{-1} \tag{2.3}$$

where λ_p is the mean free path due to phonon scattering alone and λ_i is the mean free path based on scattering due to all other imperfections, excluding phonon vibrations. When one or more dimensions of the metal is on the order of λ, scattering processes at the surface become significant to ρ. An appropriate description of the resistivity of these films thus requires a λ_s term to account for scattering at the surface of the film.

The Classical Size Effect

The Fuchs-Sondheimer (F-S) model is widely accepted for describing the influence of film thickness, t, on ρ. The F-S model imposes boundary conditions on the Boltzmann transport equation to describe the limitations of t on electrical transport.[5,10] A specularity parameter, p, is introduced to describe the fraction of electrons specularly reflected at the surface. A value of p equal to 1 indicates completely specular reflection such that ρ is independent of t. Completely diffuse scattering is indicated by $p = 0$. The value of p may vary significantly between these extremes depending on the nature of the reflecting surface. Diffusely scattered electrons contribute to a higher resistivity. For $t > \lambda$, the F-S model simplifies to the following:

$$\rho = \rho_o + \rho_o \frac{3\lambda_o}{8t} (1 - p) \tag{2.4}$$

such that

$$\lambda_{eff} = \left(\frac{1}{\lambda_o} + \frac{3}{8t} (1 - p) \right)^{-1} \tag{2.5}$$

and

$$\lambda_s = \frac{8t}{3 (1 - p)} \tag{2.6}$$

The F-S model maintains the Matthiessen rule such that the resistivity due to surface scattering is added to ρ_o. Thus, in the limit of very large values of t, the contribution of surface scattering approaches zero and $\rho = \rho_o$. For modeling wires, the relevant length is the wire diameter which replaces t in the equations and 3/4 replaces 3/8.

The value of p cannot be independently measured, it must be calculated using measured values of ρ. This calculation is trivial using a plot of ρt vs t,

$$\rho t = \rho_o t + \rho_o \frac{3\lambda_o}{8}\left(1 - p\right) \qquad (2.7)$$

which gives a line with slope ρ_o and y-intercept of $\rho_o \frac{3\lambda}{8}\left(1 - p\right)$. An example of this fitting is shown in Figure 2.1. For regions of the plot which are not linear, the model cannot be applied. This straightforward model is still used to accurately fit ρ data for many thin metal films and will be used in Chapter 4 for the fitting of VD films.
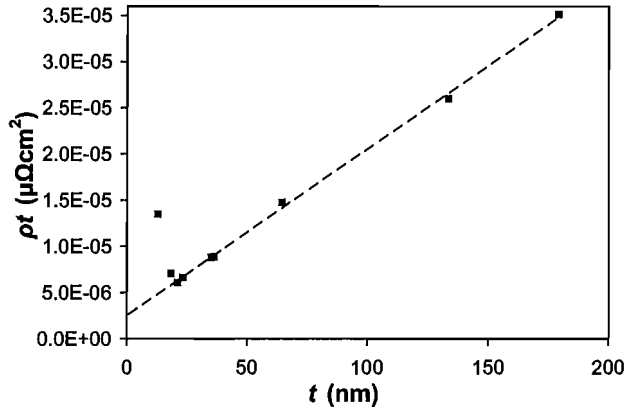
Figure 2.1: A plot of ρt vs t for VD films show the linear region in which the F-S analysis is applicable.

Epitaxial films are grown with single-crystalline structures, have minimal contamination when produced through vacuum deposition, and have near-atomically smooth surfaces. These films provide the ideal case for the study of the relationship between t and ρ as it deviates from the bulk metal description in the Drude model. It is not surprising that the ρ of these films can be fit well to F-S models.[14,56] VD polycrystalline films also fit these models reasonably well and are also very well studied.[9,14,57]

For films with $t < \lambda$ the F-S model gives,

$$\rho = \rho_o \frac{4\lambda}{3t} \frac{\left(1 - p\right)}{\left(1 + p\right)} \frac{1}{\log\left(\frac{\lambda}{t}\right)} \qquad (2.8)$$

and

$$\lambda_{eff} = \frac{3t}{4} \log \frac{\lambda}{t} \frac{\left(1 + p\right)}{\left(1 - p\right)} \qquad (2.9)$$

However, the F-S model is generally not accurate for VD films thinner than λ. The reasons for this are related to the deposition process. The growth of VD films begins with the nucleation of small islands which do not support ohmic conduction.[58,59] These islands persist at greater thicknesses for films deposited on glass than for those

on pure silicon due to substrate dependent growth modes[60] that are influenced by the lower adhesion of silver to glass.[26,59] As the islands grow, they coalesce and at some point a critical thickness, t_c, is reached, at which a conducting pathway exists across the films. For VD silver films, $t_c \approx 15$ nm. Continued growth up to $t \approx 50$ nm has been called the coalescence stage wherein the grains are not isolated islands, but are not yet complete films.[61] The limited connectedness of the film distinguishes it from the smooth complete films assumed by the F-S model, rendering the model inapplicable.

Polycrystalline films beyond the coalescence stage also tend to exhibit a rough surface, which introduces macroscale and microscale variations in film thickness.[14,62–66] Proposed models to include the influence of surface roughness on resistivity have ranged from the use of a sine function to approximate thickness variations[62] to the incorporation of measured roughness values using STM data.[63] These modifications are added to the F-S model adding or modifying the terms in λ_{eff} .

Grain Boundaries and Electron Density

It has also been noted that, unless epitaxial deposition is used, the films are generally polycrystalline and the size of their crystallite grains scales, on average, with t.[67,68] Since grain sizes on the order of λ induce an additional size effect of electron scattering at the grain boundaries, they also elevate the resistivity of the metal. These grain size effects are present for films thicker than the coalescence stage as well.

To account for the influence of grain boundary scattering, a term for λ_g has also been proposed,[67,68] yet attempts to model grain boundaries have experienced difficulties. Mayades and Schatzkes reviewed the use of the Boltzmann equation by F-S and proposed additional boundary conditions leading to a value of λ_g.[67] Others have also supported the concept of an overall scattering coefficient which also results in a single λ_{eff} for the film.[14] Multiple models with reasonable fits to data based on these concepts have been reported.[8,69,70] More recently it was determined that the process by which crystallite grain boundaries influence ρ could not be modeled properly using the Matthiessen rule.[71] Rather a grain boundary behaves as a potential barrier though which an electron can only pass with sufficient energy. Vancea and Hoffmann (V-H) conclude that this limitation of electrons results in a modification in n, the electron density, and not λ.[57,71,72] They present the following model where

the term $P^{\frac{\lambda}{D}}$ is derived from the quantum mechanical treatment.

$$\rho = \frac{m_e v_f}{e^2 \lambda n \left(P^{\frac{\lambda}{D}}\right)}$$ (2.10)

P is a transmission coefficient $(0 < P < 1)$ describing the fraction of electrons that pass through the grain boundary and D is the average grain size. The value of P may vary significantly based on the quality of the contact between grain in the film. Surface scattering, thickness variation and other modifications to λ may also be included in eq 2.10. This V-H model has gained wide acceptance in studies involving the influence of grain boundaries[50,51,69,73] and is qualitatively supported by the results presented here.

Nanostructured silver (n-Ag) materials, whose resistivity is dominated by grain boundaries, have been studied using the V-H model.[50,51] N-Ag materials have revealed that a lower packing density of the grains leads to greater resistivity. This can be interpreted as an effect of a lower quality contact between grains. In the V-H model this equates to a lower value of P.

Models based entirely on the quantum mechanics of conduction have also been used to explain resistivity data as a function of thickness $\rho(t)$ and in some cases have been shown to give close agreement with data and the semiclassical models.[8,74] We have implemented the semiclassical approach in our analysis of the resistivity of CD silver films.

Modeling Concerns

All of the models reviewed here consider ρ as a function of thickness. Wherever comparison to measured data is presented, resistivity is calculated from the measured values of resistance, R and t as $\rho = Rt$. For films of uniform thickness, t is the geometric parameter which best describes the influence of the metal geometry on the measured R. Many films to which the models have been previously applied, however, are not uniform. Some are reported to have surface roughness on the order of their thickness, implying the presence of voids and a semicontinuous structure.[12,62,64] In these cases we will show that for films that do not have a uniform thickness, the relationship $\rho = Rt$ does not apply.

An alternate geometric parameter, g, is proposed to be necessary in the accurate modeling of films with a network type geometry such that $\rho = Rg$. Otherwise, the

resistivity modeled is inaccurate and comparison to the bulk resistivity is not valid. A few studies on very thin VD (<10 nm) and agglomerated films noted the network film structures and used percolation type analyses.[75,76] Using a value of g determined for CD films, the use of percolation analysis is also supported for CD films.

The substitution of a new parameter of g for t does not alter the models discussed above. As in the case of wires, the use of the geometric length that is relevant to scattering within CD films will show that use of the appropriate value of g allows thin film models to relate more accurately to the films. These results are reported in Chapter 4.

CHAPTER III

CHEMICALLY DEPOSITED SILVER FILMS

Background

The effects of scale, geometry and microstructure on the electrical transport properties of silver are studied using chemically deposited (CD) silver on silica substrates. These polycrystalline CD films differ significantly from vacuum deposited (VD) films which have been studied extensively as presented in Chapter 2. CD films are polycrystalline and granular with a porous network of silver coverage present on the substrate as shown in Figure 3.1B,C, and D. A similar network-like form of silver on a flat substrate has also been observed for thermally agglomerated films[75] and in very thin polycrystalline vacuum deposited (VD) films in the coalescence stage.[61,77] VD films in the coalescence stage typically have thicknesses greater than t_c and less than the mean free path of silver, λ_{Ag}, which is ~55 nm at 273 K. Such films have been described as having surface roughness on the order of their thickness.[12,62,64] This roughness indicates that the films are porous and may have a significant concentration of voids.

Models describing uniform films have been modified in order to model the resistivity of films with significant surface roughness.[12,62,64] The parameter of void concentration however, is not generally reported. The void concentration is measured as the area fraction of substrate exposed and is referred to as the exposed substrate fraction, A_e. The measurement of A_e is a 2-D approximation of the porosity of a 3-D film. Measurable values of A_e are indicative of a network type structure within the film such that as A_e increases, it becomes inaccurate to discuss the films in terms of their average thickness alone. This applies to films in the general percolation range of $A_e \leq$ 30%.[78] The increased resistivity observed for CD films with A_e values as low as 5% can be explained in part by the increase in overall surface area of the film due to the exposed film walls bordering the voids. A basic calculation assuming cylindrical voids with a radius of 5 nm in a 10 nm thick film results in a 35% increase in metal surface area. The additional surface area increases with greater film thickness. Assuming
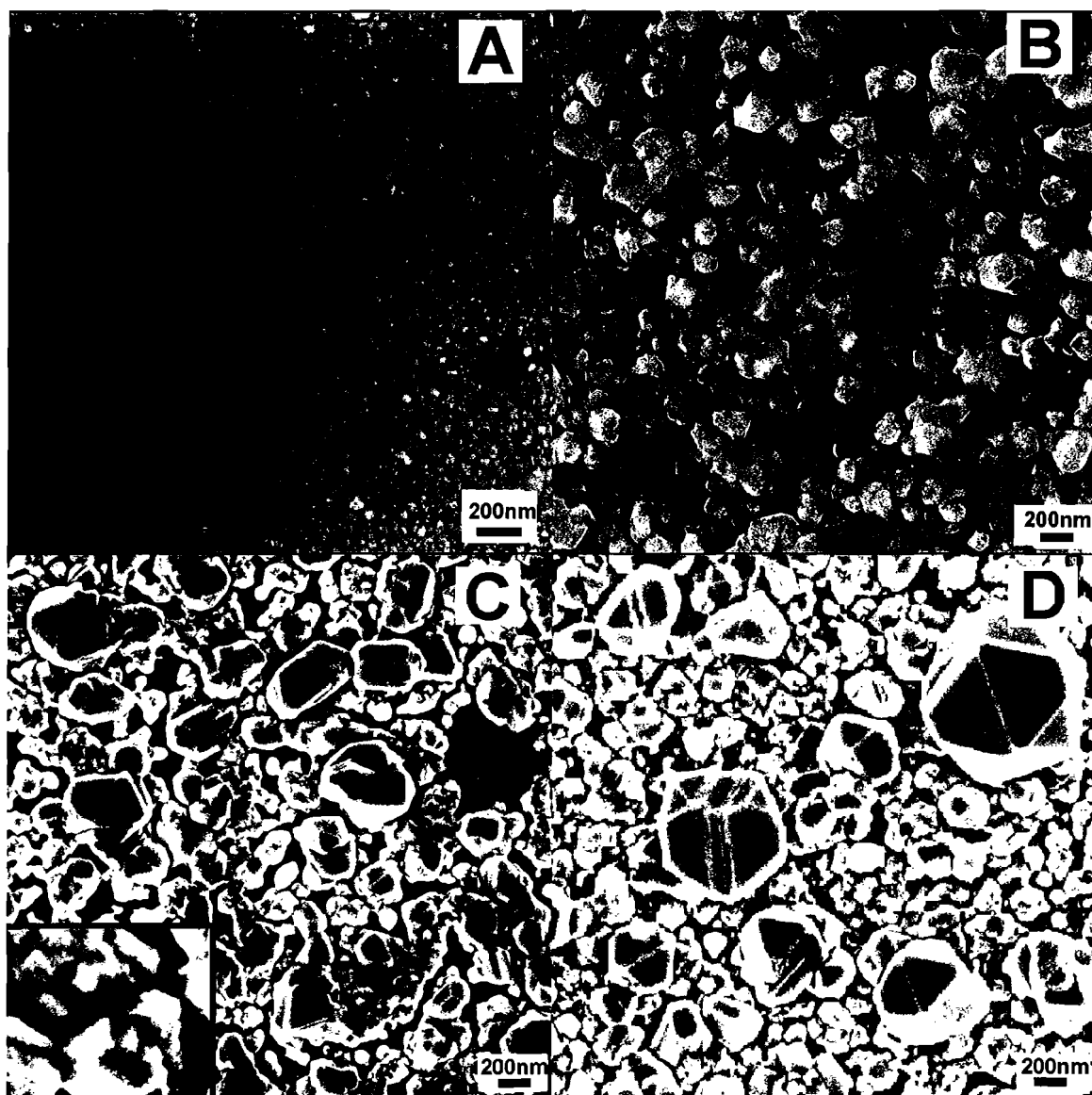
Figure 3.1: SEM micrographs of silver films. (A) 77 nm thick VD film which is equivalent to approximately 0.18 mg of silver. (B,C,D) Chemically deposited silver films with 0.14, 0.22, and 0.31 mg of silver deposited corresponding to t_{eff} values of 59, 93, and 131 nm respectively. The inset shows the irregularity of the interconnection between grains.

a uniform distribution, the voids would be as close together as 50 nm such that classical size effect surface scattering is significant at the void walls. It is therefore not surprising that significantly altered resistivity is observed for CD films which have measured A_e values of 5-10% even for very high average thicknesses ($t \gg \lambda_{Ag}$.) When discussing films with greater than 5% void space, even the term *film* can be misconstrued to imply a uniform smooth surface. For ease of discussion, all types of metal deposited on flat substrates are discussed herein as films.

A terminology is needed for the discussion of films which are too porous to be described only by their thickness. The term network morphology could be used, but morphology is used loosely in thin film literature to include both macroscale and microscale features,[56,79,80] while thin film crystallography uses the term morphology only to include microstructural properties such as crystallite size and orientation.[81] In order to avoid ambiguity we use the designation of *geometry* to differentiate the overall structure of the silver, excluding microstructural characteristics. Examples of different geometries include metal wires, foils, and shells. To describe the geometry of films with a high porosity, network, semicontinuous, or percolative geometry will be used. Semicontinuous and metal network are the more general terms as percolative implies that the films exhibit percolation behavior.[78] The percolation resistance behavior of CD films will be discussed further in Chapter 4. The term *microstructure* is used in the discussion of crystallite size, orientation, and the nature of contacts between crystallites.

This chapter presents the synthetic methods used in the preparation of CD and VD silver films followed by a comparison of some of their optical and electrical properties. VD silver films are extensively discussed in the literature and therefore ideal to assist in elucidating the unique aspects of CD films by comparison and contrast.

The electrical and optical characteristics of CD silver films are found to be influenced by the scale, network geometry, and microstructure of the silver. The presence of material length scales, such as t, comparable to λ_{Ag} is understood through classical size effects.[5,10] Scales on the order of λ_{Ag} are present in the thicknesses of VD films and in the average diameter of the interconnecting network branches of CD films, leading to increased resistivity through electron scattering at the metal surfaces.

Geometry becomes significant because the diameters of the network branches are on the scale of λ_{Ag}. If only the thickness of CD films were considered, the influence of surface scattering in thicker CD films would be falsely assumed negligible. The influence of network geometry on resistance is also important and has not been directly

addressed in resistivity models (as previously discussed in Chapter 2.) Properties which indicate the presence of network film geometry have been noted in the literature. Surface roughness on the order of the film thickness[57] indicates that the film is not only rough but has a significant A_e, suggesting a network geometry. Increased resistivity has also been attributed to the lengthened path of electrical transport reported in semicontinuous films without being explicitly accounted for in the modeling.[61] The potential need for an alternative geometric parameter, g, to replace t in relating the resistance and resistivity of these films has not been proposed. Lacking a definition of g, initial comparisons of CD to VD films must make use of calculated average thickness values in spite of the drawbacks. These comparisons clearly delineate the differences between CD and VD films and will aid in directing the determination of g in Chapter 4. One exciting result of knowing g for CD films is that the F-S model for scattering is found to be applicable even to these disordered films.

The microstructure also alters the resistivity of polycrystalline VD and CD films. Both types have crystallite grain sizes on the order of λ_{Ag}. According to the V-H model in eq 2.10, grain sizes of this scale modify film resistance by limiting the participation of conduction electrons in the conduction process.[71,72] The inset in Figure 3.1 also suggests that the quality of the electrical contact between grain that have grown together may also increase the resistivity. Both of these influences correspond well to data for CD films to be presented in in Chapter 5.

The powerful influence that geometry and microstructure hold over the electrical behavior of nanostructured metals is a critical tool for micro-engineering. The elevated resistivity of CD films is the result of the combination of scale, network geometry and microstructure. A thorough study requires that these characteristics be examined from multiple angles. With this end in mind, resistance studies are presented in the following three chapters. These include resistance studies, annealing and temperature dependence of resistance, presented in conjunction with multiple surface and structural analysis techniques including electron microscopy, atomic force microscopy, and X-ray diffraction. The conclusions drawn from these analyses provide a foundation upon which a model of the electrical properties of CD metal films may be developed.

Experimental Details

The synthesis of CD films is based on a modified Tollen's reaction. The procedures and reactions used in the deposition of CD and VD silver films are presented in detail as follows. The substrates used were 15x15 mm glass cover slips purchased from ProSciTech. Silver nitrate was obtained from Alfa Aesar. Concentrated ammonium hydroxide and glucose were obtained from Aldrich. All solutions were prepared using 18.2 MΩ·cm ultrapure water. The electroless deposition used to grow the silver films is derived from the method used to grow silver shells on silica nanospheres discussed in Chapter 6.[82] The substrates were cleaned overnight in Piranha solution, rinsed with ultrapure water and then soaked for 2 hours in NaOH solution with pH ~10. Soaking in base was found experimentally to improve the uniformity of the silver coating, presumably by hydroxylating the surface of the silica and slightly roughening the surface. Reactions were carried out by placing the rinsed substrate in approximately 15mL of 2 mM $AgNO_3$. Saturated glucose solution, ~30% w/w (10 μL) and 3% w/w NH_4OH (15 μL) were added to initiate the reaction. The reactions were carried out in centrifuge tubes which were shaken during the reaction using a VWR vortex mixer. The uniformity of the coating is sensitive to the mixing method. A vortex which lifts the slide in the mixture (rather than only spinning it) results in better film uniformity. Trials in which the substrates were not shaken resulted in thinner films and were often associated with the formation of silver nanoparticles in the reaction solution. The mass of silver deposited (and therefore the average thickness) was varied by decanting the reaction mixture after 7-25 minutes and resulted in films with masses of 0.1-0.5 mg. Silver films with a mass greater than 0.5 mg were produced by placing the slide into fresh silver nitrate solution and repeating the reaction. The coated slides were rinsed with ultrapure water and ethanol before being dried with filtered air and stored in sealed, clean, and dry centrifuge tubes. The mass of the slide before and after silver deposition was measured using a Sartrius Genius Series Semi-microbalance. Roughness and average thickness measurements were taken using atomic force microscopy (AFM.)

VD films were deposited under 10^{-6} Torr at ~1 Å per second. The thickness of VD films was determined by high-resolution wavelength dispersive spectroscopy using a Cameca SX-100, known as electron probe microanalysis (EPMA.) All resistance measurements were taken by the van der Pauw method[83] using a Keithley Source Measure Model 2400. SEM images were obtained using a Zeiss Ultra Mark II thermal

emission microscope (SEM.) Energy dispersive spectra (EDS) were obtained using an Oxford INCA EDS system in tandem with the Zeiss SEM. X-ray diffraction (XRD) spectra were collected using a Scintag XDS 2000. A Hewlett-Packard 8453 UV-visible (UV-vis) spectrophotometer was used to collect the optical extinction spectra.

Optical Studies

EDS and EPMA analyses revealed that residual reaction materials are not incorporated into the films and that a layer of 3-7 nm of silver (I) oxide is common to films which have been exposed to air. The details of these analyses are presented in Chapter 8. VD films with thicknesses of 12-80 nm were compared to CD films and optical differences were visible with the naked eye. VD films were silver in color and highly reflective for all thicknesses produced and films less than ~50 nm appeared blue in transmission of fluorescent room lighting. By contrast, CD films were highly scattering and appeared light gray. In direct reflection they cast different colors depending on the amount of silver deposited. Thinner films appeared golden in reflection while thicker films became pink and then violet. In transmission, CD films were semi-transparent with colors that ranged from light yellow-brown to brown and became dark gray for very thick films with a mass > 0.5 mg. This transparency is demonstrated in Figure 3.2. Two photographs are shown including both a target image directly illuminated by sunlight with a metal film sample used as a filter in front of the object, (A, C) and the corresponding background image photographs (B, D.)

The difference in the nature of the scattering and absorbance of the films is quantitatively expressed in their extinction spectra shown in Figure 3.2 E. Typical extinction spectra of several films, obtained by UV-vis are clearly separated into two groups, -low mass, high resistance films (0.173-0.239 mg, $R \approx$ 5-50 Ω) and high mass, low resistance ones (0.563-0.779 mg, $R \approx 0.3$ Ω) For clarity we only present the spectra of these two extreme mass groups. A double extinction peak is observed for all low mass films, indicating the excitation of multipolar resonances of the silver clusters.[44] These features broaden and merge into a single peak as the mass of the film increases, due to the strong electromagnetic coupling now present among the metal clusters.
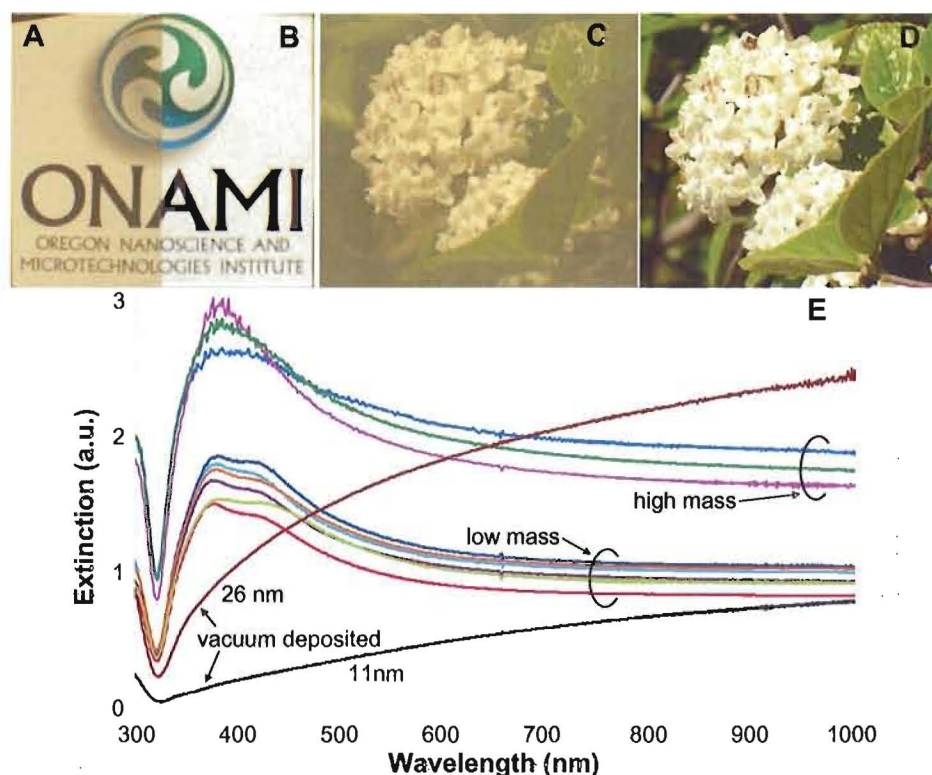
Figure 3.2: (A-D) The transparency of a CD film with t_{eff} of 111 nm is demonstrated using the film as a filter. (A,C) use a CD film as a filter while (B,D) are taken under the same sunlit conditions without a filter. (E) Extinction spectra are compared for VD films and CD films with high and low masses of silver deposited.

Electrical Studies

A collection of previously reported resistivity and thickness data for thin silver films is shown in Figure 3.3A.[13,14,84,85] Also presented are the current data taken in lab for VD films deposited on silica substrates. As can be seen from the collection of data in Figure 3.3A, there is moderate variation between films even of the same nominal thickness. This is due to the variations in microstructure such as surface roughness and grain boundary concentrations arising from differences in deposition methods and substrates. The epitaxial data shown uses deposition of silver on silicon, while the polycrystalline films are evaporated onto glass substrates similar to those used here.[14] In general the current data for VD silver films on silica are consistent with previously reported data.

The plot of ρt versus t in Figure 3.3B shows a turning point with a loss of linearity that corresponds to the breakdown of the F-S model of eq 2.4 for very thin metal
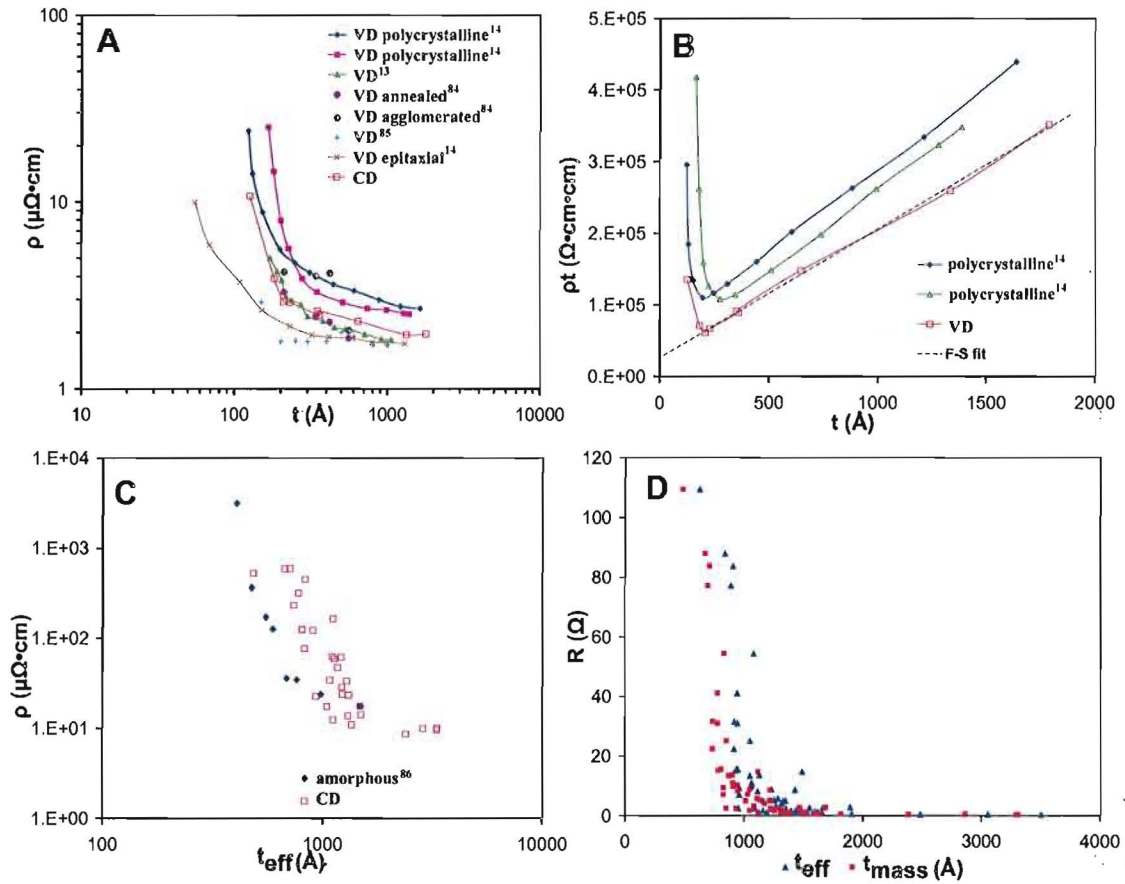
Figure 3.3: (A) A review of data in the literature for the thickness dependence of the resistivity of VD silver films.[13,14,84,85] Lines are visual aids. (B) Plotting the data in this way demonstrates the breakdown of the Fuchs-Sondheimer approximation for very thin VD silver films. Dashed lines indicate the F-S fitting. (C) The resistivity of chemically deposited films is on the same order of magnitude as the resistivity reported for amorphous silver films.[86] (D) Resistance verses t_{mass} and t_{eff} for CD films. Values of t_{mass} and t_{eff} are defined in eqs 3.1 and 3.2 respectively.

films. The thickness region of approximately greater than 50 nm exhibits a linear trend which is described by the F-S analysis. In this region the variation of ρ is dominated by surface scattering and the thickness accurately characterizes the film's geometry. The linear approximation of F-S based on thickness alone using eq 2.7 is shown as a dashed line for VD films used in this study. The fit gives a specularity value, $p= 0.17$ and an electron mean free path, $\lambda = 46$ nm, both of which are reasonable values.

For thinner films the linear approximation no longer applies yet the F-S model derived for very thin films in eq 2.8 also does not fit the ρ data. It has been suggested that the breakdown of the F-S model at a particular film thickness is due to both the greater influence of grain boundary scattering due to smaller grain sizes in thinner polycrystalline films and the increase in voids in the metal due to stopping film growth during the coalescence stage, resulting in a semicontinuous film structure.[14,57,61,63] The turning point thickness typically falls in the range of the coalescence stage of film growth for VD films, wherein A_e is significant to the film resistance.[61] For very thin films islands are present leading to a rapid increase in resistivity for extremely thin films.[64]

Due to the additional influences of network geometry and microstructure, metal films thinner than the turning point thickness are not accurately modeled using t alone. It has been suggested previously in this work that an increase in A_e suggests that an alternate geometric parameter, designated g, is required for accurate modeling of film resistivity.

Resistivity values of CD films are necessary in order to include them in these comparisons of Figure 3.3. The calculation of the resistivity from measured resistance values requires knowing the geometric parameter of the films. The surface topography evaluated using AFM reveals that RMS roughness values of each film are comparable to its average thickness. This is supported by the SEM micrographs of Figure 3.1 which show incomplete coverage of the substrate for all thicknesses deposited. Extreme roughness of the CD films, which often include granular structures higher than 500 nm, results in large errors in the AFM measurements. In light of these facts it is misleading to discuss the properties of CD films in the context of the measured thickness by AFM. The mass of silver deposited can be measured with much better precision. For substrates all of the same surface area, mass correlates directly to the thickness of a complete smooth film. For CD films mass can be used to define an average mass-thickness of the film. As an alternative mathematical description of the film's

geometry is sought, the mass of the silver deposited in each film is first used to calculate an average film thickness using,

$$t_{mass} = m_d/2A\text{d} \qquad (3.1)$$

where A is the substrate area, m_d is the total mass deposited in a given reaction, and d is the density of bulk silver (10.5 g/cm^3.) The factor of $1/2$ accounts for the silver depositing on both sides of the substrate. For simplicity and clarity we define the mass of a single sided film as $m = m_d/2$ in future equations. The calculated thickness approximates the average height of silver by assuming a uniform coating over the entire substrate area. In fact, the low points of thickness are known to be zero while high points vary hundreds of nanometers. To partially account for the porous nature of the films, the total substrate area is multiplied by the fraction of substrate area covered by the metal, A_f , which is the metal filling fraction. This correction gives an effective thickness such that;

$$t_{eff} = m/AA_f\text{d} \qquad (3.2)$$

Using this definition, the SEM images in Figure 3.1B,C,D correspond to t_{eff} values of 59, 93, and 131 nm respectively.

Filling fractions of films with measurable resistances were determined from high resolution SEM data, as in Figure 3.1, using a previously developed technique.[87] In this procedure, the images are digitally processed using linear contrast enhancement and thresholding which allows the measurement of A_f directly from SEM data. CD film results ranged from $A_f \approx 0.75 - 0.96$. This correction only approximately accounts for the porosity of the films because it is a 2-D analysis. CD films have significant thickness and cannot be treated as 2-D materials. It is actually the 3-D porosity (which is not possible to evaluate from SEM data) which should be used here. Films with lower masses (and hence smaller values of t) more closely resemble 2D networks such that this approximation is more accurate.

Figure 3.3C,D presents ρ and R vs. t_{eff} data for CD films. These values lie consistently higher than those for VD films and are very similar to data for amorphous silver films.[86] Amorphous films have elevated resistance values due to increased scattering by the lack of an extended lattice structure. The lack of crystalline structure is equivalent to a very high concentration of grain boundaries which include voids, vacancies, and lattice mis-matching and that impede transmission of electrons
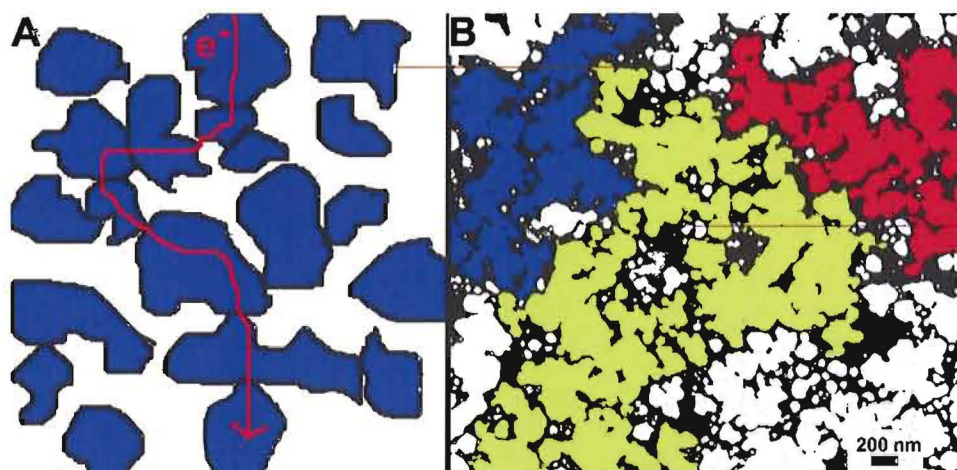
Figure 3.4: (A) shows the extended length of conduction pathways in a hypothetical granular network film. (B) The same film shown in Figure 3.1B after thresholding to black and white. Color is drop-filled using a paint bucket tool in order to show the interconnected pixels, approximating the actual available electrical transport pathways in the film.

between grains. Because the granular CD films grow from individual grains that coalesce during the growth process, they also have a high concentration of grain boundaries with grain sizes on the order of λ_{Ag} (see Chapter 5.)

The semi-continuous geometry of the film is a separate factor that also increases the resistance of the CD films. Thin metal film resistance is known to be elevated in the coalescence region of VD films due to the circuitous route through which electron transport occurs.[61] Figure 3.4A demonstrates the effect of the network structure on the length of electron transport pathways. Figure 3.4B shows the same film shown in Figure 3.1B in a way that highlights its conduction pathways. Thresholding was used to set all substrate to black and the silver film to white. Then a paint bucket tool is used to drop color into the film network such that the color spreads as far as connected pixels are available representing the limited pathways within the film. Thus both the geometry, which is related to interconnectedness, and the grain boundaries, which describe a microstructural aspect, are significant to the overall film resistance.

It is interesting to note in Figure 3.5 that the plot of ρt_{eff} vs. t_{eff} shows that CD films exhibit similar regions of conductivity to those of the VD films discussed above. The linear region as the t_{eff} approaches bulk values is preceded by the turning point and the region in which the resistance increases exponentially. While VD films can be fit reasonably based on the F-S approximation for classical size effects, CD films
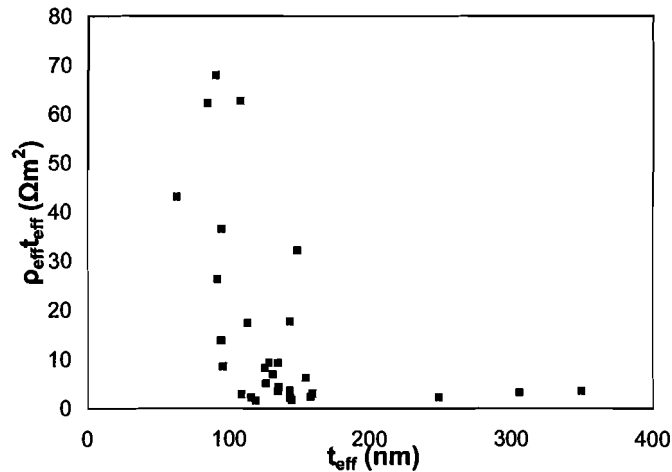
Figure 3.5: The plot of $\rho_{eff} * t_{eff}$ vs t_{eff} for CD films shows a similar trend in behavior to VD films in Figure 3.3B

do not meet the assumptions of a complete continuous layer and thus result in the calculation of large negative p values which are physically meaningless. Most of the data points in Figure 3.5 fall in the non-linear region clearly indicating that t_{eff} is not the correct geometric parameter for CD films. Of note in this plot is that the turning point occurs at a calculated average thickness of 100 nm, an order of magnitude larger than for typical VD films.

Using t_{eff} for the comparison, CD films are found to have R values 10x higher than VD films of similar average thickness. Considering the network geometry of CD films it is both questionable and difficult to limit the discussion of the measured R of CD films to comparisons with VD films. Even using t_{eff}, CD films show a wide spread in data and cannot be analyzed using the models which exist for continuous films. Rather than developing a model which applies only to CD films, a more accurate parameter, g, will be presented in Chapter 4. The value of g will relate the network geometry of CD films to R and therefore relate R to ρ. Reliable values of ρ for CD films are ultimately critical to the the comparison of CD films to the electrical properties of other forms of silver.

CHAPTER IV

GEOMETRY AND RESISTIVITY

Just as the resistance of a wire is related to its length and cross-sectional area and that of a thin film is related to its thickness, the resistance, R, of CD films also has a geometric parameter that describes the volume and arrangement of silver atoms which impacts the measured transport of electrons under bias. Because of its porous, granular nature the CD film geometry is an interplay between the amount of silver mass which makes up the films and the way in which that mass is arranged on a limited surface area. Films in which the same mass of Ag stacks thicker leave more substrate exposed, while those that cover more area are thinner on average.

The Geometric Parameter

Previous studies have shown that using t and the measured R to calculate ρ of granular and thin metal films with percolative geometry leads to anomalously high effective resistivities. The reason being that this commonly accepted approach underestimates the importance of long conduction paths in the charge transport mechanism.[61] It was also shown that re-scaling of the calculated resistivities of such films by a geometrical renormalization factor yields a resistivity value acceptably close to that of the bulk metal. The semicontinuous films with $t < \lambda_{Ag}$ presented in the study also followed a power scaling law of resistance which can be interpreted by percolation theory.[61] Studies of similarly structured metals created by thermally-induced agglomeration have also been shown to follow a power scaling law for resistance. Instead of film thickness, the fraction of substrate area exposed, A_e, was the correlating variable in this case.[88]

These two variables of m and A_e are actually present together in the analysis of both types of films. In the case of an agglomerated film, the mass of metal present (which is proportional to the value of t) is constant throughout. For the percolative VD films, t measured by quartz microbalance is inherently a mass-derived
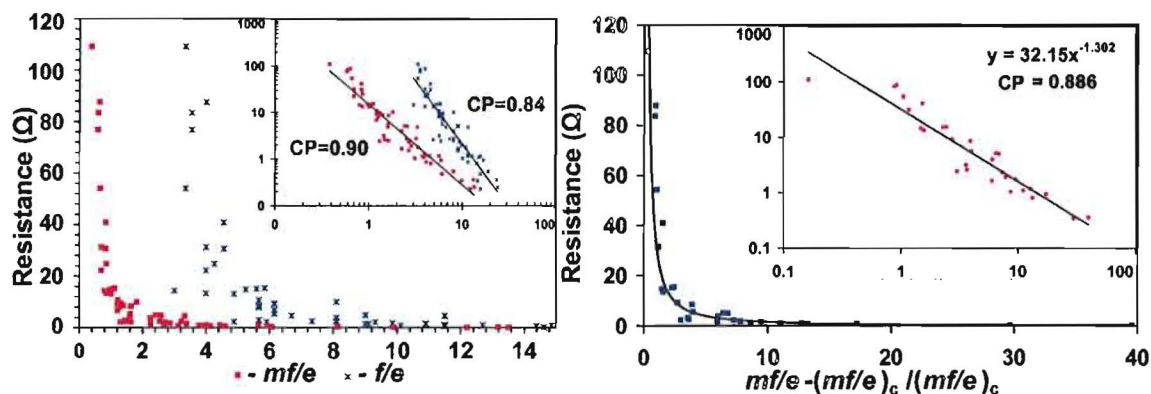
Figure 4.1: (A) The resistance of CD films shows a correlation to the ratio f/e (blue stars) which parallels the relationship between resistance and thickness for thin films. The parameter mf/e (red squares) exhibits a tighter correlation to R as measured by the linear regression confidence parameter (CP) than that of filled fraction ratio alone. (B) The relationship between R and mf/e follows a scaling law which can be explained in terms of percolation theory. The ratio f/e is defined in eq 4.1.

measurement and the additional geometry influence was acknowledged in the reported scaling factor.[61] The variables of A_e and m, (in the form of the mass-derived t_{eff}) are also used in the analysis of CD films. Very thin films such as those presented above may be approximated as 2-D. For these films A_e is proportional to R because as A_e increases the number of interconnecting pathways for electron transport decreases. We find that this trend holds true for thick, semicontinuous, network CD films which are clearly 3-D. For these films A_e may provide an rough approximation of the 3-D porosity of the film. The mass of silver present in the film is proportional to t, which is inversely proportional to R.

In Figure 4.1 CD film R is plotted against the ratio of substrate area filled by silver to that left exposed, f/e.

$$\frac{A_f}{A_e} = \frac{f}{e} \tag{4.1}$$

This ratio is found empirically to have a very similar trend with R to plots of ρ vs t for VD films as in Figure 3.3 and a stronger correlation to R than either A_e or A_f alone. This correlation suggests that f/e is related to the film geometry. The inclusion of the silver mass, m results in the parameter mf/e which is included on the same plot. The plot of mf/e results in a tighter spread of the data and improves the correlation to R as seen on the logarithmic plot inset. The correlation of 0.9, as measured by the linear regression confidence parameter (CP) is also higher than for the plot of R

vs m alone which is omitted for clarity. These data exemplify the interplay between thickness and geometric distribution of the metal. Including both a mass and a filling fraction parameter provides a strong predictor of R for the rough CD films, without explicitly accounting for scattering contributions from grain boundaries or large scale surface roughness.

The combined factor mf/e includes both the relationship to A_e and to m. This parameter is in fact a combination of the mass normalized by the filled fraction, A_f of the film, multiplied by the inverse of A_e. This factor also follows a power law with resistance for CD films as shown in Figure 4.1. It is therefore suggested that this factor, mf/e, forms a valid basis for the geometric parameter of CD films. Further support for the conclusion that mf/e forms the basis of the geometric parameter of CD films will be presented below through the calculation of ρ for CD films using the measured values of the temperature coefficient of resistance.

Temperature Coefficient of Resistance

The temperature coefficient of resistance, α, mathematically describes the impact that τ and n have upon R at different temperatures, as these are the only values in eq 2.2 which may vary with temperature. $\tau(T)$ is varied by phonons, lattice defects, and impurities which cause the scattering of electrons. For bulk metals, n is a constant with T. However, the influence of crystallite boundaries on R in eq 2.10 defines $n_{eff} = nP^{\frac{\lambda}{D}}$, where λ and P are both temperature dependent quantities. The value of α is unaffected by the shape or dimension of the material, unless those dimensions approach λ as in the case for the classical size effect.[84,89] Consequently, τ may be calculated from measured α values without the need for a t_{eff}, or any other geometric parameter. Eq 4.2 is the definition of α,

$$\alpha = \frac{1}{R_o}\frac{\partial R}{\partial T} \tag{4.2}$$

which can be applied to measured data using the following;

$$\frac{R}{R_o} = \alpha\,(T - T_o) + 1 \tag{4.3}$$

where R and R_o designate resistance at temperatures T and T_o.

Values of α are known to decrease for decreasing film thicknesses of VD films. This phenomenon is explained by classical size effects and follows the following mathematical

reasoning. Recalling the Drude model presented in eq 2.2 and using the relationship of t, R, and ρ for thin metal films where $\rho = Rt$, the equation for the resistance of a film can be written as,

$$R = \frac{m_e}{(tne^2\tau)} \qquad (4.4)$$

Combination of eq 4.3 and eq 4.4 results in the following relationship between α and τ:

$$\alpha = \left(\frac{\tau_o}{\tau} - 1\right)(T - T_o)^{-1} \qquad (4.5)$$

As with the λ_{eff} presented in eq 2.3, an effective relaxation time, τ_{eff}, can be calculated such that

$$\tau_{eff} = \left(\frac{1}{\tau_b} + \frac{1}{\tau_i}\right)^{-1} \qquad (4.6)$$

and therefore

$$\alpha = \left(\frac{\tau_{oeff}}{\tau_{eff}} - 1\right)(T - T_o)^{-1} \qquad (4.7)$$

The τ_b designates the value for pure bulk silver while τ_i indicates contributions from all types of defects and lattice imperfections and surface scattering. Scattering due to classical size effects using the F-S model is included in values for τ_i and is temperature independent. τ_b is related to phonon scattering and is therefore temperature dependent. As τ_i decreases due to surface scattering, its contribution decreases the value of the ratio of τ_{oeff}/τ_{eff} such that α also decreases. Therefore VD films show values of α which decrease with decreasing film thickness.[89]

Experiment and Results

The values of α were measured for CD and VD films in the range of 243 - 308 K. The temperature of the films was controlled by placing them on a thermoelectric cooling module equipped with a temperature controller. All measurements were taken in a vacuum chamber evacuated to 400 mTorr to prevent water condensation on the films. The resistance was then measured using the van der Pauw method for a range of temperatures. For the analysis T_o was chosen to be 273 K. The slope of the plot of R/R_o vs $(T - T_o)$ was then used to obtain the values for α_{273K}. All the results were highly linear for this range of temperatures.

Table 4.1: Temperature Coefficient of Resistance, α, for VD[89] and CD Films

VD t/l	VD $\alpha_{calc}(\text{K}^{-1})$	CD t_{eff}/l	CD $\alpha_{ave}(\text{K}^{-1})$
.1	0.0013	1.1	0.0016
.2	0.0017	1.4	0.0015
.5	0.0021	1.9	0.0017
1	0.0025	2.5	0.0018
2	0.0030	4.9	0.0018

Measurements of α_{273K} for CD films show values ranging from 0.0014 to 0.0022 $\pm$ 0.0005 K^{-1}, comparable to those previously reported for VD films with thickness near 20 nm.[13,89] This is a surprising result for films with a mass of deposited silver equivalent to that for films which are 50-200 nm thick. Classical size effects are insufficient to explain this large an alteration in the temperature related transport of CD films. Calculated and measured α values for smooth thin films previously reported in the literature are compared to the α data obtained for CD films in Table 4.1. The results obtained for the VD films we measured are comparable to those previously reported.

The α of CD films shows no correlation to the mass of silver present within the range of error and also none to the A_e as would be expected if either size effects or film geometry were a dominant influence. This analysis has not included the influence of grain boundaries whose influence on α values will be discussed in greater detail in Chapter 5.

Modeling and CD Films

Many granular areas of the silver network of CD films (as seen in Figure 3.1) have sizes $\sim \lambda_{Ag}$. Based on the average sizes observed, classical size effects in the form of surface scattering are likely to be present. The limitations of the Drude model for materials exhibiting the classical size effect and for the influence of grain boundaries have been discussed in detail in Chapter 2. For mathematical simplicity we include surface scattering in the model implicitly as part of τ_{eff}. The influence of grain boundaries must also be included due to the fact that CD films are known to have average grain sizes $\leq \lambda_{Ag}$ based on XRD data to be presented in Chapter 5. Consequently, the V-H model (below) from eq 2.10 is expected to provide a more accurate model for

CD films than the F-S model alone.

$$R = \frac{m_e}{te^2 \tau_{eff} n \left(P^{\frac{\lambda}{D}} \right)} \tag{4.8}$$

Eq 4.8 includes the grain boundary scattering term, $P^{\frac{\lambda}{D}}$, where P is a transmission coefficient $(0 < P < 1)$ describing the fraction of electrons that pass through the grain boundary and D is the average grain size.[57]

Substitution of eq 4.8 into eq 4.3 leads to a cancellation of the thickness, confirming the independence of α from the geometry of the metal. The result can be rearranged as the following,

$$\frac{P^{\frac{\lambda_o}{D}}}{P^{\frac{\lambda}{D}}} \left(\frac{1}{\tau_{bT}} - \frac{1}{\tau_{bo}} \right) = \left(\frac{1}{\tau_{bo}} + \frac{1}{\tau_{io}} \right) \alpha \left(T - T_o \right) + \left(\frac{1}{\tau_{bo}} + \frac{1}{\tau_{iT}} \right) \tag{4.9}$$

where the subscripts T and o indicate values at temperatures T and T_o respectively. The contribution of $P^{\frac{\lambda_o}{D}}/P^{\frac{\lambda}{D}}$ to α is small. Over a narrow temperature range (50 K in this study,) we estimate that the ratio $P^{\frac{\lambda_o}{D}}/P^{\frac{\lambda}{D}}$ may range approximately from 0.8-0.99 and can be reasonably approximated as 1 for this calculation. A plot of $\left(\frac{1}{\tau_{bT}} - \frac{1}{\tau_{bo}} \right)$ vs $\alpha(T - T_o)$ yields a slope and y-intercept value from which τ_{iT} and τ_{io} can be determined and thus τ_{eff} using eq 4.6. The calculated τ_{eff} can also then be used to determine λ_{eff} by the relation $\lambda = v_f \tau$. A rearrangement of eq 4.8 is presented as

$$K\rho = \frac{m_e}{\left(ne^2 \tau_{eff} \right)} \tag{4.10}$$

where $K = P^{\frac{\lambda}{D}}$. The value of $K\rho$ may be calculated directly from the value of τ_{eff}, as all the other values are constants. Then, using the measured values of R, we calculate $K\rho/R = Kg$. In this way we arrive at a calculated value of the geometric parameter determined only by the measured values of α and R. Some calculated values of Kg are compared to the values of mf/e in Table 4.2.

In order to plot the comparison of Kg to mf/e the units of mf/e (mass) are converted to length by the multiplication of the constant $1/Ad$, which equates to 4.23×10^5 cm/g for the CD films studied herein. Calculated values of Kg are plotted against measured mf/eAd values in Figure 4.2A. Due to the very high correlation between the measured and calculated parameters we conclude that mf/e is a

Table 4.2: Calculated Effective Values for λ_{eff} and ρ_{eff}

t_{eff} (nm)	R (Ω)	mf/e (g)	α (K^{-1})	λ_{eff} (nm)	$K\rho_{eff}$ ($\mu\Omega$cm)	Kg (nm)
92	21.8	0.7	.0017	24	3.8	1.7
95	2.44	1.62	.0012	17	5.3	21.3
105	9.68	1.32	.0017	24	3.8	3.8
151	1.15	3.77	.0021	29	3.0	26.4
161	1.25	4.01	.0015	21	4.2	3.4
174	0.48	6.07	.002	28	3.2	66.3
191	0.54	8.13	.0018	25	3.5	65.5
306	0.37	9.89	.0018	25	3.5	96.1
bulk	-	-	.004	55	1.6	-

significant part of the quantitative basis of the geometric parameter for the CD films. The physical meaning of the y-intercept is unclear at this time.

The definitive relationship between g and the parameter $\frac{m}{Ad}\frac{f}{e}$ leads to the question of what $\frac{m}{Ad}\frac{f}{e}$ represents physically within the film. The value m/d is the volume of silver available to be arranged on the 2-D substrate area, A. Dividing by A gives the average height of the silver if it were spread uniformly across the substrate. We speculate that the appropriate length of g for CD films is related to its 3-D porosity. The volume of total space occupied by the film, V_f, including silver and voids is obtained by dividing the volume of silver alone by its porosity, H, such that $V_f = \frac{V}{H}$. The 1-D length which characterizes g might then be designated as $g = \frac{V_f}{A}$. If this is the case then substituting $\frac{m}{Ad}\frac{f}{e}$ for g leads to a porosity of $H = \frac{A_e}{A_f} = \frac{e}{f}$. This result suggests that the ratio, $\frac{e}{f}$ may approximate the 3-D porosity of the film.

The parameters $K\rho$ and Kg may also be used to estimate the validity of the combined F-S, V-H model for CD films which is given by the following,

$$\rho = \frac{\rho_o}{K}\left(1 + \frac{3\lambda_o}{8t}(1-p)\right) \tag{4.11}$$

and which may be rearranged as below.

$$K\rho = \rho_o + \rho_o\frac{3\lambda_o}{8t}(1-p) \tag{4.12}$$

The parameter t represents the distance between scattering surfaces of the film. For a thin uniform film t is the film thickness. For the CD films there is no single
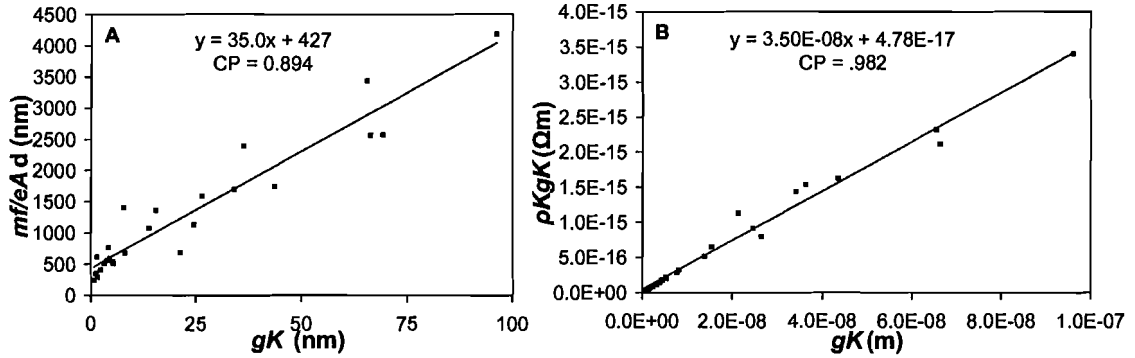
Figure 4.2: (A) A very high linear correlation is observed between the calculated Kg values and the measured parameter $mf/(e\!Ad)$. (B) The linear relationship of the F-S model calculated using the alternate geometric parameter, g, for CD films is demonstrated.

measurable value to describe the distance between metal surfaces in all the branches of the network. Generally, fitting with the F-S model proceeds by plotting eq 4.12 multiplied by t. For films which fit the model, the linear relationship between ρt and t yields a slope of ρ_o, the background resistivity of the metal. For the values which have been calculated for CD films we multiply eq 4.12 by Kg such that,

$$K\rho(Kg) = \rho_o(Kg) + \rho_o(Kg)\frac{3\lambda_o}{8t}(1 - p) \tag{4.13}$$

The term $\rho_o(Kg)\frac{3\lambda_o}{8t}(1 - p)$ is only expected to be a constant with thickness if Kg cancels the parameter t which is unknown for CD films. However, the plot of $K\rho(Kg)$ vs Kg in Figure 4.2B exhibits a high degree of linearity, suggesting that $\rho_o(Kg)\frac{3\lambda_o}{8t}(1 - p)$ is essentially constant for the films measured. The slope indicates that $\rho_o \approx 3.5 \times 10^{-8}\Omega\text{m}$ and thus $\lambda_o \approx 24$ nm. These values are approximately double and half the values for bulk silver respectively. A background resistivity double that of bulk indicates a high concentration of lattice defects within the crystallites, which we do not find unreasonable.

Additionally the y-intercept gives $\rho_o(Kg)\frac{3\lambda_o}{8t}(1 - p) \approx 4.78 \times 10^{-17}$. Dividing out all constants, $(Kg)\frac{1}{t}(1 - p) \approx 0.15$. Even if the geometric parameter, g, is equal to t, the remaining unknown values of K and p cannot be further deconvolved in this analysis. It is therefore not possible to calculate whether crystalline grain boundaries (indicated by K) or diffuse reflection (indicated by $1 - p$) is more significant to the overall resistivity. It is notable, however, that K and p are both theoretically defined

as values between zero and one such that the result of $K(1-p) \approx 0.15$ is a very reasonable one based on the order of magnitude.

We acknowledge that the analysis presented is numerically limited due to the use of approximations, yet overall the data fitting discussed above indicates that the concept of an alternate g is reasonable and that use of the newly proposed g values allows the current models to relate the resistance of highly disordered silver structures, in the form of CD films, to their resistivity. It is our intent that the analysis presented will provide insight toward a more complete understanding of the electrical properties of disordered metals and assist in the development of a complete model that accurately describes the resistivity of CD films and other disordered metal structures using measurable properties of the geometry and microstructure.

CHAPTER V

MICROSTRUCTURE AND ELECTRICAL PROPERTIES

Background

Resistivity is an intrinsic material property describing the ease of electron flow in a material under bias. The geometric arrangement of the material limits the actual transport from that which is possible in the infinite material and is measured as resistance, R. In Chapter 4 the geometry of CD silver films was described using the measured value mf/e. These values were found to be directly proportional to the geometric parameter, g, which relates R to ρ. This analysis holds for the $A_f=$ 75-95% range studied. The geometry of the film as described by g does not alter its intrinsic resistivity, but impacts the measured R. Scales on the order of λ_{Ag} in the thickness or width of network branches elevate the intrinsic resistivity of CD films due to the contribution of the surfaces to the scattering of electrons. The microstructure, including crystallite size, texture, and the character of the crystallite grain boundaries, also elevates the resistivity of the film. These two parameters were represented by K and $(1 - p)$ in the analysis of Chapter 4.

In this chapter the investigation is focused on the microstructure of the film. The V-H model proposes that the increase in ρ due to microstructure can be explained by a decrease in the effective electron density, n_{eff}, in the metal. For a material with mean grain size, D, on the order of λ, the V-H model defines the effective electron density as[57]

$$n_{eff} = nP^{\lambda/D} \tag{5.1}$$

We present again the V-H model from eq 4.8 rearranged to emphasize the relationship of a depressed n_{eff} in elevating the resistivity,

$$R = \frac{m_e}{ge^2\tau} * \frac{1}{nP^{\lambda/D}} \tag{5.2}$$

The microstructure is also found to be the source of the the depressed temperature

coefficient of resistance, α values reported in Chapter 4. Analysis of these unique silver network films will demonstrate that background defects and grain boundaries strongly influence the electrical transport and its temperature dependence in CD films.

XRD Results

High angle XRD was used to establish the mean crystallite size and the texture of CD films as compared to VD films. Representative spectra are shown in Figure 5.1 for VD films on silicon (A) and silica (B), and CD films on silica (C). The five strongest peaks for face centered cubic (FCC) silver are present in the spectra for all CD and VD films.[90] The absence of additional peaks in the diffraction data for all films further indicates that other crystalline material such as various silver oxides are not present in measurable quantities.[91]

Crystallite sizes are determined using the well known Scherrer equation,[92]

$$D = \frac{.9\varphi}{B\cos\theta} \tag{5.3}$$

where D is the mean crystallite size, φ is the wavelength of the X-ray radiation, B is the full width at half maximum (FWHM) of the peak used in the analysis, and θ is the angle at which the peak appears. Using values for the strongest peak, (1,1,1), mean crystallite sizes for the CD films were found to range from 30-69 nm. The crystallites measured here are the individual crystalline domains within the larger grains visible in SEM images as in Figure 3.1. Mean crystallite sizes for VD films were in the range of 25-58 nm and were found to correlate with the film thickness as expected. By contrast the crystallite sizes for CD films have only a weak correlation with the mass of the silver in the film. The CD film grain sizes are on the order of λ_{Ag}, and are much smaller than the t_{eff} and other dimensions, such as the width of necks and branches in the metal network (Figure 3.1). This disparity between t and grain size is not possible for VD films for which grain size scales similarly to film thickness.[67] CD films are therefore distinguished from VD films by the independent influences of their scale (in the form of surface scattering) and microstructure on their transport properties.

VD and CD films have the same diffraction peak positions yet the relative intensities of the peaks vary. Any preferred orientation of the crystallites, known as *texture*, in
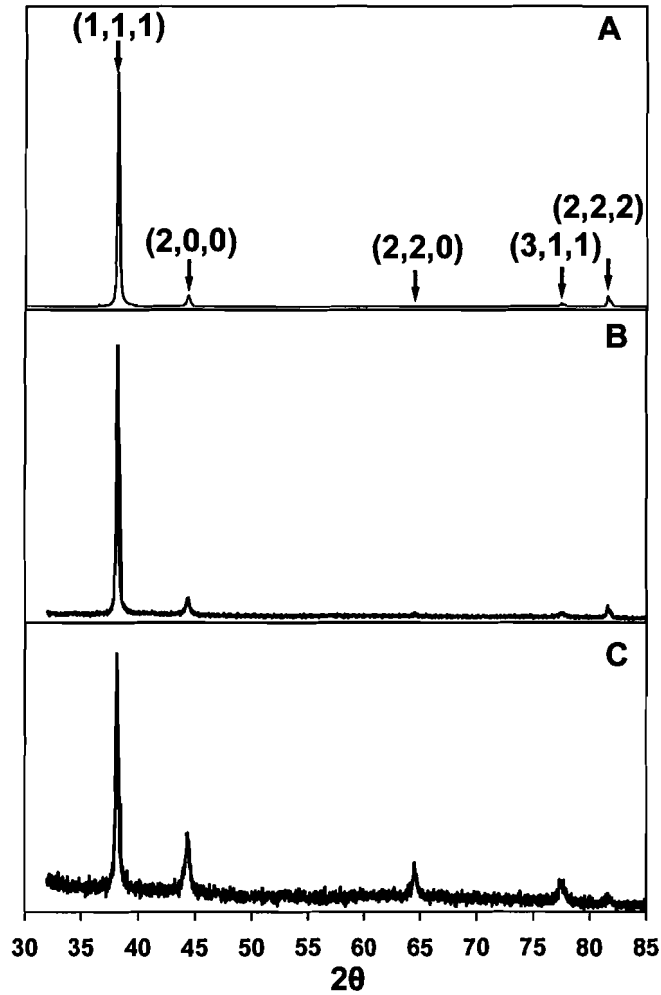
Figure 5.1: XRD spectra demonstrate the presence of crystalline silver in films vacuum deposited on A) silicon ($\sim$ 77 nm) and B) silica ($\sim$60 nm) and in C) a chemically deposited film (t_{eff} $\sim$140 nm.) The difference in the relative areas of the peaks indicates that the films have different textures.

Table 5.1: Relative Integrated Peak Intensities for VD and CD Silver Films

lattice plane	2θ (degrees)	powder std	VD (Si)	VD (silica)	CD (1)	CD (2)
(1,1,1)	38	100	100	100	100	100
(2,0,0)	44	40	7	5	44	34
(2,2,0)	64	25	0	0	18	18
(3,1,1)	77	26	2	2	21	16
(2,2,2)	82	12	6	4	2	2

the films can be assessed from the ratio of the integrated peak intensities. The calculated relative peak intensities for a powder silver standard[90] and VD and CD films are shown in Table 5.1. In general, for a face centered cubic (FCC) crystal structure the (1,1,1) peak is the strongest. Powder samples are known to have a random orientation of crystallites such that their peak ratios may be compared to measured samples to determine whether the crystallites have a preferred orientation. For the VD films, whose spectra are shown in Figure 5.1A,B, the relative size of the (1,1,1) peak is disproportionately greater than the other four peaks such that a texture with a preferred (1,1,1) orientation is evidenced. By contrast, the ratios of the peaks measured for CD films are very similar to those for powder silver standards.[90] The similarity allows us to conclude that the crystallites of CD films are randomly oriented and have no preferred texture.

Microstructure and Resistivity

The CD film microstructures are directly related to the method of material deposition. As crystallites grow and intersect during the synthesis of the film, voids and vacancies are likely to be included between crystal domains. A close up image of the intersections of two granular clusters in a CD film is shown in Figure 3.1 to illustrate the irregular grain contact that is present. The random orientation indicated by the XRD data is a sign that high lattice strain may be present.[93] In the modeling that has been presented, both the existence of grain boundary defects and high lattice strain would manifest in a decrease in the transmission coefficient, P, and consequently an increase in resistivity (see eq 5.2.) It was shown in Figure 3.3C that the resistance of CD films is comparable to that of amorphous films.[86] We now suggest that this elevated resistivity is due to the influence of the CD film microstructure as manifested in the values of D and P.

This microstructure distinguishes CD films from VD films with similar geometries such as those at the coalescence stage of deposition or those agglomerated by annealing. VD metal films have grain sizes that are comparable to their thickness due to the thermodynamics of the deposition process. The same process supports preferred textures of crystallite orientation on a substrate even when epitaxial growth is not supported. This is evidenced by analysis of the XRD spectrum of the VD silver film in Figure 5.1B. Preferred orientations result in lower contact angles between grains in VD films. Grains with lower contact angles have smaller regions of lattice mismatch

at their boundaries.[93] Consequently VD films are expected to have higher values of P and smaller increases in resistivity due to a high concentration of grain boundaries.

VD films which have been annealed to the point where agglomeration occurs have a similar network geometry to CD films[88] though on a much smaller scale. However, because agglomerated films are already annealed they have a low concentration of lattice defects, preferred microcrystalline textures, and larger, more uniform crystallite sizes.[93] CD films by contrast are studied with their as deposited structure with its particular crystallite size range, orientation, and defect concentrations. Thus, while the geometry of CD films strongly resembles scaled up examples of agglomerated or coalescence region VD films, the microstructure of each film type distinguishes them from the other two.

The relatively poor contact between grains in polycrystalline CD films can be related to the poor contact associated with the packing of silver nanocrystals in n-Ag materials.[50,51] N-Ag materials are polycrystalline silver structures produced by the arrangement of silver nanocrystals into macroscale structures such as films or pellets. The degree of compression used to create the n-Ag is described in terms of its packing density where higher compression results in higher packing densities. Studies of n-Ag and CD films have similar grain sizes.[51] Because they are produced by packing together randomly oriented crystallites, n-Ag materials are randomly textured and are expected to exhibit boundary-related defects such as voids and high angle lattice mismatches at the grain boundaries.[51] In the context of the V-H model, lower packing densities lead to lower values of P due to poor electrical contact between the grains. Because they have macroscopic dimensions overall the resistivity of n-Ag materials is dominated by grain boundaries.[50,51]

N-Ag materials have also revealed that a lower packing density of the grains leads to significant changes in the temperature dependence of resistance. Measured relative resistance values exhibit a smaller dependence upon temperature than would be expected due to phonon scattering. This can be interpreted as an effect of a lower quality contact between grains.[51]

Microstructure and the Temperature Dependence of Transport

Studies of the temperature dependence of electrical transport use the temperature coefficient of resistance to compare the behaviors of different systems. The definition

of α and values determined for CD films were presented in Chapter 4. The value of α is a constant over small temperature ranges wherein the relationship of R and T is linear. For temperature ranges significantly greater than 50 K the R vs T relationship is no longer linear. Consequently, α is actually a measure of the tangent to that curve. Values for $\alpha(T_o)$ may be determined using measured R and T values in a range of $T_o\pm25$ K. For these ranges the same graphing method presented in Chapter 4 based on eq 4.3 remains valid.

The variation in α values measured for depressed temperatures is quite dramatic for bulk silver. α more than doubles its α_{273K}value of .004 K^{-1} at temperatures below 140 K such that α_{140K} is .009K^{-1}.[51] The increase in low temperature values of α for bulk silver is a direct result of the increasing variation of R with T, $\alpha \propto \frac{\partial R}{\partial T}$. For bulk silver the electron relaxation time is the only component of R which varies with T such that

$$\frac{\partial \alpha}{\partial T} \propto \frac{\partial \tau^{-1}}{\partial T} \tag{5.4}$$

It has been reported that the relationship of eq 5.4 does not hold for n-Ag pellets composed of silver nanocrystals <50 nm with packing densities less than 100%. The reported values of α for n-Ag pellets with packing densities less than 98% did increase at depressed temperatures, but much less than the increase seen for bulk silver. Additionally, the variation in α was strongly correlated to the packing density of the pellets. N-Ag with packing densities below 92% showed almost no change in α at 140 K while those at 98% showed an increase in α of approximately double at 140 K as compared to 273 K.[51] The authors, Qin et. al., conclude that the unusual behavior of α was due to the low quality of the contact between grain boundaries as described in the V-H model.

According to the V-H model of eq 5.2, the limitation imposed by grain boundaries on electron transport can be described by n_{eff} defined in eq 5.1. In the V-H model we therefore find that:

$$\frac{\partial \alpha}{\partial T} \propto \frac{\partial \left(\tau n_{eff}\right)^{-1}}{\partial T} \tag{5.5}$$

While τ increases at lower temperatures, the n_{eff} decreases due to the larger ratio λ/D.

The value of P also decreases at very low temperatures. The ability of an electron to move through each grain boundary is indicated by the value of P. As P approaches 1, the grain boundary becomes completely transparent, having no effect on electrical transport. For values of $P < 1$, the grain boundaries manifest as a decrease in n_{eff}

and increase the resistivity of the material. At depressed temperatures, the thermal activation of the electrons is also depressed manifesting in lower transmission between grains. This equates to smaller P values further reducing n_{eff} at lower temperatures. To further clarify, for large variations in T, P is no longer a constant of the material. This last effect is the most critical in reducing n_{eff} for pellets with low packing density.[51] The decrease in n_{eff} counterbalances the increase in τ as temperature decreases and the change in α with temperature decreases compare to the bulk.

We have measured the variation of α for CD films in the temperature range 140-273 K. The portable vacuum container used for the measurements reported in Chapter 4 was also used for the low temperature measurements of α. The container was evacuated and purged with He gas twice and then evacuated to ≈ 200 mTorr. The temperature was controlled by partially submerging the evacuated container in a dewar bowl containing liquid nitrogen. The upper portion of the system
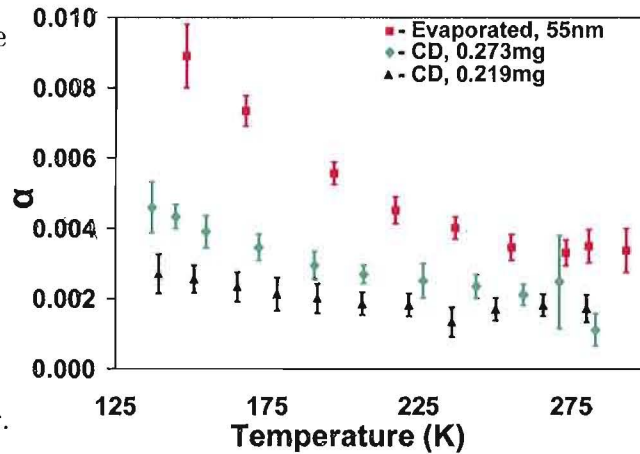
Figure 5.2: The change in α for CD films at low temperatures is significantly less than for VD films indicating a greater influence of defects at the grain boundaries of CD films.

was wrapped to minimize heat transfer. The film inside the container was in thermal contact with an aluminum block attached to the stainless steel container floor. The temperature of the film was measured using a thermocouple. The thermocouple was positioned inside the evacuated container next to the CD film and attached to the top of a silica coverslip identical to that on which the film was deposited. Once a minimum temperature for the system was reached (typically 135 K), R values were measured using the van der Pauw method at multiple temperatures as the system slowly warmed to 273 K over ~6 hours.

Figure 5.2 shows the change in α with temperature as determined for one VD film and two representative CD films. At 148 K the VD film shown has an α of 0.0089 K^{-1}, a 160% increase from its room temperature value of 0.0034 K^{-1}. This corresponds well to data reported for bulk polycrystalline silver[51,89] and suggests that the relationship of eq 5.4 holds for VD films. The CD films in contrast increase only 53% and 115%

for the same temperature difference. This is comparable to the variations seen for n-Ag with packing densities between 95 and 99%.[51] The comparison to n-Ag pellets suggests that the CD film with the increase of 115% has a higher value of P than the film that increased only 53%. Based on eq 5.2, a higher value of P should correspond to a lower measured R value, which is in fact the case for these films.

The temperature dependent behavior of α in poorly connected granular materials provides convincing evidence that an accurate model of the influence of grain boundaries on ρ must violate or modify the Matthiessen rule. The V-H model is one solution which conceptually fits the behavior observed. Though values of P can be estimated, the mathematical relationship of the unknown values P, λ , and g, in eq 5.2 prevents their direct calculation given only the present model. Based on results reported for VD films for which $g = t$, we can estimate that since P values for VD films are reported to range from 0.7-0.9[72] the value of P for CD films such as those reporting only a 53% increase in α are expected to be lower than this range. With further study, the relative difference at depressed temperatures may eventually provide a quantitative measurement of the P of a material. Such a measurement would be extremely valuable since current calculations of P for non-VD materials require significant estimation.[50]

Annealing

Annealing is often used on vacuum deposited films to stabilize the microstructural properties of the film. This occurs because the energy provided during annealing surpasses the activation energy for the surface diffusion of atoms and results in various microstructural changes.[93,94] These changes include 1) the loss of defects and vacancies within crystallites, 2) recrystallization at grain boundaries, and 3) the growth of crystallites and/or the shifting of grain boundaries. Annealing of silver films is typically accomplished at temperatures between 473-673 K, well below the melting point of bulk silver, 1234 K. If films are annealed too hot, the silver will dewet the surface and agglomerate. Due to size effects, the melting point of silver is depressed for thin films so care must be taken in selecting an annealing temperature at which agglomeration is avoided.[26,95] Annealing is used in this study to further elucidate the microstructure of CD films and the influence of defects on electron transport. By annealing at temperatures well below the point of agglomeration, smaller defects within the crystallites can be eliminated since their removal generally has a lower activation energy than recrystallization, crystallite growth, and agglomeration.[93]

Studies of annealed and agglomerated films produced by vacuum deposition show that the measured α does not change due to agglomeration.[84,96] This can be explained by the constant nature of the internal microstructure of the metal. Concentrations of defects and lattice strain are expected to be at minimum values and grain growth at a maximum after the initial annealing process, thus further annealing to agglomeration does not alter these values. These findings support the understanding that the geometry of the material does not influence α so long as the structure is electrically interconnected.

VD films which have been annealed to the point where agglomeration occurs have a visibly similar network structure to CD films.[88] Agglomerated films thus exhibit the same network type geometry as CD films. We use these films for comparison in the study of the influence of film geometry in Chapter 4. However, because agglomerated films are already annealed they have a low concentration of defects. CD films by contrast, have been studied up to this point with their as deposited structure. Therefore the changes induced by annealing provide a comparison that assists in elucidating the properties of the original films.

When significant numbers of defects and high lattice strain are present, moderate annealing will decrease the strain and allow for the mitigation of defects, leading to a decrease in the overall R and an increase in α. More specifically, λ of the film increases with annealing due to the loss of crystallite defects. According to the V-H model in eq 2.10, an increase in λ affects ρ in two ways. ρ decreases due to its proportionality to λ^{-1}. This effect is more significant than the decrease in n_{eff} that also results from an increase in λ, assuming D remains constant. The transmission coefficient, P, may also increase during annealing if the quality of contact between the grains is improved by a reduction in defects specifically at the grain boundaries. This would also contribute to lower ρ values.

Annealing studies reported for thick films of n-Au used an approximation method to calculate values for P and λ.[50] Grain growth was also reported as occurring during annealing in these samples. In the reported experiment both λ and P continually increased for higher annealing temperatures, with λ approaching the bulk value for gold only in one case. That a maximum value for P is not reached may be due to the random orientation of the nanocrystal grains. For random grain texture, the majority of grain boundaries are at contact angles greater that 15% . High angle grain boundaries above this limit are known to decrease the probability of electron
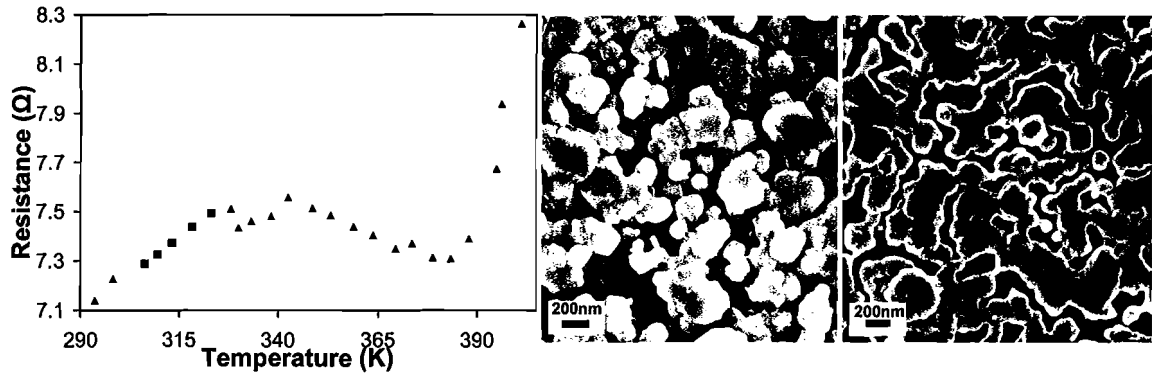
Figure 5.3: The resistance of the CD film with a t_{eff} of 111 nm was monitored during heating as an annealing test. The five square data points are used to calculate an α value of .0017 K^{-1}. SEM images of the film (A) before and (B) after annealing reveal smoother grains without significant dewetting.

transport more so than lower angle mismatches. High angle grain boundaries are not removed by moderate annealing.[93]

CD films were annealed in a tube furnace. A programmable ramp rate was used to heat the films to the chosen annealing temperature at ramp rates less than 2 K per minute. A platinum probe thermometer was placed inside the tube with the film to monitor the temperature at the actual film surface. Four point contacts during annealing were attached to the film corners using silver paint.

The microstructural changes during annealing can be monitored in a general way via the R of the film. Figure 5.3 shows the variation in R of a CD film as the temperature was increased at a rate of 1 K per minute. An initial increase in R with T is observed corresponding to the increase in phonon vibrations within the metal. The value of α (.0017 K^{-1}) calculated using the five square data points in Figure 5.3 agrees, within error, with the value of α measured before annealing began. When the temperature is sufficient to activate a loss of defects and vacancies within the crystallites and/or at grain boundaries, R levels out with temperature or even decreases. The loss of defects counteracts the continued increase in phonon resistance. This is the region that is chosen as the appropriate annealing temperature for the material. Based on the curve for the film in Figure 5.3, CD films were subsequently annealed between 353 K and 368 K. For films with grain sizes $\ll 1 \mu m$ these temperatures may also result in the movement of grain boundaries without an overall change in average grain size and may include moderate grain growth.[93] At higher temperatures a sharp increase in R is seen when the geometry of the film begins

Table 5.2: CD Film Parameters Before and After Annealing at 353 K

Film	mass	$\alpha(\mathrm{K}^{-1})$		R_{293K} (Ω)		A_f		$D_{ave}(\mathrm{nm})$		$t_{eff}(\mathrm{nm})$	
number	(mg)	before	after	before	after	before	after	before	after	before	after
CD-34	.214	.0017	.0020	9.7	7.95	.86	.83	38	39	91	91
CD-39	.349	.0015	.0024	1.3	1.00	.92	.91	49	47	148	148
CD-47	.428	.0018	.0024	.54	.40	.95	.93	41	47	181	181
CD-49	.328	.0021	.0023	1.15	.85	.92	.89	38	46	139	138
CD-51	.388	.0020	.0022	.48	.38	.94	.93	42	50	164	164
CD-103	.676	.0018	.0024	.22	.38	.94	.95	69	60	286	286

to change. The growth of voids increases R and dewetting leads to an exponential increase. Continued heating sends R out of measurable range due to the formation of metal islands which are no longer interconnected.[93,94] Upon cooling, the changes in the visible shape of the grains of the CD film heated to 400 K is shown in Figure 5.3. It is clear that the film has not undergone significant dewetting. After cooling the film displayed a moderately lower R at 293 K (6.98 Ω) than before annealing (7.14 Ω.) R data points were also measured as the film cooled back to 293 K. These data were used to calculate the value of α after annealing, which had increased to .0020 K^{-1}, indicating improved electrical contact between the grains.

The changes in R due to the loss of defects and altered geometry are irreversible. The data in Figure 5.3 was used as a preliminary test which established that CD films do follow the expected trends and begin to dewet the substrate at temperatures below 400 K. For comparison, 400 K is lower than the depressed melting point for 10 nm silver nanoparticles.[95] Though very low, the dewetting temperature is not really surprising for CD films since the silver networks are already porous and the adhesion between silver and silica is known to be weak.[26,97]

Annealing of multiple CD films with various t_{eff} values at ~353 K for 2 hours resulted in a moderate decrease in R and a increase in α. SEM analysis revealed that the A_f of the network and the XRD texture and grain sizes were nearly constant within error before and after annealing. A comparison of the exact values is shown in Table 5.2. This result leads us to suspect that the changes measured in the transport properties are primarily due to the loss of defects in the polycrystalline microstructure. These defects could include single vacancies within the crystals as well as vacancy clusters and small pores at the grain boundaries resulting in improved contact between grains. Therefore the change in R cannot be specifically attributed to only λ or P, but may involve changes in both.

The low temperature values of α for a CD film after annealing support the conclusion that most of the changes occur within the crystallites. The values for α_{150K} for an annealed CD film with 0.297 mg deposited Ag shows an increase of 80% from its α_{280K} value of 0.0028 K^{-1}. This percent increase is less than half that measured for VD films. In fact the specific values for α correspond precisely to data for a n-Ag pellet with a packing density of 98.8%. This indicates that poor contact between grain boundaries is still significant in the annealed CD film. The increase in α_{280K} to 0.0020 K^{-1} compared to the pre-annealed value of 0.0017 K^{-1} and the decrease in overall R of the film with no measurable alteration in geometry, provide evidence that defects have been removed. The reasonable conclusion is that for the moderate annealing applied, the primary change in the CD films was a loss of defects within the crystallites themselves resulting in an increase in λ. Small changes in P, however, are also possible.

Summary for CD Films

Data describing the crystallite grain sizes and orientation of the grains in CD films combine with the low temperature α and annealing data to provide a convincing case that the influence of microstructure on the electrical properties follows the model of Vancea and Hoffmann. Grain sizes are of the appropriate scale to influence resistivity and their random orientations further limit conduction across the grain boundaries. The mitigated change in α at liquid nitrogen temperatures affirms that poor electrical contacts exist between clusters of silver grains. Also, the electrical contacts between clusters are only moderately improved by annealing. These results explain the elevated resistivity (twice that of bulk silver) obtained by applying the F-S model to CD films.

It is important to note that the application of the F-S model with such reasonable results was only possible through the determination of the geometric parameter which accurately relates measured resistance to resistivity for disordered CD films. For these films the value of g determined was directly proportional to the phenomenological parameter mf/e. Because the networked shape of the silver in CD films cannot be described with a straightforward geometrical length measurement, phenomenological analyses might provide the only straightforward estimate of the value of g. The mf/e parameter is directly related to the mass of the film, and its filling fraction, or to think of it another way, mf/e expresses the balance of how much silver is present

and in what way it is arranged on the films. Such a parameter is limited to films within a particular range of measurable filling fractions, but is highly valuable for its correlation to resistance within that range.

The influence of scale is present in CD films both in its microstructure and in the value of g which are both on the order of λ_{Ag}. The applicability of the F-S model indicates that the distance between scattering surfaces is also on the order of λ_{Ag}. This is supported by SEM images which show that the width of the necks of silver throughout the film are often less that 500 nm. The scale, geometry, and microstructure of CD films are each important parameters which may be useful in the development of optimized electronic materials.

Using the results for flat films, Chapter 6 will begin the process of a comparison between films grown on a planar silica substrate to those grown on spheres of silica. The synthesis of spherical silver shells is chemically identical to that of flat films. The deposition method was in fact developed primarily for spheres rather that films. Therefore is worthwhile to explain the synthesis and its implications for spherical colloids in detail before beginning a discussion of electrical properties in Chapter 7.

CHAPTER VI

SYNTHESIS OF SILVER CORE-SHELL MATERIALS

Background

The exploration of novel applications for nanoscale metallodielectric core-shell materials provides one of the original motivations for the studies of CD films presented in Chapters 3, 4, and 5. The electroless deposition of silver used to produce CD films was originally developed for use on nanospheres of silica.[82] The properties of silver nanoshells deposited by the same method are now explored in light of the results presented for CD films. The present chapter discusses the discoveries pertaining to the synthesis of silver nanoshells. A comparison to CD films including the electrical characterization of these materials will be presented in Chapter 7 with an additional synthesis of gold nanoshells presented in Appendix A.

The motivation to elucidate the properties of metallodielectric core-shell materials lies in their potential for both novel optical and electrical properties, as discussed in Chapter 1. The investigations presented in this chapter focus specifically on metal nanoshells of silver coated on silica spheres with diameters of 250-1000 nm. There are multiple parameters that endow these materials with their unique blend of properties. The optical response of metal nanoshells is sensitive to both the size and the geometry of the metal. Their nanoscale to mesoscale size range influences their optical properties through a geometrically tunable plasmon resonance. Due to their spherical shape, the extinction spectra of the shells behave differently than those of silver nanoparticles or silica alone. These spectral differences are due to the behavior of the surface plasmon modes which are sensitive to both the geometry of the metal and its chemical environment.

The organization of the nanoshells into aggregates or higher order structures also alters the optical response. Higher order structures of nanoshells include microscale crystal arrays whose optical behavior is predicted to allow the synthesis of photonic crystals and waveguides.[21,34,98] With the various levels of size, geometry, and microscale

structures, the properties of nanoshells present many facets for discovery and material design.

The initial step in the design process is the syntheses of the silver coated spheres to be studied. Other methods for the deposition of silver nanoshells have been presented in the literature.[24,29-32] Attempts to reproduce two of them[24,31] have resulted in silver shells which were considerably less uniform and complete than those reported. Additionally the success rate for shell formation was low and inconsistent. These results led to the development of the synthesis method now reported.

Most established methods for the deposition of metal shells involve seed metal nanoparticles organically tethered to the surface, such that organic materials and sometimes even multiple metals are incorporated into the core-shell structure.[24,32,34-39] The impact of organic ligands and seeds of a different metal on the electronic transport and optical properties of core-shell materials has not been thoroughly studied. Since the optical properties of metal nanoshells are highly sensitive to their chemical environment it is advantageous to develop fabrication protocols that produce pure two-component inorganic metallodielectric particles. The stoichiometrically controlled (SC) synthesis we have developed meets this standard while requiring only one step in the deposition process. The scientific value of limiting the number of variables in any experiment is a well understood precept and the SC synthesis was developed with this in mind.

In nanoscale core-shell systems both the electronic and optical properties depend mainly on the nanoshell morphology, as well as on core-shell size and ratio.[87] The SC method results in nanocrystalline silver shells with controlled thicknesses ranging from 20-140 nm. The thin shells are typically composed of semi-continuous clusters, exhibiting incomplete surface coverage. As shell thickness increases with additional silver deposition, a rough, interconnected thick shell morphology results. Both thin and thick shells are polycrystalline aggregates and therefore highly granular. The rough network morphology of these shells reflects the growth process of the deposition as has been discussed for the CD films deposited using the same reduction reaction.

The SC fabrication method credits the Tollen's reaction and recent work based on this reaction for the idea that silver may be deposited directly onto silica without the previously used seeding step.[36,41] The classic Tollen's reaction for silver reduction is kinetically fast, which has made it a valuable test for the presence of aldehydes. One consequence of this is that the formation of silver may occur as nanoparticles in solution. It has been previously reported that the reduction of silver directly onto

spheres can lead to highly uneven shell growth as well as spontaneous nucleation of silver nanoparticles in solution.[32] Metal seeds or pretreatment steps have been used to increase the thermodynamic favorability of nucleation of silver at the surface of the spheres.[32,35] We find that the electroless deposition can be modified to encourage silver deposition at the sphere surface without seeds or pretreatment. Using these modifications we are able to adjust the kinetic parameters of the silver reduction, leading to even growth of rough, granular shells in a single step, without extra nanoparticles in solution. Two different combinations of deposition parameters were developed to produce nanoshells. One method relies on very low reaction temperatures and is presented in the literature as the temperature controlled (TC) method.[82] The SC method which is the focus of this chapter uses low concentrations of reactants in precise stoichiometric ratios, the details of which will be discussed in greater detail later.

Although no seeding step is used, the reduction of silver onto the spheres begins with silver growth resembling the seeding used in previously reported methods.[32,35–37] Once shell growth is complete, the measured optical extinction of such shells exhibits coherent optical response, which is due to the excitation of tunable multipolar plasmon resonances in the disordered silver nanoshells. This optical response persists despite the disorder within the metal shell. We report that the optical response is tunable based on the core size and the shell thickness. The experimental details of the synthesis are described below.

Experimental

Silica particles of diameters 250, 530, and 1000 nm and polydispersities of 1-3% were prepared by the Stöber synthesis[99] or purchased commercially. All solutions were prepared under stirring, using 18.1 MΩ-cm ultrapure water. Silver nitrate was obtained from Alfa Aesar. Concentrated ammonium hydroxide and glucose were obtained from Aldrich.

The following Tollen's reaction was employed:

$$RCHO(aq + spheres) + 2Ag(NH_3)_2OH(aq) \rightleftharpoons 2Ag(s) + RCOONH_4(aq) + 3NH_3(aq)$$
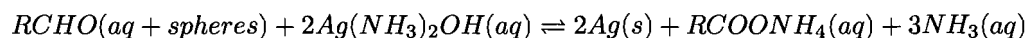
The stoichiometrically controlled method (SC) for growth of silver on silica spheres was used as follows. The concentration of $AgNO_3$ required for each reaction was calculated to stoichiometrically limit the quantity of silver and therefore the thickness

of the shells. Reactions were carried out in approximately 30 mL of solution. For different sphere sizes a constant ratio of sphere surface area to volume of reaction solution was maintained at approximately $2 \times 10^{-4} m^2/mL$. This led to $AgNO_3$ concentrations on the order of 2 mM. The $AgNO_3$ was mixed with the spheres and 50 μL of saturated glucose solution. While stirring 50 μL of 3% NH_4OH were added to this mixture to begin the reaction. The pH, as determined with pH measuring strips, was near 8. Once the reaction had started the solution turned yellow-brown in color. The color progressed again through brown to dark gray. The pH approached neutral value when the reaction was completed. Centrifugation was used to separate the coated spheres from the supernatant. The washed products were then re-dispersed in a known volume of either ultrapure water or ethanol. A JEOL JSM-6300XV scanning electron microscope (SEM) system was used to image the spheres for analyzing shell morphologies. Transmission electron microscope (TEM) studies were conducted with a Phillips CM12 at 80-120kV. Extinction spectra of silvered spheres were obtained by dispersing the particles in either ultrapure water or ethanol, in 0.5cm quartz cuvettes.

Deposition Results

The SC coating method is found to have good control of the thickness of the metal shells based on the stoichiometry of the reaction which limits the silver available. The SC uses a reaction similar to one previously reported for producing silver nanoshells on seeded spheres.[24] In this case, however, no functionalization with organic monolayers or seeding with gold nanoparticles is used and glucose replaces formaldehyde as the reducing agent. The reaction parameters tracked during silver deposition include sphere size, reactant concentrations, reaction time, the total sphere surface area in solution, total volume of solution, and pH. Typical reaction parameters are shown in Table 6.1. Since silver reduction requires an elevated pH, the standard Tollen's reaction uses NaOH to create a basic environment. For the SC method the NH_4OH functions as the source base as well as a reactant such that no NaOH is required.

The homogeneous nucleation of silver nanoparticles in the solution is a known competing process with heterogeneous nucleation at the sphere surface.[32] Nucleation at an existing surface interfaces reduces the energy barrier for silver formation.[100] However, if the energy barrier for nucleation at the surface is not significantly lower than for nucleation in solution, a kinetically fast reaction will reach a higher saturation of reduced silver and result in both nucleation types. The results of test reactions,

while developing the SC protocol, fell into three categories, nanoparticle formation in solution (an intense yellow solution,) deposition on spheres (a dark gray solution,) or both (dark gray with a yellow cast.) These results were determined using TEM analysis. It was confirmed experimentally that slowing the reaction rate minimizes nucleation in solution and nucleation at the surface is preferred. The kinetics for nanoparticle formation are slowed by the use of very low concentrations of silver nitrate and by replacing formaldehyde with glucose. Glucose is a larger molecule with lower accessibility to the aldehyde group involved in the reaction. Using the SC method, silver deposition occurs only on the silica surfaces.

Silvering takes place relatively quickly, generally in 10 minutes at room temperature compared to 30 minute or greater reaction times required by the TC method.[82] The SC reaction time can be extended to 40 minutes by cooling the reaction solution in ice before addition of the ammonia.

EDS of coated spheres, as compared to that performed on 99.99% pure silver in bulk form, revealed highly similar (and negligible) levels of carbon, typical to environmental contamination. These findings strongly indicate that glucose is not permanently incorporated into the shells in these reactions.

Results of typical SC coating on 530 nm silica spheres are presented in Figure 6.1 both in TEM and SEM micrographs. The rough shells are composed of rounded polycrystalline aggregates as shown in Figure 6.1A. In general, thicker coatings tend to yield rougher shells which are more likely to exhibit the elongated grains seen in Figure 6.1B. The thickness of the shells has been determined using TEM image sizing techniques. The coated and uncoated sphere diameters were measured using an in-house written program,* which averages out the roughness of the shells in order to estimate an average shell thickness. A total of 100-200 spheres were used to obtain the average shell thickness. The resulting polydispersities were typically near 4%. This confirms that although thick silver shells are considerably rough and porous, the silver growth occurs uniformly on all spheres, with no significant deviations from the underlying spherical symmetry of the silica cores.

---

*We use a modified Hough transform with a variable-radii circular kernel to map the thresholded-binary edge map of a grayscale image onto a maximum likelihood data cube. By scanning the data cube for its highest values we retrieve the most likely center positions and radii of circular objects in the image. The procedure was adapted from Pistori's Hough Circle plugin (H. Pistori, http://rsb.info.nih.gov/ij/plugins/hough-circles. html) for the ImageJ program written by Rasband (W.S. Rasband, ImageJ, US National Institutes of Health, Bethesda, MD, USA, 1997-2006, http://rsb.info.nih.gov/ij/).

Table 6.1: Typical Reaction Parameters for SC Silver Deposition

sphere size(nm)	260	530	1000
calculated shell thickness (nm)^a	40	100	108
$AgNO_3$ (mM)	1.5	2.0	2.0
36% glucose (μL)	20	20	20
3% NH_4OH (μL)	20	20	20
total volume of solution (mL)	20	34	40
surface area/volume (m^2/mL)	4.1×10^{-4}	2.1×10^{-4}	2.6×10^{-4}

a. Calculated thickness includes adjustment for 10-20% typical shell porosity.

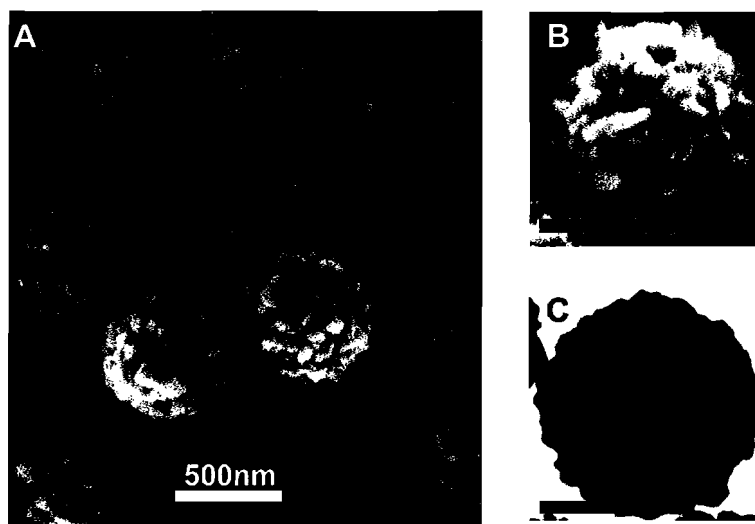Figure 6.1: (A, B) SEM images demonstrate the range of morphologies from (A) rounded to (B) elongated clusters observed coating 530 nm silica spheres with the SC. Shell thicknesses are (A, C) 102 nm and (B) 140 nm all on 530 nm silica spheres. Elongated clusters have a typical length of 100 nm. (C) TEM shows the outline of surface roughness for the same batch shown in (A). All scale bars are 500 nm.

SEM data further allow the relative surface coverage to be measured in terms of the average metal filling fraction, A_f, similar to the analysis done for CD silver films.[87] Sphere images such as in Figure 6.1B are digitally processed using linear contrast enhancement and thresholding. The edges of the sphere are cropped in order to analyze only the central, least shadowed area of the coated sphere as a 2-D projection. This allows an estimation of A_f directly from SEM data. Shells of average thickness near 100 nm were found to have A_f values in the range of 80-95%. As with CD films, this 2-D measurement is actually used as an estimate for the 3-D porosity of the shell. The thickness of the shells is controlled stoichiometrically by the volume of silver added to the reaction in the form of silver nitrate, yet it is noted, based on trial and error that the resulting porous shell thickness is systematically $\sim$30% greater than that predicted from stoichiometry. This is not surprising considering that our calculation assumes a complete, solid silver shell as the end product. The porosity of these shells has been independently estimated by modeling their linear optical response.[87] Extinction spectra were analyzed using a core-shell Mie scattering model,[25] with A_f as a single fitting parameter. The resulting porosity was estimated at 10-20%. This value both corresponds to the A_f determined by SEM image analysis and is equivalent to a 25-33% increase in shell thickness. These results are in excellent agreement with our reported observations.

Comparison of the shell morphologies with previously published methods can be difficult when only TEM images are presented. The common use of SEM imaging is a recent and much needed development in the study of nanoshells. Some previously published silver nanoshells are clearly of lesser coverage and granular[32,35] while others appear to be more uniform in outline[24] as shown by TEM. As can be seen in Figure 6.1, the difference between SEM and TEM images is pronounced. SEM data offer a clear representation of detailed surface morphology, which is often not available from TEM images. We have used here TEM images only for the analysis of shell thicknesses while SEM images were used for visual analysis and the measurement of A_f.

For reactions with a calculated thickness greater than 100 nm, nanoparticles occasionally form in solution accompanying the shell deposition. The free nanoparticles in these cases could be eliminated by centrifuge separation. The shells obtained as the end product were, however, thinner than calculated, due to the significant loss of silver to free nanoparticle formation.

The silver of the SC nanoshells adheres well to the surface of the sphere after centrifugation and sonication. After longer than a few weeks in solution, irreversible

aggregation of the spheres is often observed and silver is lost from the shells upon attempting ultrasonic re-dispersion. Silica spheres of 1 μm-, 530 nm-, and 260 nm-diameter have been effectively coated using this method. Reaction results were most consistent when the ratio between the total surface area of the spheres to the total volume of the reaction solution was maintained within an order of magnitude of $2 \times 10^{-4} m^2/mL$. This parameter was determined experimentally and the underlying principle behind it is not clearly understood. We speculate that this ratio contributes to the kinetics of the reaction and therefore plays a role in whether nucleation occurs in solution or at the surface of the spheres.

Extinction Behavior

The characterization of the silver nanoshells synthesized by the SC method required multiple perspectives on the material properties. The optical behaviors of the spheres are considered first, while the electrical behaviors will be considered in Chapter 7 with a comparison to the electrical studies of CD films on flat substrates from Chapters 4 and 5.

The excitations of surface plasmon modes at the metal surface is a readily measurable optical property of metal nanoshells using UV-vis spectroscopy. The surface plasmon resonance (SPR) of a metal occurs due to collective excitations of conduction electrons bound to the surface of a metal. This excitation, observed as a peak in the extinction spectrum, gives metal nanoparticle solutions their characteristic colors. The SPR of nanometer scale metals provides the basis for many applications, including bio- and chemical sensing.[7,47,48] Unlike the plasmon resonance of metal nanoparticles, which depends weakly on particle size, SPR of nanoshells may be tuned by independently adjusting the core size and core-shell thickness ratio. The SPR tunability of core-shell structures spans the entire range of visible wavelengths as well as the infrared, suggesting a broad range of potential applications. A typical UV-vis spectrum for shells 70, 110, and 125 nm thick produced using the SC method on 530 nm-diameter spheres is shown in Figure 6.2. This spectrum also demonstrates that the SPR of the SC shells may be tuned through the shell thickness, similar to previously reported geometrical tunability in smooth complete nanoshells.[24]

Spheres decorated sparsely with seed nanoparticles exhibit a resonance at 420 nm, characteristic of individual silver nanocrystals as seen in Figure 6.3A. Because of the dilute metal surface coverage, the excitations of the nanoparticles are independent of
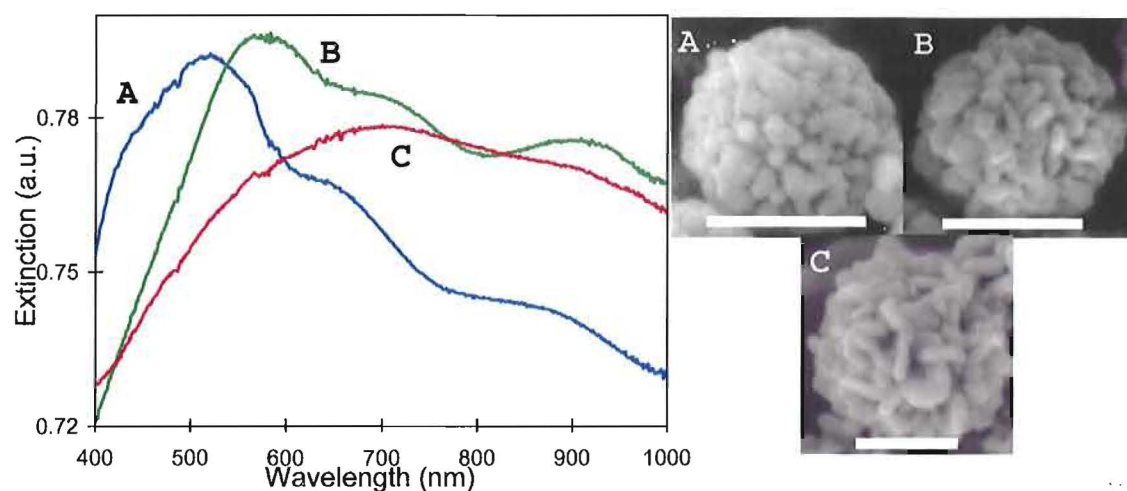
Figure 6.2: Extinction spectra and SEM micrographs of 530 nm silica spheres coated with (A) 70, (B) 110, and (C) 125 nm of silver and dispersed in ethanol, demonstrating spectral tunability based on the thickness of the silver shell. SEM micrographs of typical shell morphologies are shown for each size. All scale bars are 500 nm.

the sphere size. Figure 6.3B shows the extinction spectrum for 40 nm silver shells on 260 nm-diameter spheres obtained by SC deposition. This spectrum is comparable to previously reported spectra of thin nanoshells with similar core size.[32] The primary absorption peak is observed at 460 nm, rather than 420 nm, indicating that the SPR of the shell is not the same as that for isolated nanoparticles, but rather is influenced by the overall shell geometry. The SPR of the shells in Figure 6.2 differs even more dramatically from that of individual silver nanoparticles.

Previously reported smooth and complete metal shells have demonstrated the existence of a spherical shell plasmon which can be modeled with Mie scattering theory.[101–103] It has been shown that incomplete shells do not support geometrical resonances such as those which have been modeled by Mie theory, exhibiting instead strong aggregate-broadened absorption.[34] In Figure 6.2 and also in Figure 6.3B,C, the spectra are core-shell multipole modes (Mie resonances), typically observed in light scattering experiments using high optical contrast layered particles. The extinction spectra of thick, porous shells such as those in Figure 6.2 and 6.3B and the thin, discontinuous shells as in Figure 6.3C are each markedly different from the previously modeled smooth and complete shells, yet also differ from aggregate-broadened absorption.

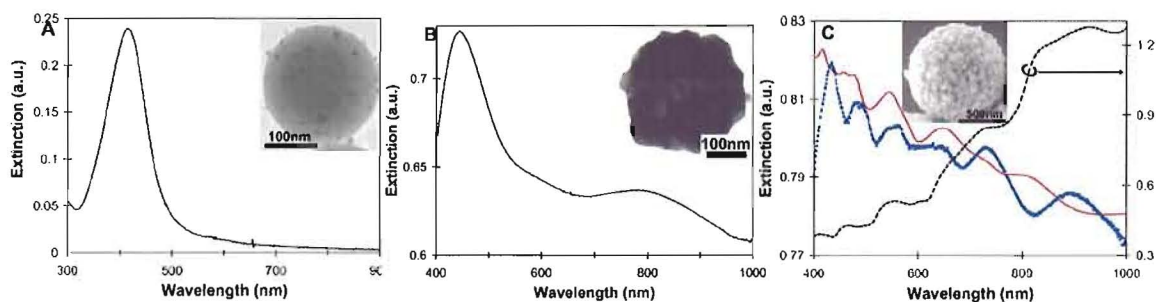Figure 6.3: (A) The extinction spectrum of seeded spheres shows the characteristic peak of isolated silver nanoparticles. (B) Extinction spectrum of 260 nm silica spheres with 40 nm average shell thickness. (C) The extinction spectrum of 1 μm spheres with 20 nm average silver shell thickness demonstrates the influence of the shell morphology on the optical response. The measured extinction is denoted by blue triangles. The solid red line shows a calculated spectrum using the fractal shell model,[87] while the dashed black line shows the same extinction spectrum calculated assuming a uniformly spherical silver shell. All spectra are of spheres dispersed in water. Insets are typical spheres from the respective batches.

The spheres with thin shells shown in Figure 6.3C are produced by the TC method with an average shell thickness below 50 nm. The A_f values are near the percolation threshold and so the dielectric function characterizing their optical response depends strongly on their morphology. Thin metal films near the percolation threshold are known to support plasmonic excitations which are localized to the metal clusters in the films.[104] When such films are grown into a fractal nanoshell geometry, coherent optical driving of cluster-localized plasmons through core-shell multipole modes is observed.[87] Although the shell is strongly disordered and incomplete, a collective optical response as seen in Figure 6.3C is achieved. Also apparent is that the standard approach for modeling the extinction assuming a solid, bulk silver shell yields poor agreement with our experimental data, while the fractal shell model agrees very well. This model also shows that the morphology of the disordered silver nanoshells largely determines their plasmon excitation.[87]

For the thicker (>50nm) SC shells of Figure 6.2 we see that the multipolar plasmon resonance of the shells differs from both complete spherical shell model and the fractal shell model. Slight modifications to the modeling, taking into consideration the porosity of the shells in terms of an effective dielectric function, have shown remarkable agreement with classical core-shell Mie scattering theory.[87] It is of note that although shell roughness increases significantly with thickness, geometrical resonances may still be observed when the shells are as thick as 125 nm or greater.

This indicates that the role of surface scattering due to roughness is mitigated in the presence of strong optical coupling to core-shell resonances. We find that although the shells possess significant irregularities, the signature plasmon spectrum of these core-shell systems is conserved to a high degree.

Solvent Studies and Aggregation

Because of their unique SPR, the UV-vis extinction spectrum of metal nanoshells in solution provides a valuable characterization tool. Monitoring the extinction spectra of SC silver coated spheres allows us to track the changes occurring during storage of silver coated spheres over time. Figure 6.4 shows changes in the shape of the extinction spectra after storing the nanoshells in ethanol and water. While significant modification is observed for particles stored for 11 days in ultrapure water, only slight changes are visible for particles stored for the same duration in ethanol. This change is the result of irreversible aggregation and loss of silver nanoparticles from the shells into solution over time. The pronounced peak centered near 420 nm in the red line of Figure 6.4A is identified as the SPR of free silver nanoparticles in solution. The broad width of this

Figure 6.4: Extinction spectra of spheres stored in (A) water and (B) ethanol taken on day 1 (blue) and after 11 days of storage (red), demonstrating the longer lifetime of SC nanoshells in ethanol. The average shell thickness is 100 nm on 530nm silica spheres. Inset is a TEM of a typical sphere from this batch.

peak indicates that these nanoparticles have undergone significant aggregation. The possibility of storing the coated spheres in dimethyl sulfoxide was also tested, exhibiting results similar to those of water storage. Based on these findings, we have stored our materials in ethanol, where degradation of the shells is slowest.

The likely cause of the increased visible aggregation in water and DMSO is related to their polarity. Of the three solvents ethanol has the lowest dipole moment at
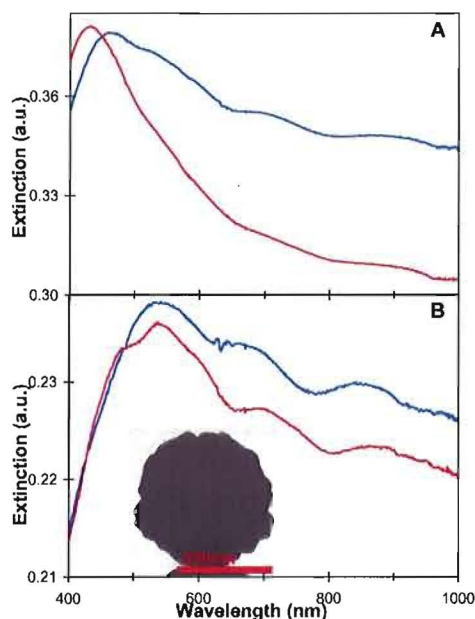
1.68 Debye units. Water and DMSO are 1.85 and 3.96 Debye units respectively. Solvent polarity is well known to influence the stability of metal nanocrystals.[105] We expect the metal on the spheres to be easily polarized just as individual silver nanocrystals are. Water and other polar solvents may induce charge separation in the shells leading to attraction between particles. This theory is supported by the observation that DMSO was the most difficult solvent from which to redisperse the coated spheres, requiring the longest sonication times. Non-polar solvents have not been tested to date.

Other methods of stabilizing spheres in order to prevent aggregation during storage in solution were also investigated. In the case of metal nanoparticles, the most common method used to prevent aggregation is the use of organic monolayers which passivate the metal surface. Citrate ion solutions and polymers have also been shown to help prevent aggregation. It has been observed that for larger metal nanoparticles, organic monolayers can be less effective at preventing aggregation.[105] The silver coated spheres are orders of magnitude larger than such nanocrystals. It is likely that ligand passivisation does not interfere with the interactions of the silvered spheres on a scale sufficient to deter aggregation.

Testing of the influence of various water based solutions on coated spheres over time supported this conclusion. Six different solutions including organic ligands, polymers, and salts were compared for their ability to preserve coated spheres. Again, UV-vis was used to monitor changes in the extinction of the sols. Based on their prior use to stabilize silver nanoparticles the following solutions were tested: polyvinyl pyrrolidone (PVP), polyvinyl alcohol (PVA),[106] sodium citrate,[107] sorbitol,[36] mercaptoethylphosphonic acid,[108] and mercaptoethanesulfonic acid.[109] After 20 days the PVA and PVP solutions maintained the same UV-vis spectra. All other solutions were ineffective at preventing aggregation. The sorbitol solution accelerated complete aggregation such that spheres could not be redispersed at all. While storage in the polymer solutions does appear to preserve the core-shell structures longer than pure ethanol, separation of the spheres from the solution and removal of the polymer after storage present another challenge which we have not addressed.

CHAPTER VII

ELECTRICAL PROPERTIES OF SILVER SHELLS

Background

The synthesis of SC shells and CD films use the same modified Tollen's reaction for the electroless reduction of silver at their respective spherical and flat silica surfaces. The sphere and cover slip substrates are highly similar chemically having hydroxylated silica surfaces. The fundamental difference between them is the geometrical aspect of a spherical versus a flat substrate. Physical comparison of the two resulting films reveals that the curvature of the sphere surface influences the scale of the granular silver cluster sizes, but not the network geometry of the resulting shell or film. This comparison is based on SEM micrographs of spheres and films with similar thicknesses. A straightforward visual presentation of the shells and films is shown in Figure 7.1. The values for flat film average thicknesses are based on AFM data. Inspection reveals that films and shells of <130 nm exhibit similar network cluster morphology, but with notable differences in scale. Films on flat substrates have much larger clusters of silver than those on spheres.

Seeking an explanation for the development of larger silver structures on flat substrates, we consider the implications of the curvature of the spheres and their suspension in solution on the diffusion of silver ions near the substrate. Imagining the flat 104 nm film shown in Figure 7.1 to be flexible and wrapping it around a curved surface, one can see that the large clusters would protrude significantly from the curved surface and space would be present between the clusters. The curvature of a 530 nm sphere is essentially flat from the perspective of the first diffusing atoms reaching the silica surface. However, the motion of nanoscale spheres in solution, as opposed to a single macroscale surface, allows many more angles of approach for silver ions. Consequently the concentration of reduced silver near the surface is rapidly replenished after being depleted by silver nucleation and deposition. In essence a greater concentration of reduced silver is available at the sphere surfaces

71nm **103nm** **110nm** **136nm** **170nm**

68nm **104nm** **110nm** **133nm** **180nm**
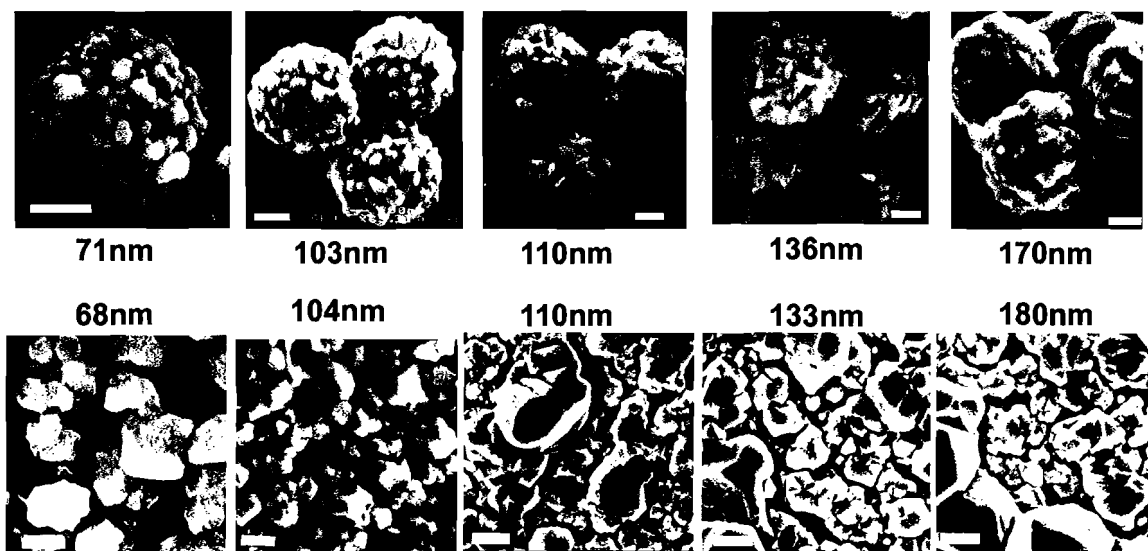
Figure 7.1: SEM micrographs of spheres and films are compared for similar thicknesses. All scale bars are 200 nm.

as compared to a flat substrate. We speculate that cluster nucleation and growth on the sphere surface results in smaller more closely spaced clusters due to the elevated concentration of reduced silver, which in turn results from a combination of the sphere curvature and its colloidal suspension in solution.

The similarity in the network structure of flat and spherical films is quantitatively verified by measurement of A_f. Using the same method previously mentioned in Chapters 3 and 6, A_f values for spheres and films have been measured using digital analysis of SEM images. Silver coated spheres with an average thickness near 100 nm were found to have metal filling fractions in the range of 80-95%. These values correspond well to those observed on flat CD silver films which range from 75-95%.

This comparability breaks down at higher film thicknesses. As cluster sizes grow, the areas of the cluster which are available for additional growth are limited by diffusion. In both cases the available ion concentration will decrease closest to the silica surface first. This effect is less pronounced, though, on the curved surfaces. The areas of a cluster that are closer to the silica sphere surface have higher availability for the diffusion of ions than those on the flat surfaces. The result is a difference in cluster aspect ratios that becomes more dramatic as film thickness increases. For films and shells greater than 110 nm, inspection of Figure 7.1 reveals a deviation in morphology. The needle-like clusters of the 136 nm shells have not been observed on flat substrates at any point. For very thick shells such as the 170 nm shell, A_f is

visibly increased and approaches 100%. In this case A_f is no longer representative of the 3-D porosity. Instead the lateral growth of clusters cover the voids beneath. The A_f of the 180 nm flat film remains at 91% indicating that the clusters of thick films grown on flat substrates develop a greater height to width aspect ratio compared to those on spheres for very thick films. Less lateral growth is available to the films on flat substrates. As clusters grow and some overhangs develop diffusion close to the silica substrate is further limited. Silver ion concentrations remain highest near the faces of the silver clusters that are already protruding from the surface. The result is increased roughness and moderate growth of overhangs rather than a smoothing of the film. Similar growth of roughness and overhangs has been observed in electrodeposited films in which the roughened growth was related to the diffusion limitations imposed by the depleted ion concentration at the surface of the film.[80]

Deposition on spheres and flat substrates used reaction conditions as near to identical as possible. Consequently, similar growth mechanisms for film deposition are anticipated. This expectation is supported by the similarity in A_f values and also by the visual similarity of the deposited clusters. As was discussed in the analysis of flat silver films, the microstructure of the film is determined by its method of growth. XRD data confirms the similarity in microstructure between shells and flat films. The integrated peak ratios and Scherrer analysis of Figure 7.2 for 114 nm silver shells on 530 nm silica spheres reveals randomly oriented crystallite textures and average crystallite sizes of 35 nm which is comparable to those measured for flat films.

Figure 7.2: XRD spectra of silver coated on 530 nm silica spheres spheres with an average shell thickness of 114 nm. Integrated peak ratios resemble that of randomly textured standards. The mean crystallite diameter based on the FWHM of the (1,1,1) peak is 35 nm

Based on the visual inspection analysis and XRD it is reasonable to expect that the electrical transport behavior of silver shells (with thicknesses below 130 nm) is governed by the same factors of geometry and microstructure discussed for the CD films in earlier chapters.
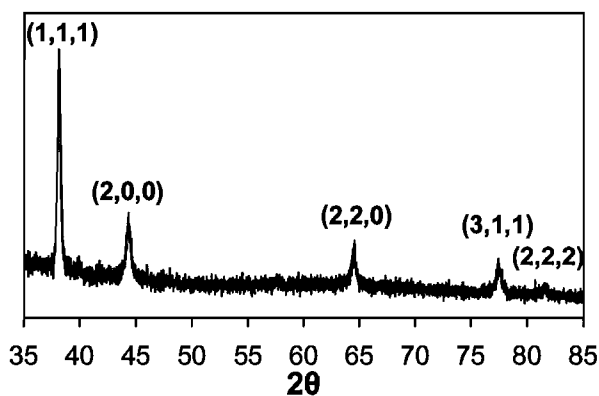
Aggregates of Silver Coated Spheres

We study the resistance of silver coated spheres by the formation of aggregates of coated spheres and then measuring R across the aggregate. Aggregates have been formed using two separate methods, sedimentation and pellet compression. Such an aggregate of metal coated spheres is expected to conduct so long as the conducting shells are sufficiently contiguous around the entire sphere and in electrical contact with neighboring shells. For the SC spheres the shells studied are sufficiently contiguous that as aggregates, low R values, on the order of 1 Ω, are measured. As with the CD films, the average thickness of SC shells is typically much greater than λ_{Ag} and A_f values are greater than 80%. By contrast, spheres coated using the TC method have average thicknesses below 50 nm and A_f values of $\approx$65%. Very thin CD films with the same characteristics as TC spheres were not measurably conducting, yet aggregates of TC shells demonstrate measurable conduction.

As with CD films, TC and SC shells are granular and incomplete to varying degrees. The network geometry of the silver therefore introduces additional surface area for electron scattering events and similar low quality of contact between crystallite grains is anticipated within the microstructure. However, modeling of the electrical influence of the geometry and microstructure on silver shells is not possible at this point. Data for the determination of g values for individual spheres and aggregates are not yet available. The ramification of this is that R data collected for aggregates of spheres cannot be converted into ρ values for comparison to bulk silver or other metal geometries. The primary comparisons which can be drawn are limited to quality and order of magnitude.

The measurement of R for a single silver coated sphere offers the most direct comparison of the silver as shells to the CD films. The mechanics of such a measurement are difficult and the attachment of electrodes to a curved surface with a diameter less than 1 μm presents a challenge in itself. Consequently such measurements have not yet been completed. The implications of a four point probe arrangement on a sphere also provide an interesting question of experimental design. The conduction pathways around a spherical surface present a random resistor network which has no limiting edge. Therefore the interpretation of resistance data may require an alternate assessment. These challenges have not been addressed at the present time.

Aggregates of spheres offer an attractive system because they present a 3-D macroscale material large enough to accommodate electrical contacts. In interpreting

the electrical behavior of aggregates, however, the microstructure within the shells must still be considered. For CD films, the grain boundary contacts within the films were previously compared to those of n-Ag. The high energy of the grain boundaries in n-Ag manifests dramatically in the low-temperature resistance of the materials and was related to the transmission coefficient of the crystallite grain boundaries in CD films as discussed in Chapter 4.

Aggregates of spheres coated by the same deposition reaction will thus also have a similar quality of crystalline grain contacts within a single silver shell. Aggregates of coated spheres additionally have a packing density between the crystallites of adjacent shells. Pellets of coated spheres also resemble the n-Ag pellets which are aggregates of silver nanoparticles.[51] In place of nanoparticles of metal compressed into pellets, we begin with a shell of metal. The contact between silver crystallites of different shells is therefore anticipated to be similar to the density of packing in n-Ag pellets.[51] It follows that the contacts between the silver of separate shells introduce additional grain boundaries whose transmission coefficient can be dramatically influenced by pressure. It also follows that sedimented aggregates of coated spheres will have a lower packing density than those shells that are subjected to pressure.

Resistance Data for Aggregates

Initial measurements of R for sedimented spheres were taken using evaporated gold as electrodes. A fine channel no more than 0.1 mm wide was cut in an evaporated gold film and a drop of coated spheres in solution was allowed to dry over the gap between the electrodes. Up to 5 drops were added allowing each one to dry before additional drops were added. R measured across an aggregate of spheres with ~100 nm thick shells was ~0.8 Ω. The method was unreliable, however, in that sometimes after many additions, R remained too great to be measured. It was not clearly established whether this was due to a lack of spheres in the aggregate or a lack of contact between the spheres themselves.

A more reliable method was developed by building a reusable module in which the spheres would be sedimented onto an insulating surface sandwiched between two electrodes as shown in Figure 7.3. This module requires that spheres be added in solution form and dried onto the insulating surface similar to the sedimentation on the flat gold electrodes. For spheres with average thicknesses between 110-125 nm, after one or two sedimentation steps, R is measurable and less than 100 Ω. Additional
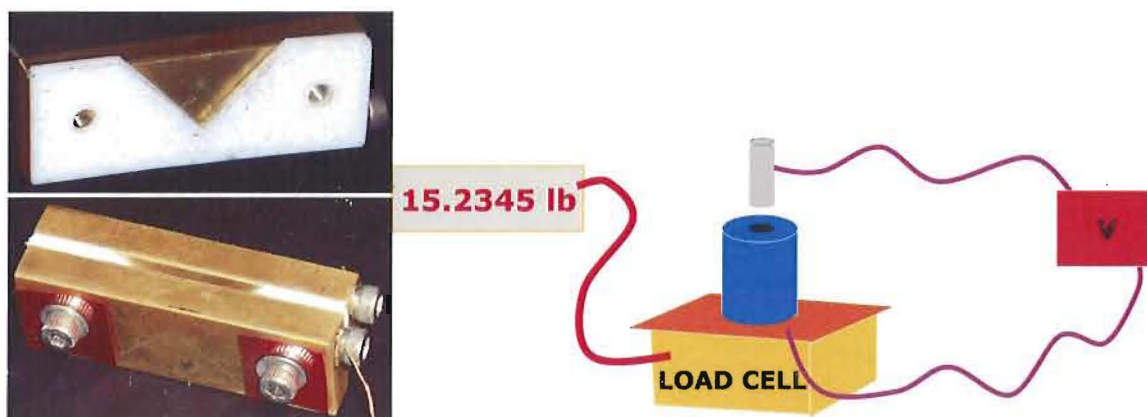
Figure 7.3: (Left) The module used to measure the resistance of sedimented aggregates of spheres both as deposited and during annealing. The cutaway shows the module opened up to expose the 2 mm wide "v" shaped surface on which the spheres collect. The brass walls act as the electrical contacts. (Right) Diagram of the voltametric pellet press. Dry silvered spheres are placed in the barrel and force is applied downward using the upper rod which also serves as one electrode. The lower rod (not shown) is in contact with the Cu plate below the barrel which provides the second electrode.

sedimentation steps result in a continued decrease in R until additional deposition yields no further change. Aggregates produced in the sedimentation module yielded consistent and reproducible minimum R values which averaged 3.2 Ω. For comparison, the short circuit value to the module resistance is 0.3 Ω. Thus the resistance of aggregates in the module is an order of magnitude greater than that measured on the gold electrodes. The difference can be attributed to the greater number of spheres required to bridge the 2 mm gap between the module electrodes indicating that the additional contact points between the shells increase the aggregate resistance.

Resistance and Pressure

Data obtained using a voltametric pellet press demonstrates the influence of improved contact between the spheres. When the contact between shells is tenuous, then the application of mild pressure will decrease R by improving the inter-shell contact. The voltametric pellet press (VPP), built in lab and shown in Figure 7.3, is used both for the formation of the pellets and the measurement of R. As with the module, a two contact method is used for resistance measurement. Aggregates are pressed with a known force while measuring resistivity across the pellet. The press uses an insulating barrel with 1/8 cm^2 diameter to contain the spheres which are pressed by two metal
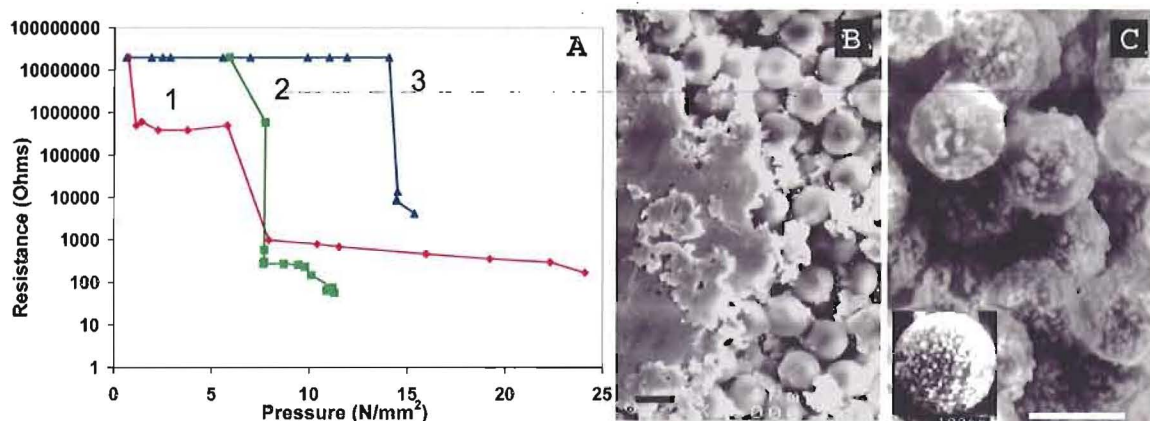
Figure 7.4: (A) Data for the onset pressure of pellets 1 (red diamonds), 2 (blue triangles), and 3 (green squares) are shown, also including the stable resistance reached with additional pressure. Lines connecting the points are visual aids. SEM micrographs show (B) the silver displaced by the bottom electrode of pellet 3 and (C) the intact nature of the spheres within pellet 2 after pressure testing. Inset shows a typical sphere from the batch used in pellets 2 and 3 before pressure testing.

rods that also act as electrodes with the lower electrode in contact with a copper sheet for easy connection to the meter. The resulting cylindrical-wafer pellets are 3.175 mm in diameter and typically less than 1.5 mm high. The force applied is measured using a load cell manufactured by Transducer Techniques. For these aggregates the coated spheres were first dried and then placed as powder into the barrel before the placement of the top pin which also functions as an electrode. Crush testing of 260 nm uncoated silica spheres gives pressure limits of about 45 N/mm^2 for 1 μm and 22 N/mm^2.

Measurement of R vs applied pressure is recorded by slowly increasing the pressure on the pins until a change in R occurs. The moment R began to drop, constant force was maintained until R stabilized and the value was recorded. The resistance of 530 nm spheres coated with 103 nm shells was $\sim$5 Ω with the application of a low pressure of only 0.17 N/mm^2. This corresponds well to the data collected for sedimented spheres in the module.

Micron sized spheres coated with less than 50 nm of silver have much higher R values (near 100 Ω) and provided a dramatic demonstration of the impact of improved contact between shells on R. As shown in Figure 7.4, the initial application of force was accompanied by a sudden drop in R at an onset pressure which varies by pellet. The onset pressure corresponds to the initial force that is sufficient to place the electrodes in contact with the topmost shells of the pellet. The high R values obtained after

the onset pressure is reached are similar to R values for a single sedimentation layer of 100 nm thick shells in the module. Here it is likely that the pins have made sufficient contact with only a portion of the shells and consequently R measured does not yet represent the pellet as a whole. This is only reasonable considering that some adjustment of the spheres is required for the formation of the pellet itself. These adjustments of spheres may also account for the variation in the onset pressure itself. Continued application of pressure ensures more complete contact between the shells and so reveals the influence of the thinner silver shells on the resistance of the pellets in Figure 7.4.

The resistance for pellet 1 levels out at a value of ~200 Ω, which is two orders of magnitude higher than results measured for 120 nm shells. SEM images of pellets 2 and 3 after the application of pressure reveal the changes that have occurred in the shells themselves, (Figure 7.4B and C.) Deformation has occurred at the contact with the electrode and some parts of the pellet interior, while most shells in the interior of the pellets remain intact, indicating that the R measured can be attributed to the network of individual shells and not to a complete deformation of silver packed between the spheres. However the significant deformation that does take place requires that conclusion be assessed with care. The possibility exists that the electrical behavior measured cannot be rightly attributed to an aggregate of shells rather than simply a composite aggregate of silica spheres and silver nanoparticles. It is also not conclusive that the electrical properties of shells in aggregates will be notably different from the simple composite system of spheres and metal nanoparticles.

The A_f for 50 nm shells is $\approx$65%. CD films with comparable A_f did not have measurable R values. Consequently, R values for aggregates of spheres coated with less than 50 nm of silver were not predictable based on R data obtained for flat CD films. Even so, the results are not inconsistent with that data. The A_f of these spheres (65%) is lower than lowest of the silver films (75%) measured and therefore it follows that their measured R values are significantly greater than those for CD films.

Pressure data for SC films of 100 nm shell thickness and greater also demonstrate the improved contact between spheres attained in the pellet press. The R values decrease with pressure beyond the onset pressure, though without the multiple orders of magnitude shift in R observed for the thin TC shells. The overall aggregate R values near 0.4 Ω are consistent in magnitude with many thicker CD films, but lower than films of comparable filling fraction. As with the spheres in Figure 7.4, some deformation of the shells is observed after VPP testing, particularly near the

electrodes as shown in Figure 7.5C. The spheres in the middle of the pellet are generally found to retain their shells with limited regions of deformation. For both types of coatings tested, the 50 nm silver on 1 μm spheres and the 70 nm silver on 530 nm spheres, the measured R values were lower than those for equivalent CD films. While there are flaws in the comparison of 2 point contact measurements to the 4 point system used for CD films, the expected error would be in the reverse direction due to the inclusion of contact resistance in the measurements of sphere aggregates. We speculate that the pressure improves the contact of crystallites not only between shells, but also within the individual shells. Because we are comparing resistance and not resistivity values, the impact of the 3-D network geometry of the aggregates has not been accounted for.

In addition to improving the contact between spheres, the VPP reveals a trend relationship between pressure and R and allows an investigation of the reversibility of the relationship. Cycling the application of force on pellet 3 demonstrates that the decrease in R is reversible to a large degree though with significant hysteresis (Figure 7.6 on the left.) By the third application of pressure, contact is attained with only a fraction of the pressure required for the first cycle. This is evidence that the pellet takes on a shape that it holds after the contact is

Figure 7.5: (A,B) Results for the effect of pressure on the resistance of aggregates of 530 nm silica spheres coated with ~70 nm shells of silver. SEM images showing (C) the loss of silver at an electrode contact area and (D) the partially damaged shells within a pellet after pressure has been applied.

removed. Cycling of the pressure between two specific values reveals similar behavior which is reversible in trend though the R values attained steadily decrease, suggesting that some irreversible changes are imposed by the addition of pressure. This type of pressure sensitive behavior may hold promise for electrically based sensors, such as for stress testing of materials.
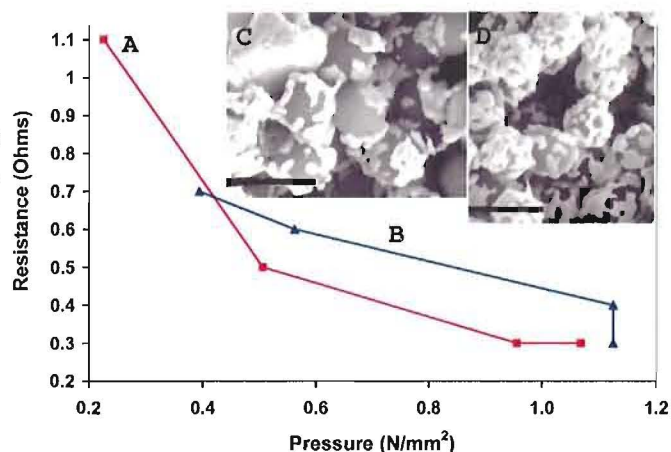
Figure 7.6: Plots showing (left) the reversibility with hysteresis of the change in R with pressure and (right) the result of cycling between two applied pressures on pellet 3.

Annealing, Resistance, and Temperature Dependence

Thin metal films are often annealed for the purpose of stabilizing the structure of the film. At elevated temperatures, yet well below the melting point of silver, microstructural changes are known to occur.[93,94] These changes include 1) the loss of microstructural defects and vacancies within crystallites, 2) recrystallization at grain boundaries, and 3) the growth of crystallites and/or the shifting of grain boundaries. With sufficiently high temperatures silver films will dewet the surface on which they are deposited. Dewetting is also referred to as agglomeration. The dewetting temperature is still well below the bulk melting point of silver, 1234 K, due to melting point depression for nanoscale metals.[95] Thin films were found in Chapter 5 to dewet the surface at ~400K. The adhesion of silver to silica is known to be poor[26] and the porous nature of the films also contribute to the ease of dewetting. In appearance the geometry of CD silver films resembles evaporated silver films during the dewetting stages.[88]

It is also well known that heat treatments impact the size and shape of metal nanostructures. For example, temperature treatments of 583 K are used as a method for growing metal nanocrystals in glasses,[18] the particle size of nanocrystal sols increases when refluxed in toluene (bp 384 K)[105] and low temperature annealing at only 303-329 K leads to island growth for 5 nm Ag films vapor deposited on mica.[110] Consequently, some rearrangement is expected during the annealing of CD silver films and shells.

Original shells
~71nm   **473 K**   **573 K**   **583 K**   **633 K**

Figure 7.7: Changes in shell morphology after sintering show dewetting at 583 K. Silica spheres are 530 nm originally coated with 71 nm average shell thickness. All sizing bars are 500 nm.
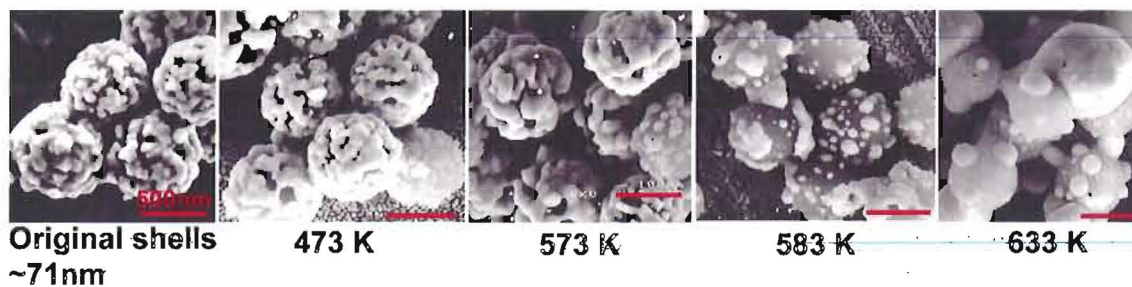
Spheres coated with silver were annealed after sedimentation on an aluminum base. The clusters of spheres with 71 nm average shell thickness show the first signs of dewetting at 473 K progressing to extensive beading of the silver at 583 K. Smoothing and dewetting are visible via SEM images as shown in Figure 7.7. Less visible changes, such as the loss of internal defects and vacancies, can be monitored via the resistance of the shells or films. Because annealing allows the system to reach a lower energy thermodynamic state, it is typically employed to stabilize a material for room temperature analysis. In the case of CD films annealing improved the contact between crystallite grains. This effect was observed as an increase in the α of the film corresponding to an increase in P. For nanoshell aggregates, annealing may also strengthen the electrical contact between shells by improving the contact between the grains that link neighboring shells.

Because the R value reflects multiple changes occurring within the metal, certain trends are typically seen during the annealing of thin films.[93,94,111,112] Previously discussed in the context of CD films (in Chapter 5) these trends are also applicable in the study of metal nanoshell aggregates. An initial increase in R with temperature corresponds to the increase in phonon vibrations within the metal. When R levels with temperature or even decreases, a loss of defects and vacancies within the crystallites and at grain boundaries counteracts the continued increase in phonon resistance. Finally, a sharp increase in R is seen when the film's geometry begins to change through the growth of voids until, eventually, dewetting begins. Continued heating sends R out of measurable range due to the formation of metal islands which are no longer interconnected. The changes in R due to loss of defects and altered geometry are irreversible.
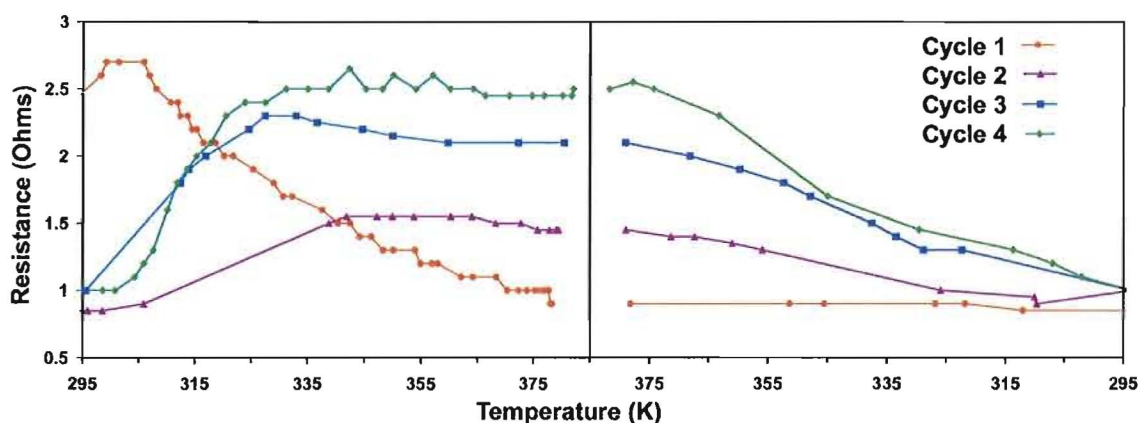
Figure 7.8: The dependence of R on temperature during four annealing cycles is shown for a single aggregate of silver coated spheres. Cycle 1 initiates an irreversible decrease in R, while subsequent cycles maintain the same R at 295 K, but a changing dependence of R on temperature.

The resistance of silver coated spheres was measured during annealing in the sedimentation module and the trends described above were observed. During the initial heating and cooling cycle, R decreases irreversibly up to ~473 K followed by a sharp and permanent increase in R at higher temperatures. SEM images reveal that the loss of conductivity coincided with dewetting of the silver from the spheres. Heating was accordingly limited to lower temperatures to avoid dewetting. As with thin films, the aggregate samples retained a lower R after annealing, indicating that irreversible changes in microstructure had taken place. In the case of CD films those changes were determined to be primarily related to the loss of defects. This loss of defects was also expected to be a cause of the decrease in R observed for silver shell aggregates.

Figure 7.8 shows the resistance of an aggregate cycled between 295 and 378 K. After the initial drop in R, the 2nd, 3rd, and 4th cycles all showed reversible increases in R with heating corresponding to phonon vibrations. In each cycle the leveling of the T vs R relationship is evidence that continued changes in microstructure and/or geometry occur above 320 K. Such continued change, however did not alter the value of R_{295K} for multiple cycles. Any additional loss of defects and improved connection between grain boundaries that are implied by the leveling of R at 320 K and greater for cycles II and III are expected to lower the minimum R at room temperature. Instead the data show an increase in α for each cycle with no change in R_{295K}. The numerical values of α in this case cannot be obtained directly from the data due

to the use of a two point probe measurement. In two point probe measurements, the contact resistance and its temperature dependence is implicitly included in the measured data. Nonetheless, the trend of increasing dependence of R on T is very clear. The source of the shift may be related to an increase in contact between the crystallites on adjacent spheres as has been shown for CD films, but has negligible impact on the overall resistance due to the macroscopic nature of the entire resistance network.

SEM micrographs confirm that the changes induced by annealing did not include dewetting of the spheres, though some smoothing of silver clusters is visible. It is also valuable to note that resistive heating is sufficient to dewet spheres when currents greater than 400 mA are sourced. Currents greater than 50 mA may also heat the silver sufficiently to cause irreversible changes in measured R.

The resistance of our silver shells of $\sim$100 nm is comparable in magnitude to CD silver films. As with a CD film, the aggregates of shells offer many pathways for electron transport if sufficient contact between the shells is maintained. Further analysis of silver shell aggregates is necessary to confirm conclusively that CD film properties are applicable to the shell aggregates. The preliminary data presented here support that the geometry and microstructure of CD films and shells are comparable. However, additional properties have been observed which are unique to the coated sphere aggregates and also merit further study. These include the pressure sensitivity of spheres with very thin shells and the behavior of R during annealing which varies with multiple heating cycles.

Summary for Silver Shells

Silver shells coated on silica cores were produced with predetermined average shell thicknesses using a stoichiometrically controlled reduction. The resulting materials exhibit optical tunability based on core size and shell thickness. The silver shells are rough and granular and appear very similar to silver deposited on planar substrates by the same reduction method. Similar grain sizes and orientation between shells and planar films are also observed using X-ray diffraction. Because of these similarities we anticipate that the completed electrical studies for films will be comparable to future results for shells. Preliminary data for shells obtained using two point probe methods cannot be quantitatively compared compared to four point data for films. We also note that nanoscale spherical shells lend themselves to potential applications

which films are not suited for such as suspension in colloidal solutions for molecular detection and as pellets which have an electrical sensitivity to pressure.

CHAPTER VIII

CONTAMINATION STUDIES

Metals fabricated with sub-micron dimensions are known to be sensitive to their chemical environment. Therefore any study of the properties of such metals must take care to ensure that the results obtained are in fact due to the metal and not some form of contamination in the system. As a case in point, one recent study which initially attributed the gas sensing ability of silver nanowires to the silver metal, with further diligence discovered that it was in fact silver (I) oxide that led to the electrical sensitivity to ammonia.[113,114] This chapter delineates the studies aimed at investigating potential contamination for both chemically deposited (CD) films and for silver coated on silica nanospheres.

Residual Organic Compounds

One possible contamination source for both CD silver films and for silver coated nanospheres is the presence of organic starting materials either on the surface or incorporated into the pores of the silver film. In these cases, the primary safeguard against contamination is a thorough cleaning procedure. The efficacy of the cleaning procedures used in these experiments was verified using energy dispersive spectroscopy (EDS.)

The electron beam used to obtain SEM images leads to the excitation of X-rays that are characteristic of the atomic orbitals for the elements present. The EDS detection system work in tandem with the SEM in order to detect and interpret the X-ray energies emitted and thus determine the atomic content of the sample surface. One advantage of the EDS system is that multiple locations may be selected and sampled quickly for overall composition.

CD silver films and shells were analyzed for the incorporation of organics from the deposition reaction by comparison of their spectra to those taken for a pure silver standard. EDS data for a 99.99% pure silver standard obtained from Kurt J. Lesker

(atomic %)	C K	O K	Al K	Si K	Zn L	Ag L
Ag standard	7.58	-	-	-	-	92.42
CD film	7.88	6.21	0.92	13.09	0.54	710.6
SC shells	5.47	54.91	-	17.95	-	21.67

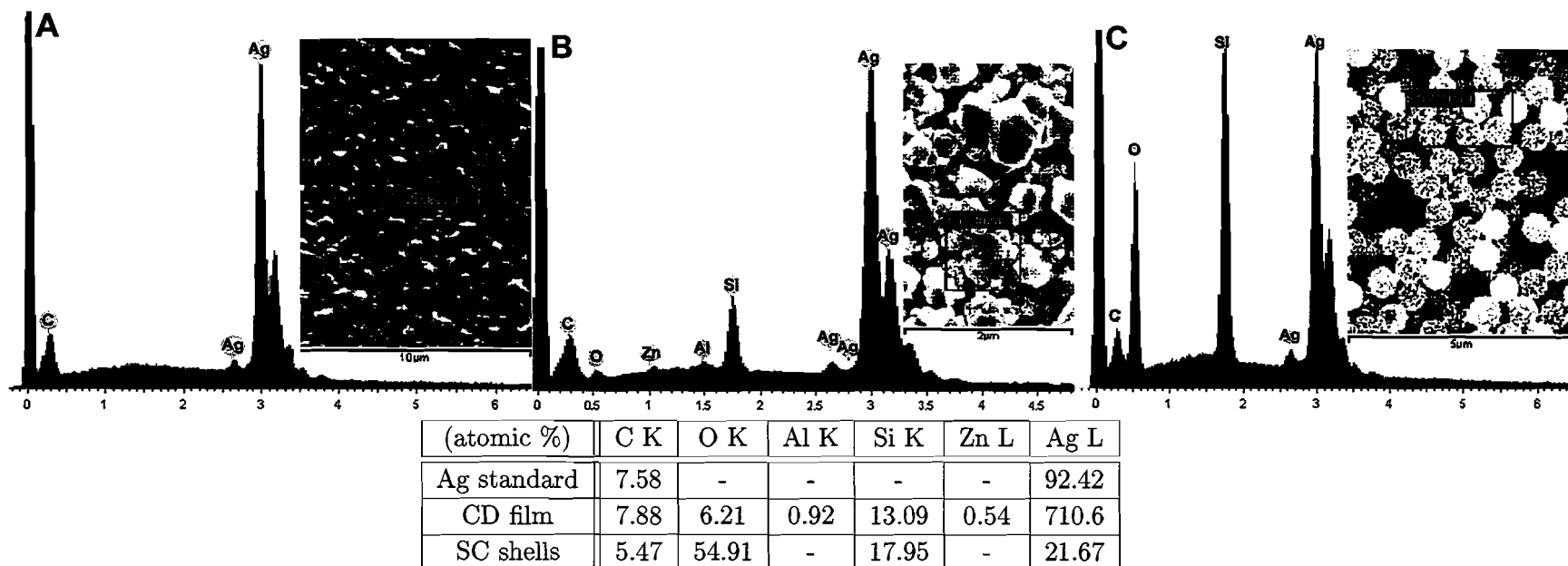Figure 8.1: Comparison of the energy dispersive spectra taken for (A) a 99.99% silver standard to the spectra of (B) a CD silver film and (C) silver coated spheres, indicate the presence of ambient carbon levels with no other measurable contamination. Al and Zn are elements present in the silica substrates of the CD films. K and L designate the orbital energy levels that are used in the atomic % analysis for each element.

Company compared to representative data for CD films and coated spheres is shown in Figure 8.1. The standard was freshly cleaned and etched with concentrated HCl. Ambient carbon is known to be present in the air of the building and comparison of the carbon levels reveals that they are comparable for all samples. The $\sim$ 7 atomic % carbon detected on all samples therefore does not indicate residual reactant materials, rather we take this value to be ambient carbon which attaches to silver surfaces.

The washing process for films and coated spheres thus proves to be effective for the removal of reactant material. For films this involves repeated rinsing with ultrapure water and ethanol, while for spheres, repeated centrifugation, removal of supernatant and redispersion in clean solvent is used.

EDS of the CD films confirms the presence of silver along with elements of the glass substrate, primarily silicon and oxygen with trace amounts of aluminum and zinc. The substrate spheres are confirmed to be pure silica.

Silver Oxide

Silver oxide formation on the surface of the films is another possible source of contamination for silver studied in an oxygen containing atmosphere. Due to the presence of oxygen in the silica substrates and the limited sensitivity of the method, EDS cannot quantitatively determine the existence of silver oxide. In order to measure the oxide layer thicknesses for silver coatings stored in ambient environment, vacuum deposited silver on Piranha cleaned silicon substrates was analyzed using electron probe microanalysis (EPMA). This silver oxide data for VD silver is applied to both CD silver films and SC silver spheres once they have been exposed to oxygen atmosphere.

EPMA uses a focused high energy beam of electrons at controlled energies to ionize material and induce characteristic X-rays of its elemental orbital structures detected using wavelength dispersive spectrometry (WDS). This method uses similar principles to the EDS in detecting specific elements, but has greater detection sensitivity. The EPMA-WDS system measures high purity standards with every unknown for accuracy in elemental characterization. Only one element is measured at a time by limiting the range of wavelengths detected such that the precision is improved over EDS.

Correction procedures for detection of multiple elements were applied to allow the determination of elemental and molecular thicknesses from the data. The results showed that if the oxygen detected is in the form of Ag_2O, then a thin layer of 5 nm

$Ag_2O \pm 3$ nm can be expected on the surfaces of all silver faces exposed to oxygen atmosphere. We note that EPMA is not able to chemically distinguish between adsorbed oxygen and silver oxide. However, the amount of oxygen detected was much higher than would be expected for only an adsorbed layer. For the purposes of quantifying the analysis we have assumed that all of the oxygen was present as silver oxide, though it is likely that oxygen was present in both forms. We assume the presence of Ag_2O because it is the most thermodynamically stable oxide of silver. Variations in exposure times from 5 hours to 4 days did not alter the thickness of the oxide layer detected. The presence of Ag_2O must be considered then when evaluating the properties of the CD silver films and SC silver shells in open air. This layer is only expected to be at the surfaces because diffusion of oxygen into the film is negligible at ambient temperatures.[115]

High angle XRD studies show no evidence that silver oxides were present in a crystalline form. The largest peaks of AgO and Ag_2O are not present in the spectra of Figure 8.2. The XRD spectra for silver shells have XRD spectra comparable to those of CD films and are not shown.[91,116] It may be reasonably concluded that any silver oxides present were primarily amorphous or of negligible quantity.

Whether or not Ag_2O was present on the surface is only of concern to the extent that it determines the properties of the overall film or shell. As a semiconducting material, Ag_2O has a notably higher resistivity than pure silver.[117,118] The resistivity values measured for CD films, while elevated, do not approach the values for silver oxides.

The temperature coefficient of resistance gives further indication that the properties of silver oxide were not being measured in the study of CD films. The value of α for silver (I) oxide, ~ 0.02, is much greater that of bulk silver, 0.004.[118] The presence of Ag_2O at the grain boundaries would be expected to increase the α value if it were significant to the temperature dependence of R in CD films. On the contrary, the α values measured for CD films are consistently lower than for bulk silver. Moreover, the measured values of α show excellent agreement with data connecting the presence of significant defects at grain boundaries with depressed α values for silver, as presented in Chapter 5.

The lack of influence of silver oxide on the data presented for CD films can ultimately be explained by their growth mechanism and their scale. During the deposition of CD films the grains of pure silver grow together while still in solution. The grains grow into reasonably good contact as indicated by their equivalence to a
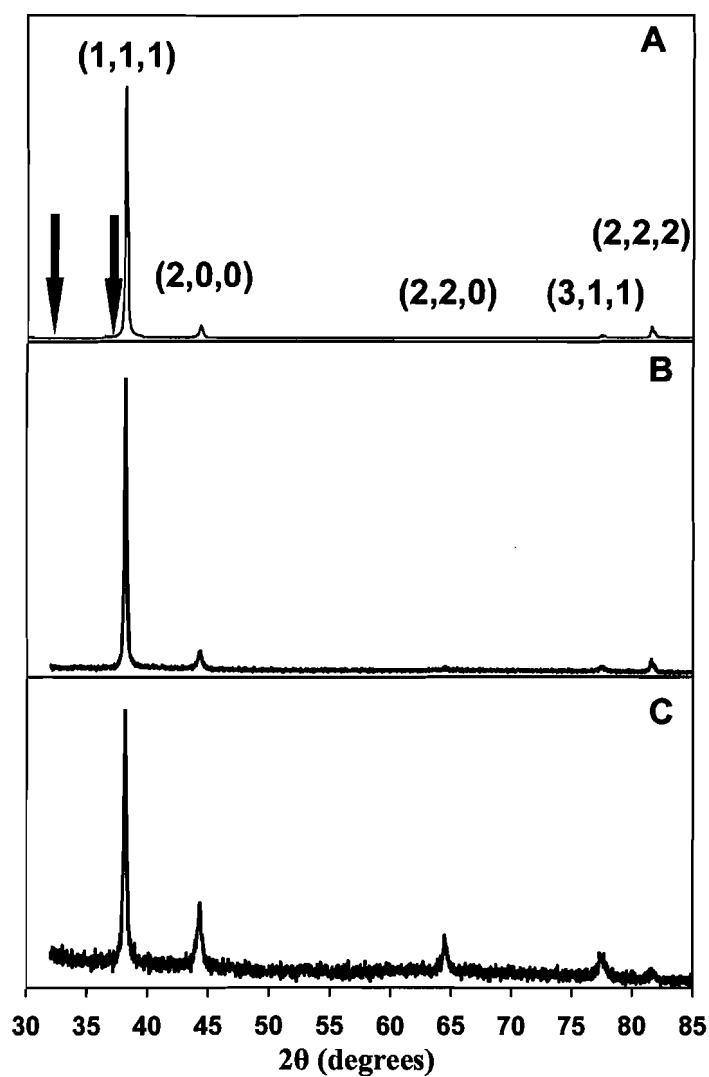
Figure 8.2: XRD spectra demonstrate the presence of crystalline silver in films vacuum deposited on (A) silicon (∼77 nm) and (B) silica (∼60 nm.) (C) A chemically deposited film (t_{eff} ∼140 nm.) The red arrows indicate locations for the absent crystalline silver oxide peaks.

95% or greater packing density of nanocrystals (see Chapter 5). Because the same method is used in the growth of silver shells we expect that the same arguments apply to those materials as well. The primary difference in treatment of shells and films is that shells have less atmospheric exposure such that the time available for oxide growth before electrical measurements are taken is even less than for planar films. As further methods are developed for the measurement of the resistivity of spherical shells this expectation may be tested for the specific case of shells.

The influence of silver oxide on nanowires used for sensing occurred for wires with diameters less than 300 nm because narrower wires were more likely to exhibit quantum point contacts.[113] The presence of a quantum point contact in a wire limits the behavior of the wire as a whole because no other electrical pathways are available. This is not the case for CD films and shells even though they may also include quantum point contacts. Alternate pathways connected by larger silver grains are always available in films of sufficient thickness and electron transport will favor these less inhibits routes.

In conclusion, small quantities of carbon and Ag_2O are found to be present on all silver surfaces that have been exposed to open air. EDS data shows that the carbon present is equivalent to what deposits on a 99.99% pure silver standard and therefore is not due to residual reactant material on the metal. EMPA data finds a thin layer of Ag_2O on the surface of VD silver films suggesting that silver CD films and shells after exposure to ambient air will also form Ag_2O. However, XRD, the method of film growth, and analysis of the transport properties of the films indicate that neither of these contamination sources is determining the properties of the CD films under study. A network of pure silver connections is the most probable source of the reported film properties. Comparable results for spheres are expected.

CHAPTER IX

CONCLUSION AND FUTURE RESEARCH DIRECTIONS

Summary and Conclusions

The primary conclusion of this research is that a detailed characterization of scale, geometry, and microstructure is necessary in order to understand and predict the electrical properties of nanoscale and nanostructured metals. For the specific case of CD films we find that each of these factors contributes to the electron transport behavior within the film. Additionally, the relative contributions of scale, geometry, and microstructure are distinct from those present in VD films or n-metals. For example, even though the geometry of CD films may resemble a scaled up agglomerated film, the microcrystalline properties of the CD film have a greater contribution to the film's resistance.

The method used to produce metal films largely determines the characteristics of scale, geometry, and microstructure. For example, it is not possible to control the grain size independently of the thickness for vacuum deposition.[67] At the opposite extreme, n-metal films allow fine control of crystallite size, but not the orientation of the crystals. CD films offer their own unique combination of a network structure with randomly oriented grains that are smaller than the average length between scattering surfaces.

Models of the impact of scale, geometry, and microstructure are an important tool in the development of optimized technologies. Microstructural control of the film properties by the choice of deposition method allows the production of metal films with the most desirable transport properties for a given application. Current resistivity models for thin metal films build on the F-S model for films with uniform thickness, modified to account for surface roughness. We conclude that the limitation of a uniform thickness is geometric in nature and that, given an appropriate description of geometry, the F-S and V-H models may be applied to nano- or mesoscale metal structures which do not necessarily meet this requirement. The case in point is the

semicontinuous CD films presented here. The geometric parameter used in previous film studies has been the thickness, t. We have proposed the use of a value g, which represents the critical length scales to electron transport within the specific system. Toward this more universal model we present the parameter mf/e to describe CD film geometry. Values of g calculated for CD films correlate in a direct proportion to mf/e. The value of mf/e thus relates the resistivity and geometry of CD films in the same way that thickness does for VD films. While the exact relationship of mf/e to the physical geometry of CD films is not clearly understood, we have suggested that the ratio of e/f may approximate the 3-D porosity of the film.

XRD data demonstrate that the mean crystallite grain sizes are on the order of λ_{Ag} and that the grains are randomly oriented. These characteristics are known to increase ρ and support the conclusion that grain boundary influences are significant to ρ for CD films. Moderate annealing of CD films leads to a decrease in R without any significant changes in the geometry, grain size, or grain textures. These results demonstrate that a combination of defects at grain boundaries and within the crystalline domains also contribute to the elevated CD film resistance as compared to VD films.

The temperature dependence of electron transport in CD films is found to be dominated by the influence of crystallite grain boundaries. The α values for CD films are lower than can be explained by size effects alone. The α values do fit the V-H concept that the electron density is reduced by grain boundaries. Low temperature studies of α give results comparable to those for n-Ag materials. The smaller dependence of α on temperature is also explained by the decrease in n_{eff} caused by the potential barrier to electron transmission through each grain boundary.

The application of the combined F-S and V-H models to CD films using $\frac{mf}{e}\frac{1}{Ad}$ in place of thickness is shown to result in quantitatively reasonable values for the specularity, p, grain boundary transmission coefficient, P and the resistivity within the crystalline domains ρ_o. By contrast, results using average thickness values alone result in unrealistic values for both ρ_o and p. These results confirm that with the appropriate value of g, the F-S and V-H models are able to account for the combined influences of scale, geometry and microstructure in a non-uniform film.

The study of silver films with network geometry is also extended to shells deposited on silica spheres with diameters less than one micron. The SC synthesis developed in the context of this research, results in a pure inorganic two component silver and silica material. Shells with average thicknesses ranging from 80 to 170 nm have been deposited by a single step procedure. The optical characterization of these shells

found that their plasmon resonance was tunable by variations in core size and shell thickness, despite the semicontinuous geometry of the silver. This synthesis method was also used in the deposition of CD films.

Electronic studies of silver coated spheres were approached using aggregates of the coated spheres produced either by sedimentation out of solution or using a pellet press. Pressure in the pellet press was observed to damage the shells both near electrode surfaces and a sometimes within the pellet interior. Consequently the overall material studied in the pellet press may be better described as a composite aggregate of silver nanoparticles and silica spheres rather than of coherent silver shells. The measured resistance of the pellets were found to be pressure dependent with minimum values less than 10 Ω. Sedimented aggregates did not experience the same loss of shell coherence. The measured resistance values were also on the order of Ohms. These results are on the same order of magnitude for CD films, however the comparison is limited by the use of 2 point resistance measurement techniques on aggregates and 4 point measurements for films. The analysis of aggregate resistance data as a whole was also limited by the use of two point resistance measurements. The development of a 4 point probe system for aggregates is an important step in the continuance of studies of the electrical properties of spheres.

Future Directions

Many avenues of future research remain to be explored regarding chemically deposited metals following the results presented here. Focusing first on the immediate steps that may be approached for the CD films, further characterization of g is warranted. Cross sectional studies of CD films to quantify their vertical porosity would reveal whether the measured parameter e/f, derived from the filling fraction, is in fact an estimate of the overall porosity of the films. This type of data could be gathered through the use of focused ion beam (FIB) to slice the films and imaging the cross section using electron micrography. A layer of deposited metal such as platinum has been reported to sufficiently protect the surface structure of rough metal films during FIB cutting.[80]

The measurability of g values for other variously structured metals also merits investigation. For example, in addition to the filling fraction, the film surface area might be also related to g. The relationship between the volume and surface area of a structure may provide another way to measure the relevant scale for surface scattering in the metal. Investigation of the exposed surface area and its relationship

to resistivity could then assist in further understanding the physical description and measurability of g. Such a relationship would be especially valuable in materials that do not have a measurable filling fraction.

Metal films are currently used in many technological applications. It is possible that the electrical properties of many of the films may not be optimized for their specific use. The ability to tailor the material characteristics can be further developed both through the choice of deposition method and by the variation of parameters within the method. Toward the end of microstructural design, we conclude that additional research in methods for the deposition of metals as well as other conducting materials should be pursued. In this way their characteristic length scales, geometry and microstructure may be varied in new combinations.

Published work presenting metal films produced by other electroless methods are known produce a different geometry than the CD method, yet that geometry has not been characterized in terms of geometric parameters other than t.[15,119] Application of the concept of g to these films will allow their electrical properties to be better understood. Additional control of deposited microstructure may also be possible within chemical deposition methods, for example by the use of an epitaxially compatible substrate such as silicon.

The relationship of the quality of electrical contact between silver crystallites and the temperature dependence of electron transport is an intriguing one. This relationship may allow the experimental quantification of P. The lack of variation in α at temperatures below 140 K for poorly connected grains has been attributed to the depressed thermal energy of the electrons such that they are no longer able to pass the high activation barrier of the grain boundaries. Based on this assumption, it should be possible to determine the actual value of the activation energy for the grain boundaries of a given film or n-metal. This activation energy may further be related to the value of the P used in the V-H model. The ideal material to use in such a study would be a n-metal with single crystalline grain sizes equal to λ such that $\rho = \rho_o P$. In this ideal case the elevation of resistivity caused by grain boundaries is dependent exclusively on the value of P. Materials which approximate this condition can be produced by n-Ag methods.[50,51]

In the study of silver coated spheres the measurement of the resistance of a single sphere is a critical experiment for the comparison of flat CD films to the spherical SC shells. Such a measurement done using 4 point probe techniques could allow the application of the F-S and V-H models to a single sphere. This measurement would

also allow the observance of any variances between the resistivity of single spheres as compared to aggregates and to CD films.

The use of pellets both in n-Ag[51] and of silver coated spheres has led to some interesting observations on the relationship between pressure and resistivity. For n-Ag this relationship has been reported to be due to the variations in contact between metal grains caused by the pressure. For n-Ag this is discussed as the packing density.[51] For sparsely coated silver on spheres we report that the change in resistance with pressure shows significant reversibility. These results suggests that the addition of the dielectric material to the composite limits the electrical transport pathways in such a way that they may be broken and reformed with small changes in pressure. Composite aggregate materials of silver or other materials with dielectric spheres thus present an avenue for studies in the electrical sensing of pressure.

The limited investigation into the storage methods which discourage the aggregation of silver coated spheres suggest further investigations involving the relationship of the shells to liquid media. In addition to long term storage, solvents which limit aggregation are needed for the advancement of crystallization techniques. Most methods for the production of ordered crystalline arrays of silica spheres rely on capillary forces. These methods require a similarity in the density of the spheres to the solvent.[120] Silver shells are significantly more dense such that these methods result in disordered aggregates or at best, single layers with short range order. The use of higher density polymer solutions such as the PVA and PVP used in aggregation studies, may allow crystallization to occur using methods similar to those with plain silica spheres. One difficulty with this approach is that the long chain polymers may incorporate into the the crystal. Thus new methods for cleaning may be necessary in order to remove the polymer organic material from the ordered structure.

Each of the above future directions continues our focus on microstructural control of material properties. The research presented has sought to deepen the scientific understanding of the influence of scale, geometry, and microstructure on the electrical properties of rough, semicontinuous, chemically deposited silver. Moving forward, we anticipate that this understanding will contribute to functional material design and assist in the optimization of electronic technologies.

APPENDIX A

GOLD CORE-SHELL MATERIALS

Background

In the field of core-shell materials analysis and engineering, gold core-shell structures have received more study than those of silver in part because the shells produced by gold reduction are typically of a smoother more uniform nature. This lends them more easily to optics models for plasmon response based on spherical shells. Understanding these materials is of current interest for their use in biomedical applications, sensing, and photonic band gap materials.[20,22,98,121] In collaboration with the lab group of Jim Hutchison, we have produced a new method for the synthesis of gold shells on silica nanospheres and also for the production of a stable silver on gold core-shell nanoparticle colloid.

The SC method reported in Chapter 6 for silver on silica requires no intermediate seeding or use of organic ligands. An equivalent single step method has not been reported for gold deposition. Instead organic ligands are employed to decorate the silica with metal nanoparticles before reduction of a complete metal shell. The organic ligands used in previously reported methods rely on the affinity of the exposed silica surface to a silane group and the affinity of an amine, or mercapto group for gold or silver. Two very commonly used functional groups are 3-aminopropyltrimethoxysilane, APTMS, and 3-mercaptopropyltrimethoxysilane, MPTMS. These ligands have a sensitive chemistry which is prone to polymerize and result in non-uniform coatings which can detach from the silica spheres.[122–124] We speculate that these limitations hindered our efforts to reproduce a previously published method for depositing silver on silica shells.[24] Foster and coworkers have independently developed a chemical tether for attaching gold nanoparticles to silica substrates which is much more robust than the above ligands.[108] This nanoparticle linkage provides a high density of gold nanoparticles at the sphere surface onto which additional metal can be reduced from
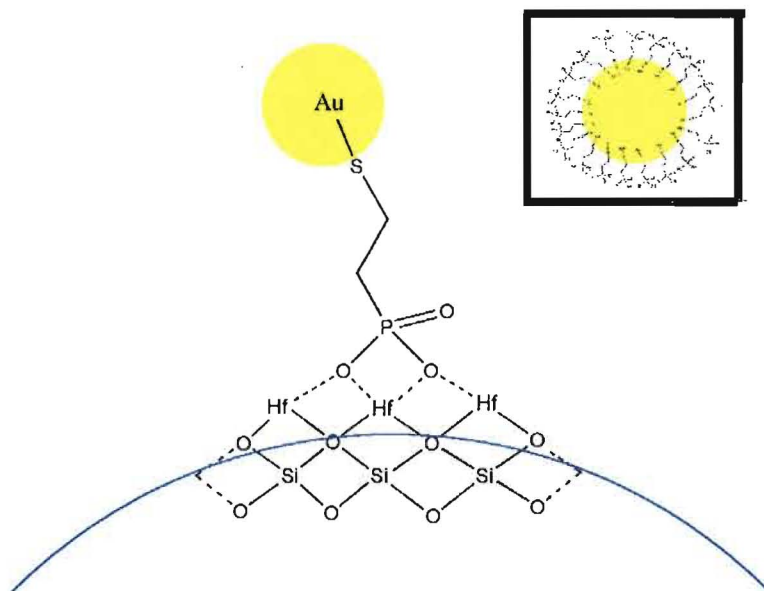
Figure A.1: One possible scheme for the Hf^{4+} mediated attachment is shown. The Hf^{4+} is expected to complex with the oxygen in the silica network and the oxygen on the phosphonate group. This representation is not to scale. Upper right : representation of a 2 nm FGNP cross-section demonstrating the complete coating of phosphonate ligand.

chloroauric acid similar to previously published techniques.[40] This method of seeding provides a more reliable route of synthesis. It limits the detachment of the gold nanoparticles and thus prevents the growth of gold nanoparticles in the reaction solution. Consequently shell growth is optimized.

This attachment system uses functionalized gold nanoparticles (FGNP) where the functionalization is a monolayer of mercaptoethylphosphonic acid. This phosphonate ligand then complexes with Hf^{4+}ions which are adsorbed onto a silica surface, in this case a silica sphere. Thus the phosphonate group acts as a tether forming a stable gold to silica linkage. Though the precise chemistry of the attachment between the Hf^{4+} and the phosphonate group has not been investigated, one possibility is shown in Figure A.1. This system of decoration using the FGNP has proved to be more stable and reproducible in our experiments than APTMS ligands. Unlike the -TMS ligands, the phosphonate ligand will not polymerize. The Hf^{4+} to phosphonate interaction provides a robust silica attachment and the thiol group has a strong affinity for gold attachment.[108] Consequently this new ligand system eliminates the problem of gold nanoparticles detaching and providing nucleation sites for the growth of metal

nanoparticles during the reduction of compete shells. In general, the use of a seeded decoration system for producing core-shell materials has resulted in smoother shell morphologies. It has been established within this document that the geometry and the structure of thin metal layers is highly significant to the electrical properties of the films and has also been shown to be significant to the optical properties of the core-shell material.[87] A reliable seeding method, therefore is a critical tool for the control of microstructure material properties.

Experimental

The seeding procedure was demonstrated both on glass slides and on spheres. The details of the process are presented as follows. Glass slides were cleaned by soaking in piranha solution for 30 minutes or more and by ultraviolet exposure. The slides were soaked in a 5 mM dry methanol solution of Hf^{4+} ions from the salt Hafnium (IV) Chloride. The slides were left in the solution overnight to promote a high concentration of Hf^{4+} ions at the silica surface. The slides were then rinsed and soaked in a concentrated solution of $\sim$2 nm FGNP in water. The same process was used for the decoration of 260 nm silica spheres. Cleaning of the decorated spheres was accomplished by centrifugation and subsequent sonication to redisperse the pellet of decorated spheres.

The details of the procedure for reducing the complete gold shell onto decorated spheres are not presented here because they are readily available in the literature[40] Only those details of concentration and method which are specific to this deposition are reported. A pH neutral mixture was used with concentrations of 0.0019 M potassium carbonate and 0.65 mM chloroauric acid. The volume of the solution to be used was calculated to give a particular shell thickness. For a 30 nm shell of gold on 260 nm silica spheres, 0.1 mL of decorated sphere solution with 1.26×10^{11} spheres/mL was added to 15 mL of the $HAuCl_4$ and KCO_3 solution. While stirring, 20 μL of formaldehyde was added to begin the reduction. Heating in a water bath to 60 °C was usually required to begin gold reduction except in the case of very densely decorated spheres.
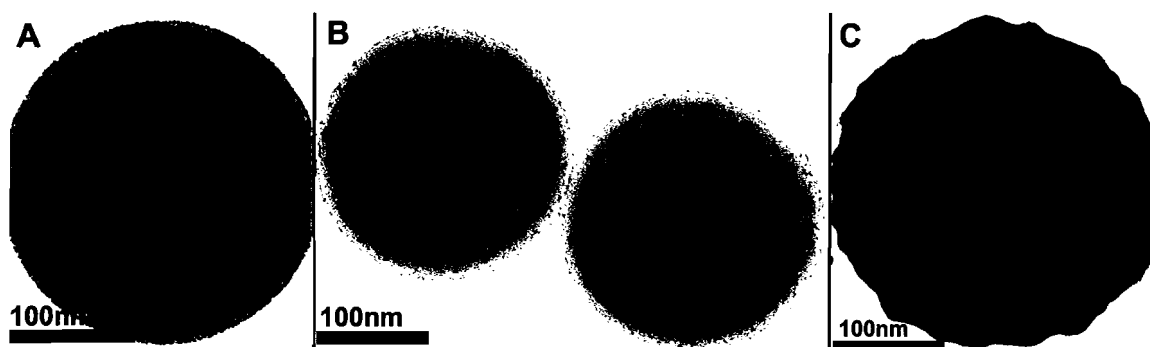
Figure 9.2: (A,B) High density coatings of ~2 nm gold seeds on silica spheres are visible in TEM images. (C) TEM image of a typical complete gold shell deposited onto a decorated sphere.

Gold on Silica Core-Shells

The resulting decorated spheres are shown in the TEM images of Figure 9.2A,B. Unlike APTMS decoration, the FGNP gold attachment is stable under sonication. Successful decoration of slides was verified using X-ray photoelectron spectrometry (XPS) which confirmed both the presence of gold and Hf^{4+}.

In theory any metal may be deposited on a decorated sphere. The molecular tether presented here has been used to synthesize complete gold shell deposited on 260 nm spheres as is shown in Figure 9.2C. In practice the choice of metal shell is limited to those which can be accomplished at neutral pH and lower. Consequently this seeding method is not compatible with Tollen's type methods for the reduction of silver. The alkaline conditions required for the silver reduction interferes with the attachment of the phosphonate group to the adsorbed Hf^{4+}.

In the published method for the decoration of spheres with plain gold nanoparticles linked to the spheres by APTMS ligands,[40] heating was not required. The elevated temperature required for the gold reduction using the hafnium and phosphonate linkage suggests a difference in activation energies. This difference may be related to the degree of decoration on the sphere, or may be explained by the ligand coating on the FGNP. The ligand attached to the FGNP may limit the diffusion of Au^{2+} to the gold nanoparticle surface where it can be reduced as opposed to the uncoated gold nanoparticles used in previous decoration methods.[40]

A study of the electrical properties of gold core-shell structures was not undertaken, though the electrical properties of gold core-shell materials have not been previously investigated. Nonetheless, there are some reasonable expectations that can be discussed

based on our late understanding of chemically deposited silver. Gold is less prone to oxidation and corrosion than silver and the morphology of gold shells is not as rough or percolative as those we report on silver. Though smoother and more uniform than silver shells, it would not be reasonable to assume that these gold shells will exactly parallel their VD thin film counterparts. Though the smoother more uniform geometry of the gold shells are visibly similar to VD films, the microstructure of gold shells may be very different. The shells are anticipated to be polycrystalline with crystallite growth occurring through a chemical reduction processes similar to those which we report for the growth of silver. For silver, randomly oriented crystals with a large polydispersity of grain sizes and a high concentration of interfacial defects between the grains were produced. We have also reported on how the greater lattice strain due to random crystallite texture is reflected in the value of P for polycrystalline metals. An XRD study of the gold films produced by this and other methods is warranted to determine the microstructural contributions to the electrical properties of the gold shells and how they may differ from VD films. Investigations of the electrical transport in gold shells are highly relevant due to the potential for materials that may interrelate their optical and electrical properties. As a catalytically active metal, gold core-shells may also find applications in catalytic processes.

Silver on Gold Core-Shell Nanoparticles

One limitation of the phosphonate ligand system used to attach FGNP to silica spheres treated with Hf^{4+} was that basic solutions passivated the Hf^{4+} ions and caused detachment of the phosphonate groups along with the gold nanoparticles. While this condition prevents the use of the SC method for depositing silver on the the gold decorated spheres, it does not interfere with the silver reduction onto the gold nanoparticles themselves. It was observed that a nanoparticle core-shell material, that of silver on gold, can be synthesized in this way. A study of these nanoparticles is of interest primarily for their optical properties. In this section the method of synthesis and a basic characterization of these metal-metal core-shell nanoparticles is presented.

As noted above, when an FGNP decorated glass slide was soaked in the basic silver reduction solution, a sol of yellow colored nanoparticles resulted over the course of a few hours and no visible deposition on the slide occurred. XPS analysis confirmed the detachment of the entire FGNP by the detection of only hafnium ions on the slide

without any carbon or gold. The yellow color of the remaining sol was indicative of silver nanoparticles. However it was not immediately clear whether pure silver nanoparticles grew in solution with the gold, or whether silver reduced directly onto the gold. For comparison silver was reduced onto plain gold nanoparticles produced by a published method.[40] UV-vis studied revealed that silver reduced directly onto FGNP as well as onto plain gold nanoparticles. Rather than the addition of gold and silver nanoparticle spectra, the spectra for the two types of nanoparticles grown with various silver thicknesses showed peak shifts consistent with theoretical calculations for silver on gold nanoparticle materials.[44]

The samples were prepared as follows. A sample of the sol for silver on FGNP which had a large size distribution of nanoparticles visible in TEM images, was centrifuged four times. The top of the supernatant and the base of the pellet were collected as separate samples with the central portion being centrifuged again. The resulting size separated nanoparticle sols showed a color gradient from yellow-orange to orange-red, evidencing the larger to smaller particles respectively. UV-visible spectra of each of the solutions were compared to theoretical and experimental data for silver grown on gold nanoparticles. Typically as the size of pure gold nanoparticles increases, the SPR peak blue shifts to smaller wavelengths. The SPR for silver nanoparticles, however, shifts red as the radius increases. Theoretical models of silver shells ranging from 0.5-8 nm thick grown on gold nanoparticles of 8 nm diameter show that the gold sol peak starts near 500 nm. The combined silver on gold peak shifts blue, to higher energy, as silver thickness increases until a peak near 400 nm dominates. As shell thickness continues to increase, the resonance energy then reverses the shift to red. Simultaneously a dip begins to appear near 300 nm which is characteristic of silver. The resonance peak reaches 413 nm when the core diameter and shell thickness are both 8 nm. This theoretical trend has also been previously supported by an experiment using 12 nm gold cores and silver shell thicknesses from 0-6.5 nm.[44]

The UV-Vis data presented in Figure 9.3 for the size separated core-shell silver on FGNP exhibits the same trend. The sol with the largest nanoparticles is designated sol A, continuing through the smallest particles as sol E. The sizes of these nanoparticles have not been independently measured. The relative sizing is derived from the centrifugation times. The characteristic silver dip clearly grows in as particle size increases. Comparison of the sol E to sol C reveals a blue shift from 460 nm to 422 nm. The trend then reverses to a red shift as continued silver growth dominates the
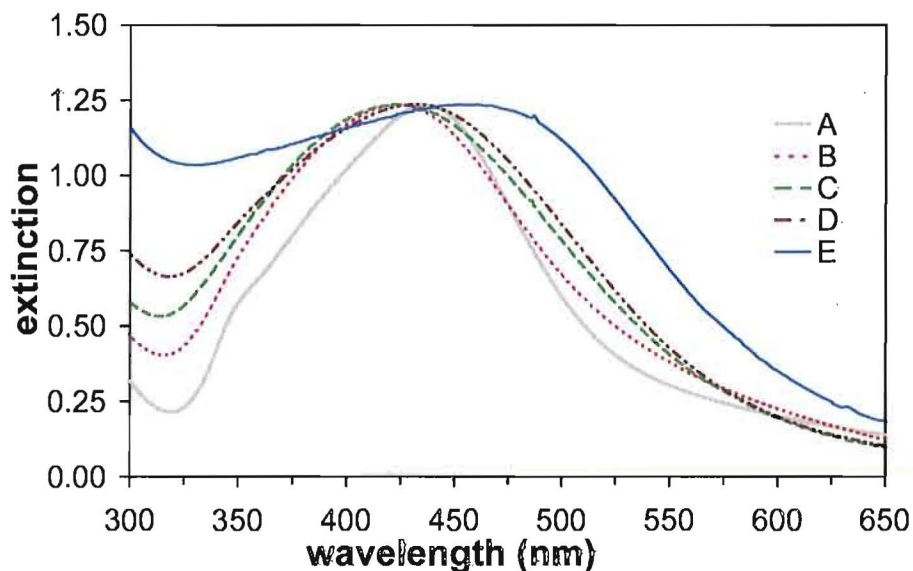
Figure A.3: UV-vis spectra showing the resonance peak for sols of silver coated on FGNP. The spectra A-E represent various nanoparticle sizes from largest to smallest respectively.

spectra of sols B and A. Spectra of four additional sols support these trends but have been omitted for clarity.

The silver on FGNP nanoparticles remained stable sols for months without further growth or aggregation as indicated by their constant color. By contrast, silver deposited onto plain gold nanoparticles aggregated and settled in less that 24 hours. The stability of the nanoparticles suggests that the functional ligand remains present, shifting to the silver surface as the deposition occurs, thus protecting the core-shell nanoparticles from aggregation.

Conclusion

In conclusion the FGNP material developed by the Jim Hutchison group has been applied for use both in the seeding of silica spheres for the production of gold shells and in the production of nanoparticle silver on gold core-shell materials. The nanoparticle structures have the valuable property of being stable in size and suspension for a significant length of time, presumably due the the attachment of the functional ligand to the outside of the silver shell. The silica spheres decorated with the FGNP differ from those previously developed in three ways: 1) they provide a secure linkage between gold and silica which is not prone to polymerization, 2) the exposed surface

of the functionalized gold has a phosphonate ligand shell, and 3) the linkage system provides a consistent high density of decoration allowing for smoother more uniform shell growth. Present results demonstrate that this is a reliable method of depositing complete gold shells.

APPENDIX B

ABBREVIATIONS AND SYMBOLS

α	temperature coefficient of resistance (or resistivity)
α_{ave}	temperature coefficient of resistance averaged for a collection of films with the same t_{eff}
α_{calc}	temperature coefficient of resistance calculated using the F-S model
φ	wavelength of radiation used for XRD method
λ	electron mean free path
λ_{Ag}	mean free path of silver (~55nm)
λ_{eff}	effective mean free path including multiple forms of scattering (uses Matthiessen Rule)
λ_g	electron mean free path due only to scattering at grain boundaries
λ_o	electron mean free path at temperature, T_o
λ_p	electron mean free path due only to phonon scattering
λ_s	electron mean free path due only to scattering at film surfaces
ν_f	fermi velocity of an electron
ρ	resistivity
ρ_i	resistivity due all factors excluding phonons
ρ_o	resistivity at temperature, T_o
ρ_p	resistivity due exclusively to phonons

τ	electron relaxation time
τ_b	electron relaxation time in the bulk
τ_{eff}	electron relaxation time due to all scattering sources (uses Matthiessen Rule)
τ_i	electron relaxation time determined only by scattering which is not due to phonons
τ_o	electron relaxation time at temperature, T_o
τ_{oeff}	electron relaxation time due to all scattering sources at temperature, T_o (uses Matthiessen Rule)
θ	angle of XRD spectrum, usually a peak location
A	Area of the coverslip substrate
A_e	exposed area fraction
A_f	metal filling fraction
AFM	atomic force microscopy
B	full width at half maximum (also FWHM)
CD	chemically deposited (silver)
CP	linear regression confidence parameter
D	average crystallite size
d	density (of silver $10.5g/cm^3$)
DMSO	dimethysulfoxide
e	charge of an electron
e	actual area of the slide not covered by silver (cm^2)
EDS	energy dispersive spectrometry
EPMA	electron probe microanalysis

f	actual area of the slide covered by silver (cm^2)
FGNP	(phosphonate ligand) functionalized gold nanoparticles
F-S	Fuchs-Sondheimer model for the influence of surface scattering on resistivity of thin metal films
FWHM	full width at half maximum (of an XRD peak)
g	geometric parameter
K	$P^{\frac{\lambda}{D}}$, the term in the V-H model that describes the influence of grain boundaries
m	mass of silver deposited on a single side of substrate
m_d	total mass deposited on all sides of a substrate
m_e	mass of an electron
n	electron density
n_{eff}	effective electron density based on V_H model
n-Ag	nanostructured silver, referring specifically to composites of silver nanoparticles
n-Au	nanostructured gold, referring specifically to composites of gold nanoparticles
n-metals	nanostructured metals, referring to composites of metal nanoparticles
p	specularity parameter as defined by the F-S model
P	transmission coefficient as defined by the V-H model
PVA	polyvinyl alcohol
PVP	polyvinyl pyrrolidone
R	resistance
SC	stoichiometrically controlled method for the deposition of silver onto silica spheres

SEM	scanning electron microscopy
SPR	surface plasmon resonance
t	thickness of a film
T	temperature variable
t_c	critical thickness during VD film growth at which a conduction pathway first exists
t_{eff}	film thickness calculated from the mass of silver deposited and limited by the A_f
t_{mass}	film thickness calculated from the mass of silver deposited
T_o	constant temperature against which relative temperatures are measured
TC	temperature controlled method for the deposition of silver onto silica spheres
TEM	transmission electron microscope
UV-vis	ultraviolet-visible spectrometry
VD	vacuum deposited (metal)
V-H	Vancea-Hoffmann model for the influence of grain boundaries in polycrystalline metals
VPP	voltametric pellet press
XRD	X-ray diffraction or diffractometry

REFERENCES

1. Duan, X. *MRS Bulliten* **2007**, *32*, 134–141.

2. Lagally, M. G. *J. Phys.: Conf. Ser.* **2007**, *61*, 652–657.

3. Pushparaj, V. L.; Shaijumon, M. M.; Kumar, A.; Murugesan, S.; Ci, L.; Vajtai, R.; Linhardt, R. J.; Nalamasu, O.; Ajayan, P. M. *Proc. Nat. Acad. Sci. U.S.A.* **2007**, *104*, 13574–13577.

4. Patolsky, F.; Timko, B. P.; Yu, G.; Fang, Y.; Greytak, A. B.; Zheng, G.; Lieber, C. M. *Science* **2006**, *313*, 1100–1104.

5. Fuchs, K. *Proc. Cambridge Phil. Soc.* **1938**, *34*, 100–108.

6. Aizpurua, J.; Hanarp, P.; Sutherland, D. S.; Kall, M.; Bryant Garnett, W.; Garcia de Abajo, F. J. *Phys. Rev. Lett.* **2003**, *90*, year.

7. Andersen, P. C.; Rowlen, K. L. *Appl. Spectrosc.* **2002**, *56*, 124A–135A.

8. Zhang, X. G.; Butler, W. H. *Phys. Rev. B: Condens. Matter Mat. Phys.* **1995**, *51*, 10085–10103.

9. Zhigal'skii, G.; Jones, B. *The Physical Properties of Thin Metal Films*; Taylor and Francis: London, 2003.

10. Sondheimer, E. *Adv. Phys.* **1952**, *1*, 1–42.

11. Sambles, J. R.; Elsom, K. C. *J. Phys. D: Appl. Phys.* **1982**, *15*, 1459–1467.

12. Reiss, G.; Hastreiter, E.; Bruckl, H.; Vancea, J. *Phys. Rev. B: Condens. Matter Mat. Phys.* **1991**, *43*, 5176–5179.

13. Rao, V. V. R. N.; Mohan, S.; Reddy, P. J. *Thin Solid Films* **1977**, *42*, 283–289.

14. D. Dayal, P. R.; Wissmann, P. *Thin Solid Films* **1981**, *79*, 193–199.

15. Pichard, C.; Drexler, J.; Tosser, A.; Flechon, J. *J. Mater. Sci.* **1983**, *18*, 2414–2418.

16. Schroder, D. K. *Semiconductor Materials and Device Characterization, 2nd Edition*; Wiley.

17. Haruta, A. *Chem. Rec.* **2003**, *3*, 75–87.

18. Pal, B. N.; Kundu, T. K.; Banerjee, S.; Chakravorty, D. *J. Appl. Phys.* **2003**, *93*, 4201–4206.

19. Gur, I.; Fromer, N. A.; Chen, C.-P.; Kanaras, A. G.; Alivisatos, A. P. *Nano Lett.* **2007**, *7*, 409–414.

20. O'Neal, D.; Hirsch, L.; Halas, N.; Payne, J.; West, J. *Cancer Lett.* **2004**, *209*, 171–176.

21. Wang, Y.; Ibisate, M.; Li, Z.-Y.; Xia, Y. *Adv. Mater.* **2006**, *18*, 471–476.

22. Zhang, W.; Wang, Z.; Hu, A.; Ming, N. *J. Phys.: Condens. Matter* **2000**, *12*, 9361–9370.

23. Chen, C.-W.; Serizawa, T.; Akashi, M. *Chem. Mater.* **1999**, *11*, 1381–1389.

24. Jackson, J. B.; Halas, N. J. *J. Phys. Chem. B* **2001**, *105*, 2743–2746.

25. Aden, A.; Kerker, M. *J. Appl. Phys.* **1951**, *22*, 1242–1246.

26. Masten, A.; Bruggemann, M.; Wissmann, P. *Fresenius J. Anal. Chem.* **1999**, *365*, 227–230.

27. Chen, A.; Hasegawa, K.; Deutsch, M. *Opt. Lett.* **2007**, *32*, 1770–1772.

28. Sotelo, J.; Ederth, J.; Niklasson, G. *Phys. Rev. B* **2003**, *67*, 1951061–1951068.

29. Barnickel, P.; Wokaun, A. *Mol. Phys.* **1989**, *67*, 1355–1372.

30. Mayer, A. B. R.; Grebner, W.; Wannemacher, R. *J. Phys. Chem. B* **2000**, *104*, 7278–7285.

31. Schierhorn, M.; Liz-Marzan, L. M. *Nano Lett.* **2002**, *2*, 13–16.

32. Jiang, Z.-J.; Liu, C.-Y. *J. Phys. Chem. B* **2003**, *107*, 12411–12415.

33. Pol, V. G.; Grisaru, H.; Gedanken, A. *Langmuir* **2005**, *21*, 3635–3640.

34. Graf, C.; van Blaaderen, A. *Langmuir* **2002**, *18*, 524–534.

35. Kobayashi, Y.; Salgueirino-Maceira, V.; Liz-Marzan, L. M. *Chem. Mater.* **2001**, *13*, 1630–1633.

36. Yin, Y.; Li, Z.-Y.; Zhong, Z.; Gates, B.; Xia, Y.; Venkateswaran, S. *J. Mater. Chem.* **2002**, *12*, 522–527.

37. Lu, L.; Zhang, H.; Sun, G.; Xi, S.; Wang, H.; Li, X.; Wang, X.; Zhao, B. *Langmuir* **2003**, *19*, 9490–9493.

38. Westcott, S.; Oldenburg, S. J.; Lee, R. T.; Halas, N. J. *Langmuir* **1998**, *14*, 5396–5401.

39. Cassagneau, T.; Caruso, F. *Adv. Mater.* **2002**, *14*, 732–736.

40. Pham, T.; Jackson, J. B.; Halas, N. J.; Lee, T. R. *Langmuir* **2002**, *18*, 4915–4920.

41. Pavia, D. L.; Lampman, G. M.; Kriz, G. S. *Introduction to Organic Laboratory Techniques. A Contemporary Approach. 3rd Ed*; Saunders College Publishing.

42. Mock, J. J.; Barbic, M.; Smith, D. R.; Schultz, D. A.; Schultz, S. *J. Chem. Phys.* **2002**, *116*, 6755–6759.

43. El-Sayed, M. A. *Acc. Chem. Res.* **2001**, *34*, 257–264.

44. Kreibig, U.; Vollmer, M. *Optical Properties of Metal Clusters*; Springer-Verlag.

45. Jensen, T. R.; Malinsky, M. D.; Haynes, C. L.; van Duyne, R. P. *J. Phys. Chem. B* **2000**, *104*, 10549–10556.

46. Sun, Y.; Xia, Y. *Anal. Chem.* **2002**, *74*, 5297–5305.

47. Schultz, S.; Smith, D. R.; Mock, J. J.; Schultz, D. A. *Proc. Nat. Acad. Sci. U.S.A.* **2000**, *97*, 996–1001.

48. McFarland, A. D.; Van Duyne, R. P. *Nano Lett.* **2003**, *3*, 1057–1062.

49. Suryanarayana, C. *Adv. Eng. Mater.* **2005**, *7*, 983–992.

50. Ederth, J.; Kish, L.; Olsson, E.; Granqvist, C. *J. Appl. Phys.* **2000**, *88*, 6578–6582.

51. Qin, X.; Zhang, L.; Cheng, G.; Liu, X.; Jin, D. *J. Phys. D: Appl. Phys.* **1998**, *31*, 24–31.

52. Walter, E. C.; Penner, R. M.; Liu, H.; Ng, K. H.; Zach, M. P.; Favier, F. *Surf. Interface Anal.* **2002**, *34*, 409–412.

53. Durkan, C.; Welland, M. E. *Phys. Rev. B* **2000**, *61*, 14215–14219.

54. Dorbolo, S.; Ausloos, M.; Vandewalle, N.; Houssa, M. *J. Appl. Phys.* **2003**, *94*, 7835–7838.

55. Halliday, D.; Resnick, R.; Walker, J. *Fundamentals of Physics, 4th Edition*; John Wiley and Sons, Inc.: New York, 1993.

56. Kastle, G.; Boyen, H. G.; Schroeder, A.; Plettl, A.; Ziemann, P. *Phys. Rev. B: Condens. Matter Mat. Phys.* **2004**, *70*, 165414–165416.

57. Vancea, J.; Hoffmann, H.; Kastner, K. *Thin Solid Films* **1984**, *121*, 201–216.

58. Rao, M.; Mathur, B.; Chopra, K. *J. Mat. Sci.* **1995**, *30*, 2682–2685.

59. Doron-Mor, I.; Zahava, B.; Filip-Granit, N.; Vaskevich, A.; Rubinstein, I. *Chem. Mater.* **2004**, *16*, 3476–3483.

60. Venables, J. A. *Introduction to Surface and Thin Film Processes*; Cambridge University Press: New York, 2000.

61. Arnason, S.; Herschfield, S.; Hebard, A. *Phys. Rev. Lett.* **1998**, *81*, 3936–3939.

62. Namba, Y. *Jpn. J. Appl. Phys.* **1970**, *9*, 1326.

63. Jacob, U.; Vancea, J.; Hoffmann, H. *Phys. Rev. B: Condens. Matter Mat. Phys.* **1990**, *41*, 11852–11857.

64. Elsom, K. C.; Sambles, J. R. *J. Phys. F: Met. Phys.* **1981**, *11*, 647–656.

65. Brueckl, H.; Reiss, G. *Surf. Sci.* **1992**, *267/270*, 772–776.

66. Luo, E. Z.; Heun, S.; Kennedy, M.; Wollschlaeger, J.; Henzler, M. *Phys. Rev. B: Condens. Matter Mat. Phys.* **1994**, *49*, 4858–4865.

67. Mayadas, A. F.; Shatzkes, M. *Phys. Rev. B: Solid State* **1970**, *[3] 1*, 1382–1389.

68. Fan, P.; Yi, K.; Shao, J.-D.; Fan, Z.-X. *J. Appl. Phys.* **2004**, *95*, 2527–2531.

69. Zhang, Q.; Cao, B.; Zhang, X. *Phys. Rev. B 74*, 134109/1–134109/5.

70. Sambles, J. R.; Elsom, K. C.; Jarvis, D. J. *Solid State Commun.* **1979**, *32*, 997–1000.

71. Vancea, J.; Reiss, G.; Hoffmann, H. *Phys. Rev. B: Condens. Matter Mat. Phys.* **1987**, *35*, 6435–6437.

72. Reiss, G.; Vancea, J.; Hoffmann, H. *Phys. Rev. Lett.* **1986**, *56*, 2100–2103.

73. Tyan, J.-W.; Lueb, J. T. *J. Appl. Phys.* **1994**, *75*, 325–331.

74. Leung, K. M. *Phys. Rev. B: Condens. Matter Mat. Phys.* **1984**, *30*, 647–658.

75. Alford, T. L.; Chen, L.; Gadre, K. S. *Thin Solid Films* **2003**, *429*, 248–254.

76. Wedler, G.; Wiebauer, W. *Thin Solid Films* **1975**, *28*, 65–81.

77. Sambles, J. R.; Elsom, K. C. *Solid State Commun.* **1984**, *52*, 367–370.

78. Smilauer, P. *Contemp. Phys.* **1991**, *32*, 89–102.

79. Liu, Y. C.; Yu, C. C.; Yang, K. H. *Electrochem. Commun.* **2006**, *8*, 1163–1167.

80. Lafouresse, M. M.; Heard, P. J.; Schwarzacher, W. *Phys. Rev. Lett.* **2007**, *98*, 236101/1–236101/4.

81. Zevin, L. S.; Kimmel, G. *Quantitative X-Ray Diffractometry*; Springer-Verlag: New York, 1995.

82. Peterson, S.; Deutsch, M.; Bouwman, J.; Chen, A. *J. Colloid Interface Sci.* **2007**, *306*, 41–49.

83. van der Pauw, L. *Philips Research Reports* **1958**, *13*, 1–9.

84. S. Mohan, P. J. R. *Proceedings of the Nuclear Physics and Solid State Physics Symposium* **1974**, *17C*, 128–130.

85. Schumacher, D. *Surface Scattering Experiments with Conduction Electrons*, 1st ed.; Springer-Velag: Berlin, 1993; Vol. 128.

86. Antonets, I. V.; Kotov, L. N.; Nekipelov, S. V.; Golubev, Y. A. *Tech. Phys.* **2004**, *49*, 306–309.

87. Rohde, C. A.; Hasegawa, K.; Deutsch, M. *Phys. Rev. Lett.* **2006**, *96*, 045503/1–045503/4.

88. Sieradzki, K.; Bailey, K.; Alford, T. L. *Appl. Phys. Lett.* **2001**, *79*, 3401–3403.

89. Verma, B. *Phys. Rev. B: Condens. Matter Mat. Phys.* **1972**, *10*, 117–118.

90. Swanson, H. E.; Tatge, E. *N. B. S. (U.S.) Monograph* **1953**, *1*, 23.

91. Swanson, H. E.; Morris, M. C.; Stinchfield, R. P.; Evans, E. H. *N. B. S. (U.S.) Monograph* **1962**, *25*, 45.

92. Chung, D.; Haven, P. D.; Arnold, H.; Ghosh, D. *X-Ray Diffraction at Elevated Temperatures*; VCH Publishers: New York, 1993.

93. Humphreys, F. *Recrystallization and Related Annealing Phenomenon*; Elsevier: Boston, 2004.

94. Wissmann, P.; Finzel, H.-U. *The Effect of Annealing on the Electrical Resistivity of Thin Metal Films*; Springer-Verlag: New York, 2007.

95. Zhao, S.; Wang, S.; Cheng, D.; Ye, H. *J. Phys. Chem. B* **2002**, *105*, 12857–12860.

96. Mohan, S.; Reddy, P. J. *Phys Stat Sol.* **1973**, *15*, K1–K3.

97. Kim, H. C.; Alford, T. L.; Allee, D. R. *Appl. Phys. Lett.* **2002**, *81*, 4287–4289.

98. Liang, Z.; Susha, A. S.; Caruso, F. *Adv. Mater.* **2002**, *14*, 1160–1164.

99. Stoeber, W.; Fink, A.; Bohn, E. *J. Colloid Interface Sci.* **1968**, *26*, 62–69.

100. Vehkamaki, H. *Classical Nucleation Theory in Multicomponent Systems*; Springer-Verlag: Berlin, 2006.

101. Oldenburg, S. J.; Jackson, J. B.; Westcott, S. L.; Halas, N. J. *Appl. Phys. Lett.* **1999**, *75*, 2897–2899.

102. Prodan, E.; Nordlander, P. *Nano Lett.* **2003**, *3*, 543–547.

103. Prodan, E.; Radloff, C.; Halas, N. J.; Nordlander, P. *Science* **2003**, *302*, 419–422.

104. Gressilon, S.; Aigouy, L.; Boccara, A.; Rivoal, J. C.; Quelin, X.; Desmarest, C.; Gadenne, P.; Shubin, V. A.; Shalaev, V. M. *Phys. Rev. Lett.* **1999**, *82*, 4520–4523.

105. Klimov, V. I. *Semiconductor and Metal Nanocrystals*; Marcel Dekker, Inc.: New York, 2004.

106. Chou, K.-S.; Ren, C.-Y. *Mat. Chem. and Phys.* **2002**, *64*, 241–246.

107. Brus, L. *Nano Lett.* **2002**, *3*, 1611–1615.

108. Foster, E.; Kearns, G.; Goto, S.; Hutchison, J. *Adv. Mater.* **2005**, *17*, 1542–1545.

109. Woehrle, G. H.; Warner, M. G.; Hutchison, J. E. *J. Phys. Chem. B* **2002**, *106*, 9979–9981.

110. Semin, D. J.; Lo, A.; Roark, S. E.; Skodje, R. T.; Rowlen, K. L. *J. Chem. Phys.* **1996**, *105*, 5542–5551.

111. Hurt, H. H.; Bennett, J. M. *Appl. Opt.* **1985**, *24*, 2712–2120.

112. Sharma, S. K.; Spitz, J. *Thin Solid Films* **1980**, *67*, 109–116.

113. Murray, B. J.; Newberg, J. T.; Walter, E. C.; Li, Q.; Hemminger, J. C.; Penner, R. M. *Anal. Chem.* **2005**, *77*, 5205–5214.

114. Murray, B. J.; Walter, E. C.; Penner, R. M. *Nano Lett.* **2004**, *4*, 665–670.

115. Wissmann, P.; Editor, *Studies in Surface Science and Catalysis, Vol. 32: Thin Metal Films and Gas Chemisorption*; Springer-Verlag: New York, 1987.

116. Waterhouse, G.; Bowmaker, G.; Metson, J. *Phys. Chem. Chem. Phys.* **2001**, *3*, 3838–3845.

117. Garner, W.; Reeves, L. *Trans. Faraday Soc.* **1954**, *50*, 254–260.

118. M.I. Talukdar, E. B. *Solid State Commun.* **1969**, *7*, 309–310.

119. Sathaye, S.; Patil, K.; Paranjape, D.; Padalkar, S. *Mat. Res. Bulletin* **2001**, *36*, 1149–1155.

120. Xia, Y.; Gates, B.; Yin, Y. *Aust. J. Chem.* **2001**, *54*, 287–290.

121. Endo, T.; Kerman, K.; Nagatani, N.; Hiepa, H. M.; Kim, D. K.; Yonezawa, Y.; Nakano, K.; Tamiya, E. *Anal. Chem.* **2006**, *78*, 6465–6475.

122. Ung, T.; Liz-Marzan, L. M.; Mulvaney, P. *Langmuir* **1958**, *14*, 3740–3748.

123. Hu, M.; Noda, S.; Okubo, T.; Yamaguchi, Y. *Appl. Surf. Sci.* **2001**, *181*, 307–316.

124. Le Grange, J.; Markham, J. *Langmuir* *9*, 1749–1753.